Dissertation

submitted to the
Combined Faculty of Natural Sciences and Mathematics
of the Ruperto Carola University Heidelberg, Germany
for the degree of
Doctor of Natural Sciences

Presented by
M.Sc. Ka-Hou Man
Born in Macau S.A.R., China
Oral Examination: March 20th, 2023

ROLES OF *SOX10* IN GLIOBLASTOMA STEM CELL PLASTICITY

Referees:

Prof. Dr. Benedikt Brors

Prof. Dr. Peter Lichter

The work and results of the following dissertation were performed and obtained from October 2018 until October 2022 under the supervision of Dr. Bernhard Radlwimmer and Prof. Dr. Peter Lichter in the Division of Molecular Genetics at the German Cancer Research Center (DKFZ), Heidelberg, Germany.

Declaration

I hereby declare that I have written the submitted dissertation “Roles of SOX10 in Glioblastoma Stem Cell Plasticity” myself and in this process have not used any other sources than those indicated.

I hereby declare that I have not applied to be examined at any other institution, nor have I used the dissertation in this or any other form at any other institution as an examination paper, nor submitted it to any other faculty as a dissertation.

Ka-Hou Man

Summary

Glioblastoma (GB), the most common brain malignancy in adults, remains incurable despite being extensively characterized genetically and epigenetically. Current multimodal treatment regimens only marginally extend patients' survival, and patients almost invariably succumb to the disease rapidly due to tumor recurrence, underscoring the unmet clinical needs in GB treatment. Central to our understanding of GB biology is the brain tumor stem cell hypothesis, which postulates the existence of a population of self-renewing tumor cells. These cells co-opt transcriptional circuitry critical for maintaining the neural stem cell (NSC) state, thereby maintaining plasticity, tumor heterogeneity and potentiating aggressive phenotypes.

Our previous work identified the oligodendroglial transcription factor *SOX10* as a master regulator of a subtype of GB. In this thesis, I strive to understand the role of *SOX10* in mediating tumor cell phenotypic plasticity and its potential clinical implications in GB. The analysis of public datasets suggested that *SOX10*-high and *SOX10*-low human samples occupy different cellular states on the developmental spectrum, indicating an inverse correlation between *SOX10* expression and NSC-related cell states in GB. Using a mouse syngraft model, I demonstrated that the knockdown (KD) of Sox10 in tumor cells leads to increased tumorigenicity and aggressiveness, corresponding to the phenotypic transitions recently published in mouse GB models derived from different neural progenitor cells. Single-cell transcriptomic profiling uncovered the cell state plasticity of Sox10-KD tumors, wherein a population of quiescent founder cells appears to drive the developmental-like phenotype of KD tumor cells, mirroring the spectrum of normal NSC development. Further *in vitro* investigations showed that the downregulation of Sox10 leads to the emergence of slow-cycling stem-like cells within both mouse and human glioma stem-like cells, exemplified by an increase in Notch pathway activity, limited proliferative capacity upon low growth factor culture conditions, and increased resilience to differentiation cues. Furthermore, I showed that temozolomide, the chemotherapeutic agent used in first-line clinical therapy, downregulated *SOX10* expression in human brain tumor stem cells. Upon release from therapeutic pressure, recovered cells retained lower expression of *SOX10* and maintained a pool of quiescent stem-like tumor cells, suggesting that treatment pressure might similarly induce a latent pool of quiescent founder tumor cells, which potentially fuel tumor regrowth. Finally, I showed that the quiescent state observed in the Sox10-KD model depends on the activity of the Notch pathway. Its pharmacological inhibition drives KD cell transition to a less quiescent, activated state, increasing their vulnerability to anti-proliferative treatment induced by Fimepinostat, a dual inhibitor of the PI3K and HDAC pathways.

In summary, my doctoral study unraveled a transition to quiescent cell states mediated by the reduction of *SOX10* expression in brain tumor stem cells. Using *SOX10*-KD cells as a model, I provided data indicating the feasibility of combination therapies depleting the quiescence founder state and simultaneously targeting resulting more proliferative cell states. My study adds to a growing body of evidence on the plastic differentiation hierarchy of brain tumor stem cells, the importance of quiescent stem cells in mediating phenotypic disparity, and the feasibility of a "state-inducing" therapeutic approach in glioblastoma.

Zusammenfassung

Das Glioblastom (GB), die häufigste bösartige Erkrankung des Gehirns bei Erwachsenen und ist nach wie vor unheilbar, obwohl es genetisch und epigenetisch umfassend charakterisiert ist. Die derzeitigen multimodalen Behandlungsmethoden verlängern die Überlebenszeit der Patienten nur geringfügig, und die Patienten erliegen der Krankheit fast ausnahmslos rasch aufgrund eines Tumorrezidivs, was den ungedeckten klinischen Bedarf an GB-Behandlung unterstreicht. Von zentraler Bedeutung für unser Verständnis der GB-Biologie ist die Hirntumor-Stammzellenhypothese, die die Existenz einer Population von sich selbst erneuernden Tumorzellen postuliert. Diese Zellen kooptieren Transkriptionsschaltkreise, die für die Aufrechterhaltung des Zustands neuraler Stammzellen (NSC) entscheidend sind, und erhalten dadurch Plastizität und Tumorheterogenität aufrecht und verstärken aggressive Phänotypen.

In früheren Arbeiten unserer Gruppe wurde der oligodendrogliale Transkriptionsfaktor *SOX10* als Hauptregulator des GB-Subtyps identifiziert. In dieser Arbeit versuchte ich, die Rolle von *SOX10* bei der Vermittlung phänotypischer Tumorzellplastizität und ihre möglichen klinischen Auswirkungen bei GB zu verstehen. Die Analyse öffentlicher Datensätze ergab, dass menschliche Proben mit hohem und niedrigem *SOX10*-Gehalt unterschiedliche zelluläre Zustände im Entwicklungsspektrum einnehmen, was auf eine umgekehrte Korrelation zwischen *SOX10*-Expression und NSC-verwandten Zellstadion in GB hinweist. Anhand eines Maus Syntransplantationsmodells konnte ich zeigen, dass der Knockdown (KD) von Sox10 in Tumorzellen zu einer erhöhten Tumorigenität und Aggressivität führt. Entsprechende phänotypische Übergänge wurden in Daten von Patiententumoren und kürzlich veröffentlichten Mausmodellen von GB beobachtet, die aus verschiedenen neuralen Vorläuferzellen stammen. Einzelzell-Transkriptom-Profiling deckte die Zellstatus-Plastizität von Sox10-KD-Tumoren auf, wobei eine Population von ruhenden Gründerzellen den entwicklungsähnlichen Phänotyp von KD-Tumorzellen zu steuern scheint, der das Spektrum der normalen NSC-Entwicklung widerspiegelt. Weitere In-vitro-Untersuchungen zeigten, dass die Herunterregulierung von Sox10 zur Entstehung von langsam zyklierenden stammähnlichen Zellen sowohl in Maus- als auch in menschlichen Gliomstammzellen führt, die sich durch eine erhöhte Aktivität des Notch-Signalwegs, eine begrenzte Proliferationsfähigkeit unter Kulturbedingungen mit niedrigem Wachstumsfaktor und eine erhöhte Widerstandsfähigkeit gegenüber Differenzierungsreizen auszeichnen. Darüber hinaus konnte ich zeigen, dass Temozolomid, das Chemotherapeutikum, das in der klinischen Erstlinientherapie eingesetzt wird, die *SOX10*-Expression herunterreguliert und die Marker für ruhende Stammzellen in verschiedenen in-vitro Modellen hochreguliert. Nach Aufhebung des therapeutischen Drucks behielten die Zellen eine geringere Expression von *SOX10* bei. Außerdem behielten sie einen Pool ruhender stammähnlicher Tumorzellen bei, was darauf hindeutet, dass der Behandlungsdruck in ähnlicher Weise ein latentes Reservoir ruhender Gründertumorzellen induzieren könnte, die das Tumorwachstum über die Herunterregulierung von *SOX10* fördern. Schließlich habe ich gezeigt, dass der im Sox10-KD-Modell beobachtete Ruhezustand von der Aktivität des Notch-Signalwegs abhängt. Dessen pharmakologische Hemmung führte dazu, dass KD-Zellen in einen weniger ruhigen, aktivierten Zustand übergehen, was ihre Anfälligkeit für eine antiproliferative Behandlung durch Fimepinostat, einen dualen Inhibitor des PI3K- und HDAC-Signalwegs, erhöht.

Zusammenfassend lässt sich sagen, dass meine Doktorarbeit einen Übergang zu einem ruhenden Zellzustand aufgedeckt hat, der durch die Verringerung der *SOX10*-Expression in Hirntumor-Stammzellen vermittelt wird. Unter Verwendung von *SOX10*-KD-Zellen als Modell habe ich Daten geliefert, die auf die Durchführbarkeit von Kombinationstherapien hinweisen, die den Quieszenz-Ausgangszustand beseitigen und gleichzeitig auf die daraus resultierenden proliferativen Zellzustände abzielen. Meine Studie trägt zu einer wachsenden Zahl von Belegen für die plastische Differenzierungshierarchie von Hirntumor-Stammzellen, die Bedeutung der ruhenden Stammzellen bei der Vermittlung phänotypischer Unterschiede und die Durchführbarkeit eines "zellstadium-induzierenden" therapeutischen Ansatzes beim Glioblastom bei.

Contents

List of Figures

List of supplementary figures

List of tables

Abbreviations

7-AAD	7-Aminoactinomycin D
AC	Astrocyte
ADAM	A disintegrin and metalloproteinase
ANOVA	Analysis of Variance
ask	Activated neural stem cells
APC	Antigen-presenting cell
ASCL1	Achaete-scute homolog 1
AU	Arbitrary unit
AUC	Area under the ROC curve
BCA	Bicinchoninic acid
BDNF	Brain-derived neurotrophic factor
BFP	Blue fluorescent protein
BLBP	Brain lipid-binding protein
BLI	Bioluminescent Imaging
BMP	Bone morphogenetic protein
bp	base pair
BRD4	Bromodomain-containing protein 4
BSA	Bovine serum albumin
BTSC	Brain tumor stem cell
CAR	Chimeric antigen receptor
CCL2	Chemokine ligand 2
CD	Cluster of differentiation
CDK	Cyclin-dependent kinase
CDKN	Cyclin-dependent kinase inhibitor
CIMP	CpG island methylator phenotype
CL	Classical (subtype of GB)
CNS	Central nervous system
CNV	Copy number variation
COR	Cerebral organoid
CRISPRi	Clustered Regularly Interspaced Short Palindromic Repeats Interference
CSC	Cancer stem cell
CSPG4	Chondroitin sulfate proteoglycan 4
Ct value	Cycle threshold value
Ctrl	Control
DAPI	4'6-diamidino-2-phenylindole
dCas9	dead CRISPR-associated protein 9
DCTN2	Dynactin subunit 2
DEG	Differentially expressed genes
DIPG	diffuse intrinsic pontine glioma
DMSO	Dimethyl sulfoxide
DNA	Deoxyribonucleic acid
EGFR	Epidermal growth factor receptor
FACS	Fluorescence-activated Cell Sorting
FBS	Fetal bovine serum

FC	Fold change
GAPDH	Glyceraldehyde-3-phosphate dehydrogenase
GB	Glioblastoma
GF	Growth factor
GFAP	Glial fibrillary acidic protein
GFP	Green fluorescence protein
GLASS	The Glioma Longitudinal Analysis
GLICO	Glioma cerebral organoid
GO	Gene ontology
GRN	Gene regulatory network
GSC	Glioblastoma stem cell
GSEA	Geneset enrichment analysis
GSI	Gamma-secretase inhibitor
HDAC	Histone deacetylase
HES	Hairy and enhancer of split-5
HEY	Hairy/enhancer-of-split related with YRPW motif protein 1
HGG	High-grade glioma
HMG	High-Mobility Group
IC50	Half-maximal inhibitory concentration
IDH	Isocitrate dehydrogenase
IF	Immunofluorescence
IHC	Immunohistochemistry
IPC	Intermediate progenitor cell
IQR	Interquartile range
KD	Knockdown
KEGG	Kyoto Encyclopedia of Genes and Genomes
KRAB	Krüppel associated box
LDS	Lithium dodecyl sulfate
LGG	Lower-grade glioma
MACS	Magnetic-activated cell sorting
MAML	Mastermind-like protein 1
MAP2	Microtubule-associated protein 2
MAPK	Mitogen-activated protein kinase
MES	Mesenchymal (subtype of GB)
MGMT	O-6-methylguanine-DNA methyltransferase
MHC	Major histocompatibility complex
MITF	Microphthalmia-associated transcription factor
MRI	Magnetic resonance imaging
MSigDB	Molecular Signatures Database
NCC	Neural crest cell
NES	Normalized enrichment score
NF1	Neurofibromin 1
NICD	Notch intracellular domain
NPC	Neural progenitor cell
NRARP	NOTCH Regulated Ankyrin Repeat Protein

NSC	Neural stem cell
NT	Non-targeting control
OL	Oligodendrocytes
OLIG2	Oligodendrocyte transcription factor 2
OPC	Oligodendrocyte progenitor cell
OR	Odd ratio
PBS	Phosphate-buffered saline
PC	Principal component
PCA	Principal component analysis
PCR	Polymerase chain reaction
PEI	Polyethylenimine
PFA	Paraformaldehyde
PGK	Phosphoglycerate kinase 1
PI3K	Phosphoinositide 3-kinase
PN	Proneural (subtype of GB)
PRC	Polycomb repressor complex
PTEN	Phosphatase and tensin homolog
qNSC	Quiescent neural stem cell
qPCR	Quantitative polymerase chain reaction
RCAS/tv-a	Replication-competent avian sarcoma-leukosis virus (ASLV) long-terminal repeat (LTR) with splice acceptor
RGC	Radial glial cell
RNA	Ribonucleic acid
RT	Room temperature
RTK	Receptor tyrosine kinase
SEM	Standard error of the mean
SGZ	Subgranular zone
shRNA	Shor hairpin RNA
SOX	SRY-related HMG-box
ssGSEA	Single sample GSEA
SVZ	Subventricular zone
TAM	Tumor-associated macrophage
TBP	TATA-binding protein
TCGA	The Cancer Genome Atlas
TF	Transcription factor
TGF	Transforming growth factor
TME	Tumor microenvironment
TMZ	Temozolomide
TP53/Trp53	Tumor protein p53
TPM	Transcript per million
UMAP	Uniform Manifold Approximation and Projection
UMI	Unique molecular identifier
UTR	Untranslated region
WHO	World Health Organization
WB	Western blot
WT	Wildtype

1 Introduction

1.1 Glioblastoma

1.1.1 Epidemiological features

Gliomas are a heterogeneous group of brain malignancies, which refer to tumors with glial cell origins. Among different entities of gliomas, glioblastoma (GB) is the most common and aggressive form. Advances in molecular profiling revealed that various glioma entities represent distinct diseases with different prognostic and genetic features [1]. Based on the most recent edition of the World Health Organization (WHO) classifications (WHO CNS5) of tumors of the Central Nervous System (CNS), GB is defined as adult-type diffuse gliomas with wild-type isocitrate dehydrogenase (IDH-WT) [2]. This thesis mainly addresses GB and its biology, unless otherwise specified.

According to the statistical report from the Central Brain Tumor Registry of the United States (CBTRUS) published in 2021, GB accounts for 49.1% of all cases of primary malignant CNS tumors and 58.4% of all glioma cases in the US, rendering it one of the most prominent brain malignancies. The age-standardized incidence rate of GB currently stands at 3.23 per 100,000 and has been stable for the past decades. GB shows a late onset in life, with the median age of diagnosis at 65. This age group was also 3.41 times more likely to develop GB. Sex and ethincity seem to play a role in the incidence of GB - males are 1.65 times more likely to develop GB compared to females, while white Americans are around 2 times more likely to develop GB compared to African or Asian Americans [3]. The risk factors for GB remain largely unknown, although a very rare proportion of the patients have underlying genetic predispositions, including Li Fraumeni syndromes [4, 5].

1.1.2 Treatment of Glioblastoma

Figure 1 outlines the standard treatment of newly diagnosed GBs (known as the Stupp's regimen) [6]. The first step is maximal safe surgical resection aiming at removing as much of the tumor area as possible without severely impairing patients' neurological functions. However, given the infiltrative nature of GB, surgical resection is typically neither complete nor curative [7]. After 3-5 weeks of the post-operation recovery period, patients are treated with radiotherapy for 6 weeks (2 Gy daily, a total of 60 Gy). Temozolomide (TMZ) is administered at the same time (75 mg/m^2 daily during radiotherapy) to patients with methylated *MGMT* promoter (encoding O-6-methylguanine-DNA methyltransferase), a predictive biomarker for TMZ response [8]. Afterward, patients receive maintenance TMZ treatment for at least 12 months (120 mg/m^2 daily for 5 days as one cycle, one cycle every 4 weeks). In patients with non-methylated *MGMT* promoter, TMZ is usually not given. However, this view has been challenged since recent clinical trials showed that TMZ treatment to *MGMT* promoter non-methylated patients did not reduce [9], if not slightly improve [10], their survival when used in conjunction with radiotherapy, hence calling for the use of TMZ in GB patients regardless of their *MGMT* promoter methylation status.

Unfortunately, despite this aggressive multimodal treatment strategy, GB remains a largely fatal tumor. Compared with other glioma entities, GB has abysmal 5-year survival rate of 6.8% [2]. This dismal 5-year survival rate is on par with some of the deadliest cancer types known to humanity. Treatment with Stupp's regimen extends the median survival of primary GB to 12.1 months with radiotherapy alone and 14.6 months with concomitant radio-chemotherapy [6]. The primary cause of poor survival for GB patients is tumor recurrence. In clinical trials by Stupp and colleagues, 85% of the patients who underwent standard GB therapy had tumor progression [6]. There is no consensus on the standard-of-care for patients with recurrent tumors [7, 11]. Surgeries and radio/chemotherapy remained the mainstream options. However, the success of these approaches is limited by the extensive infiltration of the recurrent tumors. Alternatively, systemic salvage therapy may be administered to patients, including the anti-angiogenic agent bevacizumab [12] or alkylating nitrosourea agent lomustine [12, 13]. However, the effects of these compounds on bringing clinical benefits to patients remain largely unproven. No known targeted therapy is available to patients. As such, the survival rate of GB has not seen a significant improvement despite intense research efforts, underscoring an unmet clinical need in managing GB.

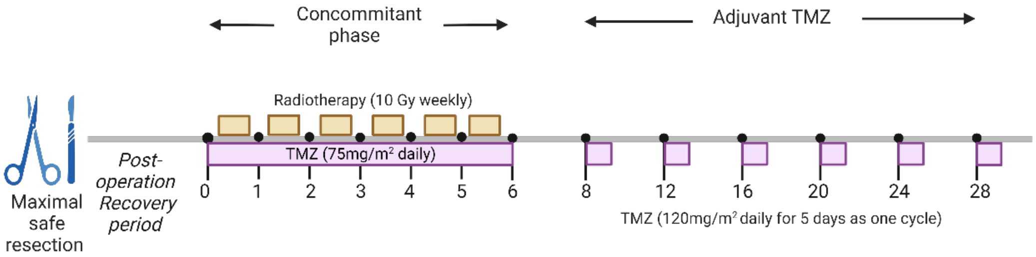

Figure 1. Standard treatment of primary GB

The timeline here depicts the major events during the standard treatment of primary GB, which entails maximal safe resection coupled with concurrent TMZ and radiation therapy (for 6 weeks). This is followed by the adjuvant TMZ treatment, which often lasts for at least 6 months (Created with Biorender.com).

1.2 Genetic alterations in primary glioblastoma

Early cytogenetic analyses identified frequent large-scale genetic lesions, including chromosomal gains in 7p (harboring the epidermal growth factor receptor or *EGFR* locus) and chromosome 10q loss (harboring the Phosphatase and tensin homolog or *PTEN* locus) [14], providing the first potential mechanistic link to the high expression of *EGFR* and low expression of *PTEN* commonly observed in GB patients. The advent of high-throughput genetic profiling approaches has further expanded the catalog of genetic lesions in GB in a genome-wide, unbiased fashion. GB is the first cohort of tumors that was comprehensively sequenced by The Cancer Genome Atlas (TCGA), leading to landmark GB molecular profiling studies in 2008 [15] and 2013 [16]. These TCGA studies revealed commonly affected signaling pathways implicated in GB's molecular pathogenesis and set the stage for the subsequent tumor classification schemes proposed later. In this section, I will first review the commonly mutated pathways in GB and its the molecular classification schemes.

1.2.1 Receptor Tyrosine Kinase (RTK) and its downstream pathways

The RTK-PI3K-Akt-mTOR pathway regulates many vital cellular processes in normal and tumoral settings. RTKs bind extracellular signals, such as growth factors or cytokines, to tightly regulate different downstream cellular processes, including cell growth and proliferation, in response to these extracellular cues. Mutations in this pathway disrupt the intricate balance between extracellular cues and proper cellular response, thereby driving the activation of downstream survival and proliferation pathways such as the Ras-MAPK and the PI3K-Akt-mTOR pathways [17]. Like in other cancer types, RTKs are commonly upregulated in GB. For instance, mutations and amplifications of *EGFR* occur in around 45-57% of patients, making it the most frequent RTK aberration in GB [15, 16]. In addition, about 70% of the patients with *EGFR* amplifications express a constitutively active mutant form known as *EGFR*vIII, in which the exons encoding the extracellular region of *EGFR* were deleted. Other frequent RTK mutations include the amplifications of platelet-derived growth factor receptor A (*PDGFRA*) (13%) (TCGA [15, 16]), vascular endothelial growth factor receptor (*VEGFR*) (6-17%) [18] and overexpression of MET proto-oncogene (*MET)* (13-30%) [19, 20]. GB samples also showed frequent mutations in genes involved in PI3K-Akt-mTOR and Ras-MAPK pathways downstream of the RTKs. The most prominent example in GB is the frequent deletion of *PTEN* (41%), a tumor suppressor negatively regulating the PI3K-Akt-mTOR pathway. Other less frequent mutations include activating mutations of *PIK3CA*, which encodes the PI3-kinase catalytic subunit p110α (around 18.3%), and deletion of *NF1* (encoding neurofibromatosis type 1). This tumor suppressor attenuates the Ras-MAPK signaling pathway in about 10% of the patients. RAS mutations, which often drive tumor development in many other types of cancer, are rare in GB (1%) [16].

1.2.2 P53 and cell cycle pathways

The *TP53* gene (encoding p53) is frequently mutated in cancers. Its promiscuous functions imply that it virtually affects every aspect of tumor development. In GB, around 23% of the samples harbor *TP53* mutations, a frequency substantially lower than that in glioma with IDH mutations, where *TP53* mutations almost always co-occur with IDH mutations, further highlighting the differences between these two glioma entities. Interestingly, the mutation frequencies of *TP53* also differ between subgroups of GB, with the proneural subtype having the highest mutation frequency (around 50%). The most common *TP53* mutations are somatic point mutations that inactivate its DNA binding domain, presumably affecting its role as a transcription factor. Other mutated genes in this pathway include *CDK4* (15.4%), occurring mutually exclusively with *TP53* mutations. The p53 pathway is mutated in around 50% of GB patients [15, 16].

Another hallmark of cancer is the deregulation of cell cycle control, leading to uncontrolled proliferation and evasion of apoptosis. In GB, the most frequent mutation in this pathway is the homozygous deletion of *CDKN2A* (encoding the cyclin-dependent kinase inhibitors p14 and p16), occurring in 57.8% of the patients. Another common deregulation is the amplification of *CDK4* (14%) and the loss of *RB1* (encoding retinoblastoma protein 1) through homozygous deletion (7.6%). In normal physiological settings, these genes regulate cell cycle progression - p16 binds to *CDK4* to inhibit its kinase activity from preventing the inactivation of *RB1*, halting the cell cycle at G1 phase [15, 16]. Thus, GB depends on the dysregulation of this pathway to fuel its rapid proliferation.

1.2.3 Telomerase reverse transcriptase (*TERT*) promoter mutations

Since their initial identifications in melanoma [21, 22], somatic point mutations in the *TERT* promoter region have emerged as critical genetic alterations in various cancer types. Interestingly, *TERT* promoter mutations seem to be highly recurrent at two hotspots immediately upstream of the *TERT* translational start site (known as C228T and C250T hotspots), creating *de novo* binding sites for ETS factors (E26 transformation specific), likely augmenting *TERT* expression in tumor cells [22]. In GB, the mutation frequencies of these two hotspot *TERT* promoter mutations are around 83% and are associated with worse disease outcomes [23].

1.2.4 Primary and recurrent GBs have similar genetic profiles

Sequencing studies analyzing newly diagnosed versus recurrent GBs showed that they have similar mutation profiles, i.e., most of the mutations in key tumor genes in the newly diagnosed tumors are retained upon recurrence [24-26]. Along the same line, clonal analyses of newly diagnosed and matched recurrent GB samples revealed that tumor relapse is driven by pre-existing oligoclonal populations in primary tumors, arguing against clonal selection events at recurrence [27]. An exception is the TMZ-induced hypermutated phenotype, which results from mutations in genes related to DNA repair, leading to increased mutation burdens upon relapse. However, this hypermutated phenotype is relatively rare in IDH-WT GB (<10% of recurrent GB) but more common in secondary glioma with IDH mutations [28].

1.2.5 Molecular subtypes of GB

With the genomic and epigenomic profiling emerging from these seminal studies, one relevant question is whether these genetically diverse GB samples can be organized into distinct molecular subtypes, forming the basis to influence disease outcomes through the identifications of clinically relevant prognostic and predictive markers for targeted therapy.

One of the first systematic attempts to classify glioblastoma based on genetic profiling data was by Phillips and colleagues in 2006, who performed expression profiling in high-grade glioma (HGG) samples and classified them as proneural, proliferative and mesenchymal subtypes [29]. They reported that the proneural subtype had a better prognosis compared to proliferative and mesenchymal subtypes. However, the observed survival advantage is likely due to the inclusion of IDH-mutant high-grade glioma (HGG) samples under this classification scheme. In a joint effort of Verhaak and colleagues, along with The Cancer Genome Atlas (TCGA) consortium, they further refined the GB transcription-based profiling scheme by overlaying it with TCGA mutation data and established 4 transcriptional subtypes, namely, proneural (PN) neural (NE), classical (CL) and mesenchymal (MES). Each subtype is associated with a distinct set of genetic abnormalities and, to a certain extent, clinical behavior, including survival and treatment outcomes [30]. Yet the subtype-specific clinical relevance identified by this study was again confounded by the *IDH* mutation status, particularly within the PN subtype. This transcriptome-based subtyping scheme was further revised to include only IDH-WT and tumor cell-intrinsic gene signatures, leading to the elimination of the NE subtype, which potentially is of non-tumor origin [31]. To sum up, PN-GB showed a higher frequency of focal amplifications of *PDGFRA* and genes involved in oligodendrocyte development, such as *SOX10, OLIG2* and *NKX2-2* [31-33]. CL-GB is associated with a high-level amplification of *EGFR* and a higher frequency of *CDKN2A* deletions. *TP53* mutations are less frequent in this subtype. Genes and pathways related to neural stem or precursor cells are highly expressed in CL-GB, including Nestin (*NES*), *SOX9*, and Notch and Sonic Hedgehog pathways. MES-GB is often associated with *NF1* deletions. Unlike PN and CL-GB, MES-GB does not resemble neural cells but expresses genes involved in immune cell infiltrates or cells from the brain mesenchyme. Indeed, this subtype is also characterized by an increase in immune cell filtration compared with PN and CL-GB. While Wang and colleagues showed that the enhanced immune cell infiltration in MES-GB can be attributable to the *NF1* inactivation of tumor cells in this subtype and hence is a tumor-cell directed event [31], accumulating evidence is now suggesting that the tumor microenvironment and the signaling cues from stromal cells also play a role in mediating the MES transition [34, 35].

Additional schemes of GB classification have been based on DNA methylation data. IDH-mutant glioma samples possess a distinct methylation subtype called the glioma-CpG island methylator phenotype (G-CIMP) [36]. In adult IDH-WT glioma samples in which G-CIMP is absent, Sturm et al. further classified these samples into RTK1, RTK2, and mesenchymal (MES) subtypes, roughly corresponding to the TCGA-PN, TCGA-CL and TCGA-MES transcriptional subtypes, respectively [37]. The overlaps between these two classification schemes suggest that these three subtypes are the most stable, predominant GB subtypes [38]. This methylation-based classification was further extended to include pan-glioma samples in a study by Ceccarelli et al., who identified mesenchymal-like, classical-like and LGm6 subtypes within the IDH-WT, high-grade glioma samples [39]. In a more recent DNA methylation subtyping encompassing all the tumors in the CNS, Capper et al. identified similar methylation subtypes within the high-grade, IDH-WT GB [40]. These methylation subtypes are now being implemented in aiding the accurate diagnosis of CNS tumors [41].

1.2.6 Clinical relevance of molecular subtyping in GB

The advances in molecular classifications based on transcription or DNA-methylation profiles are important milestones in the field. Through these molecular classifications, intertumoral heterogeneity was charted in GB, revealing potential genetic dependencies of each subtype. It also reinforced some other older hypotheses regarding GB pathogenesis. For example, the resemblance of molecular subtypes to different populations of glial cells implied a parallel between the progression of GB and normal neural stem cell (NSC) development [15, 29, 30].

Nevertheless, molecular classification schemes have yet to provide significant improvement in wider clinical applications. For example, while it has been consistently reported that MES-GB has worse survival, such differences between subtypes are indeed marginal, casting doubts on the clinical use of these classification schemes within the universally rapidly fatal IDH-WT GBs. Notably, the genetic profiles of the molecular subtypes do not seem to correlate well with the efficacy of targeted therapy. For instance, despite their success in lung cancer, *EGFR* inhibitors failed to provide clinical benefits to GB patients with *EGFR* amplifications [42, 43]. Similar failures were also reported in other targeted therapies, such as those targeting mTOR [44]. While it waits to be seen whether improved brain penetration of these targeted therapies will provide additional benefits to patients [45], it also argues against single genetic driving events in each molecular subtype. Indeed, heterogeneity within each transcriptional subtype, particularly within the PN subtypes [39], has been consistently observed. In addition, plasticity exists within different GB subtypes, particularly following standard primary therapy [29, 31, 46]. Hence, the underlying cause for the inefficacy of targeted therapy might stem from the nuanced intra-tumoral heterogeneity and dynamic cellular architecture within each subclass, which is often averaged out and dismissed in bulk transcriptomic analysis. Further understanding of the processes governing intra-tumoral heterogeneity holds promise for better therapeutic strategies in GB.

1.3 Cancer stem cell hypothesis in Glioblastoma

The cornerstone of our understanding of the intratumoral heterogeneity or phenotypic plasticity in GB is the brain tumor stem cell (BTSC) hypothesis, which postulates a hierarchical arrangement of tumor cells akin to that of normal stem cells and their progenies, with the top of this hierarchy occupied by tumor-initiating BTSCs with self-renewal properties [47-49]. Recent advances in single-cell transcriptomic profiling studies in GB have provided strong evidence supporting the existence of BTSCs in human patient materials and discovered their phenotypic plasticity, orchestrated by transcriptional networks and pathways critical in normal tissue stem cells. This phenotypic plasticity manifests itself as functional heterogeneity in response to microenvironmental changes. In this section, the intratumoral heterogeneity of GB will be examined through the lens of the BTSCs.

1.3.1 Adult Neural Stem Cells

The BTSC hypothesis is based on the premise that brain tumor development mirrors that of normal NSCs. Using human patient samples, Lee et al. provided experimental evidence that adult NSCs in the subventricular zone (SVZ) harboring driver mutations are potential cells-of-origin of GB [50]. Surprisingly, the presence of stem or progenitor populations in normal post-natal brains is a relatively recent concept, as it was widely held that mammalian brain development only takes place at the embryonic stage (reviewed in [51]). This notion was challenged following the discovery of post-natal neurogenesis in rodent subventricular zone (SVZ) and dentate gyrus (DG) in the 1960s [52] and later in song birds [53], providing the first indications that self-renewing neural precursor cells exist in adult brains. Reynolds and Weiss later validated the presence of these precursor cells in 1992 when they successfully isolated and maintained cells from the adult murine SVZ and cultured them as self-organizing neurospheres in an undifferentiated state. They also proved that these neurospheres displayed important stem cell features *in vitro*, including self-renewal properties and the ability to differentiate into astrocytes and neurons [54].

We now know that adult NSCs reside in two stem cell niches, namely the SVZ in the lateral ventricle and the subgranular zone (SGZ) in the dentate gyrus (DG) of the hippocampus (reviewed in [55]). **Figure 2** shows a simplified scheme of the differentiation pathways of adult neurogenesis and gliogenesis. In the SVZ, remnants of embryonic NSCs persist in adulthood to form adult NSCs pool in these brain stem cell niches. They show morphological and molecular characteristics reminiscent of astrocytes (hence they are also known as type B astrocytes in SVZ); however, they possess self-renewal properties and are the precursors of neurons [56] and glial cells, including astrocytes and oligodendrocytes [57, 58]. They expressed *GFAP*, BLBP*/FABP7* and other glutamate transporters and receptors such as GLAST (known as *SLC1A3*) or different glutamate receptors (mGluR1-5) [59, 60]. Usually, they remain in a slow-cycling quiescent or dormant state and are not depleted by anti-mitotic agents, in contrast to other faster cycling progenitors [56]. However, upon activation, they can give rise to fast-cycling immediate progenitor cells destined to differentiate to either the neuronal lineage (neuronal IPC) or the fate-restricted oligodendrocytic lineage (oligodendrocyte precursor cells, OPC) upon appropriate expression of lineage transcription factors (**Figure 2**). For example, the expression of Ascl1 initiates adult neurogenesis, whereas the expression of Olig2 and Sox10 specify cell fate toward oligodendrocytic differentiation. The presence of an astroglial progenitor cell population is debatable, and astrocytes can arise from either directly type B astrocytes by asymmetric cell division, or from a glial progenitor population.

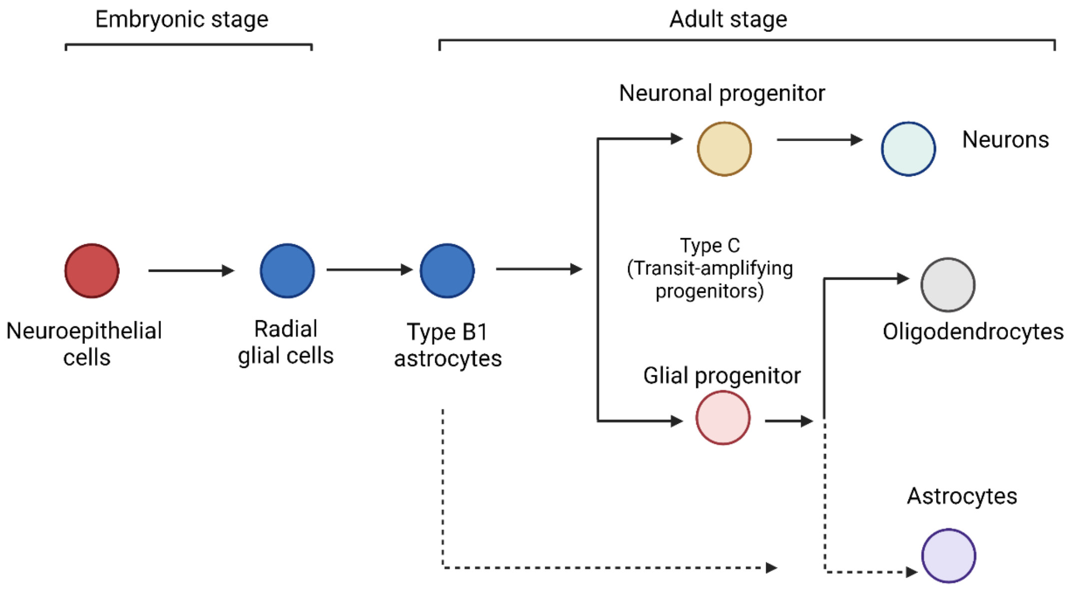

Figure 2. A model of the adult NSC hierarchy in the subventricular zone (SVZ)
In the adult SVZ, some of the embryonic NSCs or radial glial cells remain in the SVZ to become the adult NSCs, also known as Type B1 astrocytes. They are the multipotent stem cells in the SVZ, which can give rise to the fast-cycling Type C cells (transit-amplifying progenitors, TAP or immediate progenitor cells, IPC) destined to go down to either the neuronal lineages (upper branch) or the towards glial differentiation (lower branch). It remains unclear whether there is a progenitor cell population for adult astrocytes (dashed line). Alternatively, astrocytes can also be regenerated from Type B1 astrocytes directly. This figure is highly simplified to provide a basic differentiation hierarchy in adult neurogenesis and gliogenesis. The differentiation of adult NSCs is also complicated by other factors, most notably the regional heterogeneity of adult NSCs within the SVZ (Figure was modified from [61] and redrawn with Biorender.com)

1.3.2 Quiescence of Neural Stem Cells

Unlike embryonic NSCs, adult NSCs only give rise to differentiated progenies when necessary. For example, NSCs can be activated in response to stroke [62] or under pathological demyelinating conditions in multiple sclerosis [63]. This tight control of differentiation lies in their inherent capacity to maintain self-renewal by entering a slow-cycling or a quiescent state. In fact, stem cell quiescence is an approach commonly used by many other normal tissue stem cells to safeguard their self-renewal potentials [64-66]. By staying in an inactive metabolic state, they are spared from the premature exhaustion of proliferation and self-renewing capacity to maintain the pool of progenitor cells. Single-cell transcriptomic analyses of SVZ NSCs showed they are heterogeneous in terms of their proliferative capacities, with the quiescent NSC (qNSC) at the root of the lineage progression towards more activated NSC or differentiated states [67, 68]. The qNSCs are characterized by their elevated lipid biogenesis pathways, likely indicating their dependence on these pathways for energy utilization. Upon activation, they turn on the expression of genes involved in protein synthesis and cell cycle progression, including Myc and Ascl1 for their fast-cycling states (**Figure 3**) [69, 70].

The quiescent state is actively maintained through many cell-intrinsic determinants. For example, they are controlled by different lineage transcription factors, including Sox9 and Id2 [68]. These transcription factors halt cell cycle progression and maintain a slow-cycling state [71]. In addition, qNSCs have a higher lysosomal activity than activated NSCs [72, 73]. It has been recently demonstrated that the increased lysosomal activity in qNSCs serves to degrade *EGFR* to prevent its activation, suggesting that the NSC quiescence is an actively maintained process [72, 73].

Interestingly, the qNSCs are also characterized by enhanced pathway activities related to cell-cell communications, underscoring that the qNSCs are actively interacting with their microenvironment. For example, they express receptors for critical pathways such as BMP and Notch [74]. Moreover, they also have altered exosomal profiles compared to the aNSCs, suggesting communication of qNSC mediated by exosomes. Interestingly, the inhibition of exosomes release from qNSC seemed to drive their re-entry into the cell cycle, underscoring the roles of exosomes in maintaining the quiescence state [75]. Additionally, qNSCs express various cell adhesion proteins and receptors, highlighting that the qNSCs are sensitive to changes in the local microenvironmental cues so that they can return to activated states as needs for neurons and glial cells arise. For example, qNSCs often express high levels of vascular cell adhesion molecule-1 (VCAM1) to monitor the level of pro-inflammatory cytokine IL-1β [76], which is released during neuroinflammation and to activate the proliferation program of the NSC [77].

Overall, the development of adult NSCs follows a strictly hierarchical, unidirectional manner, with the differentiation capacity limited by stem cell quiescence. Quiescence is an actively maintained state orchestrated by intrinsic and extrinsic determinants (**Figure 3).**

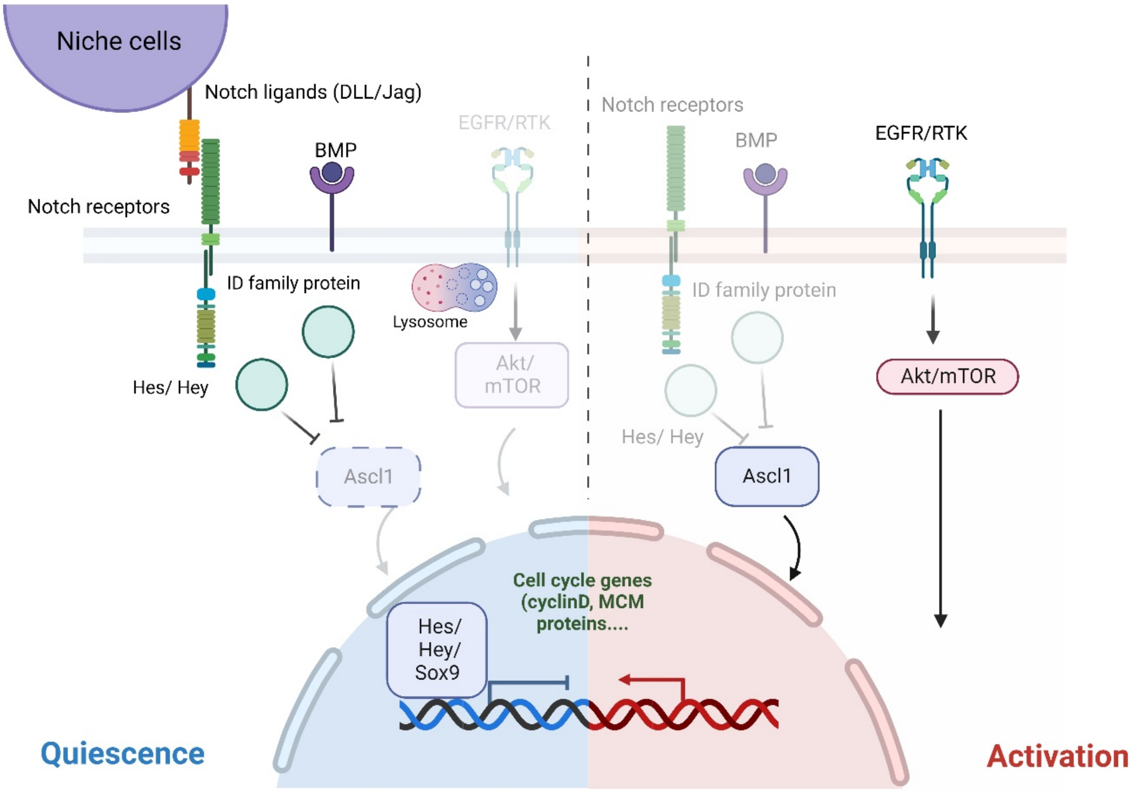

Figure 3. Molecular determinants of adult NSCs quiescence

NSC quiescence is actively maintained through extracellular and intracellular determinants. Extracellularly, the quiescence state is sustained by activating the Notch and BMP signaling pathways. For example, niche cells such as activated NSCs in the SVZ protrude Notch ligands such as Dll/Jag1 and bind to the Notch receptors on qNSCs to activate the Notch pathway in the qNSCs. Hes and Hey family TFs downstream of the Notch pathway then repress Ascl1 to prevent the activation of cell cycle genes such as cyclin-D1. When Notch signaling is deactivated in NSCs, or when relevant growth factors bind to the qNSC, they trigger the re-activation of cell cycle genes via Ascl1 or through the PI3K-Akt-mTOR pathways downstream of the RTK. The quiescence of NSCs prevents the premature exhaustion of the pool of stem cells in the SVZ, ensuring that they can be re-activated as needed. (Figure was modified from [74] and redrawn with Biorender.com)

1.3.3 A historical perspective of the brain tumor stem cell hypothesis

The breakthrough in the field of NSC biology propelled the development of cancer stem cell (CSC) hypothesis in brain tumors. Specifically, the central question here is whether we can also identify a similar hierarchy in NSCs, wherein a group of self-renewing tumor cells (BTSCs) produce other tumor cells in GB. The seminal work by Bonnet and Dick provided the first *in vivo* evidence of the presence of “leukemia-initiating cancer cells” in acute myeloid leukemia [78]. Their discovery sparked the quest for CSCs in other cancer types, leading to the CSC hypothesis of tumor initiation and development in multiple cancer types, including brain tumors. In addition, better characterization and surface marker-based isolation methods for NSCs also prompted the search for stem-like tumor cells that propel brain tumor development. Using CD133 as a marker, Uchida and colleagues developed the first marker-based isolation method for NSCs and isolated them from fresh human fetal brains. They further showed that these sphere-forming CD133-positive cells could engraft, proliferate and differentiate when intracranially transplanted into immunodeficient mice [79]. This led to the breakthrough in the field of BTSC by Singh et al. from P. Dirks' laboratory, who adopted Uchida's CD133-based NSC isolation method and prospectively isolated NSC-like tumor cells from human patient samples [80]. They further showed that these CD133-positive tumor cells, but not the CD133-negative counterparts, were tumorigenic *in vivo.* Notably, the tumors arising from CD133-positive BTSCs recapitulated the histological features of the parental tumors in immunodeficient mice [81]. Their findings suggest the roots of brain tumors can be traced back to a group of NSC-like tumor cells, and these self-renewing cell populations could give rise to more differentiated-like progeny. Moreover, the ability of these BTSCs to re-generate parental tumors seems to suggest that a hierarchy similar to that of NSCs also exists in GB. This hierarchical arrangement of BTSCs was further dissected unbiasedly (i.e., without pre-selection of BTSCs based on marker expression) by Lan et al. from the same research group, where they performed *in vivo* lineage tracing of barcoded patient-derived BTSCs. They identified a cellular hierarchy of proliferation status starting from the slow-cycling quiescent GSCs, which subsequently yielded proliferative progenies, reminiscing the hierarchy observed in normal NSCs [82].

1.3.4 Pathways or developmental programs driving brain tumor stem cell state

Tying in with the resemblance to normal NSCs, many critical pathways that drive or maintain NSCs are co-opted by BTSCs. Importantly, this self-renewal state is also governed by transcription factors (or the networks thereof) critical in maintaining the stemness state, thereby exacerbating the aggressive phenotypes driven by the developmental programs [83] .

1.3.4.1 Notch pathway

Notch signaling is a highly conserved pathway that is crucial in various developmental processes [84], in particular stem cell maintenance and cell fate decisions in different anatomical areas [85]. The activation of this pathway is mediated through cell-cell interactions between a signal-sending cell, which provides Notch ligands Jagged1 and 2 and Delta-like ligands (Dll1 to Dll4), and a signal-receiving cell, to which the ligands to the Notch receptors (Notch 1- 4) bind [86]. Binding onto Notch receptors results in their conformation alterations, leading to the release of the active, intracellular form of Notch receptor known as Notch intracellular domain (NICD) through sequential cleavages by members of the disintegrin and metalloproteinases family (ADAM) and by the γ-secretase complex. Non-membrane bound NICD can then migrate to the nucleus, where it becomes associated with RBPJ, to activate the expression of Notch target genes through the recruitment of Mastermind-like protein (MAML), a transcriptional co-activator or other chromatin remodeling factors CBP/p300 [87]. Most notable Notch target genes include the transcriptional repressors Hairy Enhancer of Split (Hes) family proteins and HES-related proteins (Hey), which play key roles in cell-fate decisions [88].

The Notch pathway is highly context-dependent and yields different transcriptional outputs depending on cellular or physiological contexts. In NSCs, Notch activity maintains the pool of adult NSCs in the neurogenic niches [89, 90]. Specifically, high Notch activity sustains NSCs sustains in a quiescent, non-differentiated states through the expression of Notch target genes such as Hes and Hey family proteins [91, 92]. Notch pathway also prevents the expression of activation and pro-differentiation genes such as Ascl1. In contrast, the reduction of Notch activity pushes the quiescent cells back into the cell cycle, resulting in a transient increase in proliferation and differentiation towards neuronal differentiation [93-96]. Meanwhile, the NSCs pool can also be maintained in an undifferentiated state via Notch receptor and ligand-mediated cell-cell interaction through lateral inhibition, where the activated cells protrude Notch ligands to bind to the neighboring cells to maintain their Notch activity [97]. Likewise, the Notch pathway is vital for preserving stemness properties in BTSCs. For example, increased Notch activity in BTSCs can also lead to the emergence of a drug-tolerant persister phenotype through epigenetic modifications [98]. Hence, high Notch activity is essential for the tumorigenic properties and resilience to therapy in BTSCs.

1.3.4.2 Wnt pathway

Another pathway important for maintaining BTSC stemness is the Wnt pathway. The binding of Wnt ligands initiates canonical Wnt signaling to membrane-associated frizzled (FZD) and low-density lipoprotein receptor-related protein (LRP) families. Furthermore, their activation stabilizes β-catenin and promotes its nuclear translocation to activate downstream target genes such as c-Myc and cyclin D1 [99]. Hence, the Wnt pathway promotes the proliferation of the NSCs and their differentiation toward neurogenesis [100]. In BTSCs, Wnt pathway activity is associated with a broad spectrum of GSCs phenotypes, including self-renewal, invasion and resistance to therapy [101, 102]. Interestingly, dual inhibition of Notch and Wnt pathways in BTSCs potentiates their neuronal differentiation in *in-vitro* models, underscoring the potential of targeting these two developmental pathways in diminishing BTSC tumorigenic properties [103].

1.3.4.3 Core transcription circuitry are prone to be exploited by BTSCs

BTSCs also have been reported to hijack the transcriptional factor networks used in normal NSCs to maintain their cancer stem cell state. Early sporadic reports on the transcription regulation of BTSCs revealed that many of these transcription factors, such as *SOX2*, Musashi-1 [104], *GLI1* [105] and *ID1* [106], are involved in normal NSCs development or in maintaining the CSC states in other cancer types. Suva and others took a more comprehensive approach, integrated transcriptomic and epigenetic landscapes of BTSCs and showed that SOX2 controls cancer stemness in GB, *SALL2, POU3F2* and *OLIG2* [107], whose functions in the glial cell lineage progression and maintain stem cell pluripotency were well-documented. Castellan et al. recently discovered that YAP/TAZ transcriptional co-activators control the stemness states regardless of the molecular subtypes [108]. These TFs drive the BTSCs phenotypes in various ways. Some of these transcriptional factors are essential in molecular subtype reprogramming. For example, *NF1* loss regulates the *FOSL1* to mediate mesenchymal GSCs [109]. Other TFs, such as *KLF4*, directly drive the activity of NOTCH as well as *SOX2* [110]. Lastly, YAP/TAZ seems essential in potentiating self-renewal properties downstream of various oncogenic insults in transformed NSCs [108].

1.4 Plasticity of brain tumor stem cells

While similarities between BTSCs and their normal counterparts are evident, early studies showed that fluidity exists within the hierarchy of BTSCs, enabling them to exhibit phenotypic adaptation in response to various microenvironmental cues to their advantage. The plasticity of BTSCs is defined as the reprogramming of cellular states and phenotypes in response to cell-intrinsic and extrinsic cues. More broadly speaking, the plasticity of GSCs is, as Rich and colleagues summarized in their review, a measure of the potential space which these BTSCs can navigate, governed by their intrinsic genetic and epigenetic factors, as well as external perturbations such as microenvironmental factors and therapeutic pressure [111].

1.4.1 Early evidence of the plasticity of brain tumor stem cell hierarchy

Following the identification of CD133 as a glioma stem cell marker, other markers of BTSCs were proposed. These include surface markers such as CD44 and CD15 (known as Stage-Specific Embryonic Antigen-1, SSEA) (reviewed extensively in [47]). The presence of different markers for BTSCs indicate that no single marker can be employed to identify BTSCs universally. In fact, different markers appear to be enriched in BTSCs with different phenotypes. For example, CD133-positive BTSCs are associated with a more proliferative state, whereas GPD1 expression is associated with pre-existing dormant or quiescent BTSCs, which promote tumor regrowth after TMZ treatment [112]. On the other hand, CD44 marks MES-like BTSCs, suggesting that each molecular GB subtype may have its subtype-specific BTSCs [46]. Hence, it became apparent that BTSCs may assume different phenotypes or change their phenotypes based on their underlying genetic or microenvironmental contexts.

1.4.2 Resilience to differentiation cues

Another significant difference between normal stem cells and BTSCs which indicates fluidity between BTSCs' cellular states, is that they rarely fully differentiate *in vivo*. Galli et al. showed that the differentiated progenies of BTSCs *in vitro* often co-expressed markers of astrocytic (*GFAP*) and neuronal lineages (*MAP2, TUJ1*) using immunofluorescence analysis. *In vivo*, they observed that the resultant tumors were positive for progenitor/astroglial marker *GFAP* but were largely negative for the neuronal marker *TUJ1*, suggesting that BTSCs do not become terminally differentiated *in vivo*, consistent with other studies [113, 114]. The impaired differentiation of BTSCs was later demonstrated to be associated, at least in part, due to the underlying genetic abnormalities of the BTSCs. For example, BTSCs derived from the inactivation of both Trp53 and Pten in mouse NSCs were locked in a relatively undifferentiated state and were resilient toward differentiation cues [115]. In parallel, BTSCs also showed impaired methylation at the pluripotent genes, such as SOX family proteins, leading to their escape from terminal differentiation [113]. In another study by Turcan et al., the production of 2-hydroxyglutarate after IDH mutation was shown to enhance repressive histone methylation marks at the promoters of differentiation genes, creating a differentiation block in the IDH-mutant tumors [116].

The differentiation of BTSCs is further complicated by the possibility of tumor cells going up against the differentiation hierarchy. This is illustrated through the observations that cells negative for BTSC markers, such as CD133 or CD15, could also initiate tumors in immunodeficient mice, albeit at a lower potency [117, 118]. This indicates the potential acquisition of tumorigenicity *in vivo* regardless of the absence of canonical BTSC markers. Moreover, forced expression of neurodevelopmental TFs in differentiated GB cells generates GSCs with tumorigenic potentials [107]. Importantly, this dedifferentiation process can occur spontaneously or in response to changes in the TME. For instance, Al-Mayhani et al showed that tumor cells negative for NG2, a lineage marker for OPC, could restore their expression of NG2, creating an equilibrium of progenitor-like and differentiated-like cells [119]. Under treatment pressure, it has also been observed that tumor cells upregulate markers associated with stem and progenitor states [120, 121]. Taken together, these lines of evidence suggest the importance of lineage transcription factors in governing the dedifferentiation and hence the phenotypes of BTSCs.

1.4.3 Single-cell studies reinforce the concept of brain tumor stem cell plasticity in glioblastoma

The advent of single-cell transcriptomics technologies enabled the elucidation of the cellular architecture in GB, shedding light on the phenotypic diversity of BTSCs. These studies revealed the widespread presence of stem and progenitor cells within tumors [83, 122], supporting previous functional experimental evidence on the presence of GSCs. Moreover, rather than as distinct populations as previously thought, BTSCs seem to lie on a continuum of phenotypes, reinforcing the notion of phenotypic adaptations of GB cells. In addition, the development of various computational methods to delineate cellular state dynamics also enabled the prediction of the state transition dynamics within the tumors, providing a more comprehensive portrait of BTSCs' diversity in GB.

Specifically, the first systematic single-cell transcriptome profiling of GB tumor cells by Patel et al. discovered that GB tumors are composed of cells with different molecular subtypes at the single-cell level. Interestingly, intermediate states (“Hybrid-states”, as coined in their paper) were observed between different cellular states, suggestive of cell state transitions between phenotypes [123]. This is in stark contrast to the more rigid, 3-state cellular architectures observed in IDH-mutant (Oligodendroglioma with 1p/19q co-deletion, a study from Tirosh et al. [124]; Astrocytoma with *TP53*/*ATRX* mutations, a study from Venteicheret al. [125]) and H3K27M pediatric gliomas (study from Fibrin et al. [126]), where an axis could explain intra-tumoral heterogeneity from cycling proliferative NPC-like (IDH-Mut) or OPC-like (H3K27M) to the more differentiated astrocytic- or oligodendrocyte-like cells. Similarly, Neftel et al. from Mario Suva’s group charted a more comprehensive single-cell transcriptomic profile in IDH-WT tumors and proposed a 4-state model of intratumoral heterogeneity in GB. Among these 4 cellular states, 3 are related to NSC development, namely the NPC-like, OPC-like, and AC-like states [127]. The fourth MES-like state seems to arise independently, likely subsequent to the effect of the immune cell compartment on the tumor cells [34]. Each tumor is comprised of different proportions of the above cellular states. Importantly, they experimentally showed that tumor cells enriched for a particular cell state could regenerate tumors consisting of all states, further underscoring their plasticity [127]. Subsequent single-cell studies independent of Suva's group further delineated the cellular plasticity of tumor cells, proposing different phenotypic axes spanning development and injury [128] and metabolomic utilization [129]. Taken together, recent single-cell transcriptome profiling in GB cells highlight the cellular plasticity and functional diversity of the BTSCs, manifested as a gradient of phenotypes (**Figure 4**).

Besides different cellular states identified by scRNA-seq, emerging studies also revealed the potential transitions along the spectrum of cellular states. One of the most frequently observed axis in describing the phenotypes of BTSCs is the cycling behavior if tumor cells. Using RNA-velocity on the GB patient scRNA-seq, Wang et al. [130] identified a developmental transition from the quiescent, slow-cycling state to the more proliferative state, in agreement with previous publications on the presence of slow cycling state propelling tumor growth [82, 131]. Using orthotopic xenograft models injected with mutated human NSCs, it was revealed that the process of GB progression involves an NSC-like beginning and multiple steps of transcriptional reprogramming involving different lineage transcription factors, leading up to the burst of proliferative cells at the end stage [132].

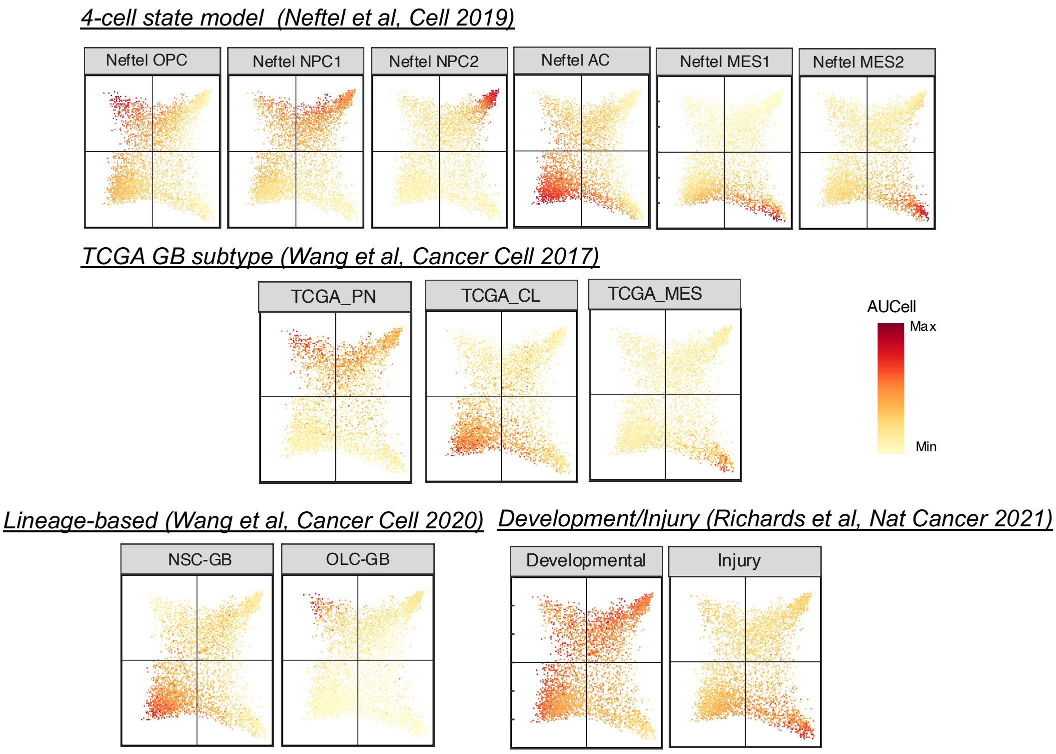

4-cell state model (Neftel et al, Cell 2019)

TCGA GB subtype (Wang et al, Cancer Cell 2017)

Lineage-based (Wang et al, Cancer Cell 2020)

Development/Injury (Richards et al, Nat Cancer 2021)

Figure 4. Phenotypic gradients of GB tumor cells

The principal phenotypic axes proposed in GB were projected on Neftel's 4-cell-state model. The figure was generated by scoring the signature scores of the proposed cell state of each cell in Neftel's dataset. Briefly, the scatter plots show the normalized AUCell score (value on the legend) for different publications. Note that these cell states exist as a gradient across the dataset. I generated the plots based on public data deposited in GSE131928.

1.4.4 Determinants of phenotypic plasticity in brain tumor stem cells

1.4.4.1 Genetics and epigenetic determinants

The underlying genetic backgrounds of the tumor cells provide a blueprint for the predominant cellular states, which ultimately manifest themselves as molecular subtypes in GB patients at the bulk transcriptpmic level. For example, each of the four cellular states identified by Neftel et al. seems to be associated with different sets of genetic alterations, largely corresponding to those observed in the TCGA transcriptomic subtypes [127]. Genetic alterations likely limit the potential space that these BTSCs can occupy. For instance, *TP53* and *PTEN* inactivation ensures the BTSCs stay undifferentiated without full-blown neuronal differentiation [115], whereas *NF1* loss might mediate the enhanced infiltration of tumor-associated macrophages, leading to the emergence of MES-like phenotypes [31].

Another constraint of phenotypic diversity of BTSCs comes from their epigenomes. This is illustrated by the recent work of Parada and colleagues, who observed that different glial lineages with identical underlying genetic mutations yielded tumors with strikingly different phenotypes – the OPC-derived tumors characterized by high *SOX10* expression are bulky and circumscribed, whereas the NSC-derived tumors characterized by low *SOX10* expression and high *SOX9* expression were more aggressive and infiltrative [133]. This study highlights the influence of parental lineage identity and memory on tumor development. However, it becomes more evident now that this lineage constraint is somewhat flexible. Under cellular stress or therapeutic insults, the epigenomes are actively remodeled to cope with the changing tumor microenvironment contexts. For example, treating BTSCs with dasatinib, an RTK inhibitor, induces a drug-tolerant persister state through upregulating transcription factors mediating the Notch pathway [98]. More recently, single-cell methylome studies identified hypomethylation of PRC2 targets in BTSCs, consequently preventing the expression of lineage-committed genes. Furthermore, taking advantage of endogenous heritable DNA methylation changes as barcodes, they proposed a less structured BTSCs hierarchy, where dedifferentiation events occur concurrently to maintain the pool of BTSCs [134]. However, the critical transcription factors that can mediate the transcending of lineage identity in a clinically relevant context remain elusive.

1.4.4.2 Tumor microenvironment

Finally, the tumor microenvironment also strongly affects the phenotypes the BTSCs can assume. The impact of immune cells on the progression of GB is increasingly appreciated. Recent single-cell studies showed that the immune landscape of IDH-WT GB is characterized by the increased infiltration of monocyte-derived macrophages from the peripheral blood, in stark contrast to IDH-mut GB, where brain-resident microglia take up a larger proportion of tumor-associated myeloid cells [135, 136]. Tumor-associated macrophages (TAM) are generally considered immuno-suppressive, and their relevance in GB progression has been demonstrated [137]. TAMs release a host of different cytokines to influence the behavior of tumor cells and other stromal cells in the TME. For example, TAMs enhanced tumor cells' proliferative and invasive potentials by releasing TGF-β1, IL-1β and *CCL2* [138, 139]. On the other hand, GB cells also release chemoattractants such as *POSTN* and *CCL2* to enhance the recruitment of TAMs. To further complicate the intricate cross-talks between TAMs and tumor cells, it was recently reported that immune attack results in the re-configuration of the methylation landscape of tumor cells, rendering them similar to myeloid cells through the induction of *IRF8* [34]. This process of “myeloid mimicry” of tumor cells underscores the entangled tumor-TAM relationship that needs further dissection [34].

Interestingly, while both glioma types are characterized by sparse infiltration of T-cells (<10%), IDH-mut GB show an even lower abundance of T cells compared to IDH-WT tumors, likely owing to the suppression of T cells by 2-hydroxyglutarate [136, 140]. In IDH-WT, BTSCs have a lower expression of antigen-presenting molecules than more differentiated cells, suggesting that the stem cell compartments are likely protected from immune surveillance by maintenance at an immunologically quiet state [141].

1.4.5 Therapeutic implications of brain tumor stem cell plastic model

The BTSC model of GB progression provided a conceptual framework for understanding treatment failure and shed light on the potential strategies to combat GB. Indeed, resilience to therapeutic pressure is arguably one of the most common functional properties of BTSCs. For example, Bao et al. reported that CD133-positive BTSCs were resistant to radiotherapy through upregulation of DNA repair pathways [142]. Moreover, the quiescent nature of the BTSCs also enables them to withstand standard therapy, which preferentially ablates fast-cycling cells within tumors [131]. This led to the early expectation in the field that by identifying the vulnerabilities of these BTSCs, one can remove the root cause of recurrence and treatment failure. However, a recent pre-clinical study showed that CAR-T treatment targeting CD133, the most prominent “marker” of BTSCs, only provided temporary treatment effect and tumors inevitably relapsed after treatment subsided [143]. While this is mainly attributable to the fact that not all BTSCs universally express CD133, it is also equally likely that the fluidity of BTSCs confers them additional routes to escape therapeutic pressure. This is illustrated by the observations that TMZ treatment induces the dedifferentiation of tumor cells, which may result in the emergence of therapy-resistant BTSCs [120]. In addition, BTSCs can also rewire their metabolic profiles to cope with the treatment pressure, underscoring the dynamic nature of BTSCs in response to therapeutic insults [112].

One viable strategy to combat this intra-tumoral heterogeneity is through the use of combinatorial therapy to target different cell states within the tumors. Wang et al. showed *in vitro* synergistic cytotoxic effects by targeting both the slow-cycling mesenchymal and the fast-proliferating proneural state [130]. Suva and Tirosh suggested a “state-inducing” treatment strategy, where BTSCs state was first induced to a more manageable state amenable to available therapeutic options [144]. First, this strategy will require a better understanding of the phenotypic plasticity resulting from different lineage transcription factors. Second, understanding the cell state transition is also essential to design therapeutic strategies that can maximally capture different cellular states within the tumors.

1.5 SOX10

1.5.1 A general introduction to SOX family Transcription Factors

SOX or **S**RY-related HMG B**ox** proteins are a group of transcription factors (TF) instrumental to cell fate determination in mammal embryonic and post-natal development. The first member identified within this family of TF was Sry, or sex-determining region Y, which plays a key role in male-sex determination in mice and humans [145, 146]. Afterward, other structurally similar TFs were identified [147], which were characterized by their sequence homology with the Sry high mobility group (HMG) DNA-binding domain. This SOX specific domain recognizes the consensus motif (A/T)(A/T)CAA(A/T)G in the minor groove of DNA [148]. The SOX family comprises around 20 transcription factors in vertebrates, categorized into 8 groups (SoxA through SoxH) based on their gene structures and HMG domain similarity among family members.

SOX proteins are widely present in eukaryotic cells to exert various functions, from maintaining self-renewal to mediating differentiation (**Table 1**), even though they largely bind to the same consensus elements. This is best illustrated in the development of NSCs where *SOX2* controls multipotency and *SOX4* and *SOX11* direct neuronal differentiation. There are three guiding principles that SOX family proteins use to exert their regulatory functions in diverse cellular processes. First, SOX family TFs rarely work alone and their functions are determined by their combinations with other DNA-binding partner TFs. As such, these combinations allows SOX TFs to bind to their target regions specifically to exert different regulatory functions in concert with their partners [149]. Second, being a minor-groove binding TF, SOX binding induces the bending of the DNA and hence changes the architecture of the regulatory elements, including both the promoters and the enhancers [150, 151]. Meanwhile, SOX proteins also interact with other transcriptional co-factors, in particular histone modifiers and chromatin remodelers such as CBP/p300 [152]. Finally, SOX TFs can also act as pioneering factors that prime their potential target genes for subsequent activation. Specifically, SOX TFs often pre-bind to the target genes to induce a more accessible chromatin structure through DNA bending mentioned above, thereby allowing other necessary transcription factors to bind sequentially so the genes they regulate can be activated in a temporal and lineage-specific manner. This is exemplified by neuronal differentiation, where *SOX3* pre-binds to target genes destined to be expressed at the later stage of neuronal differentiation [153].

Table 1: List of SOX Transcription factors relevant to NSCs development

SOX Group	Gene	FUNCTIONS
SOXB1	*SOX1*	Controls NSC self-renewal. A marker of NSCs in SGZ.
	SOX2	Controls NSC self-renewal. A marker of NSCs in both SVZ and SGZ.
	SOX3	Pre-binds neuronal genes destined to be activated by Sox11 [154]
SOXB2	*SOX14* *SOX21*	Take part in neuronal terminal differentiation in mouse brains by counteracting the self-renewal functions of SoxB1 TFs [155, 156]
SOXC	*SOX4* *SOX11*	Direct NSC differentiation towards neuronal lineage. Binds to open-chromatin marked by SOX3. Expression is the highest in neuroblasts and decreases upon terminal neuronal differentiation [154, 157, 158]
SOXD	*SOX5* *SOX6*	Take part in neuronal differentiation and migration of neuroblasts [159]. In oligodendrocytes development, they compete with *SOX10* for binding sites and act as negative regulators of oligodendrocyte differentiation [160]
	SOX13	Seems to show functional redundancy with Sox5 and Sox6 [161]
SOXE	*SOX8*	Plays a minor role in OPC specification [162] but synergizes with *SOX10* in exerting a prominent role in myelination in oligodendrocyte differentiation [163]
	SOX9	Maintains self-renewal properties in NSCs from SVZ [164]. Partners with NFIA to mediate astroglial development. Specifies NSCs towards oligodendrocytic fate, and the expression becomes negatively regulated by *SOX10* in the later stage of oligodendrocyte development
	SOX10	Presides over the gene regulatory networks governing oligodendrocyte proliferation and maturation and expresses through the entire development of oligodendrocytes.
SOXF	*SOX17*	Takes part in myelination during the later stages of oligodendrocyte differentiation [165]

1.5.2 Gene structure of *SOX10* and its expression in normal tissues

The SOX TF covered in this thesis is *SOX10*, which belongs to the SoxE group proteins. **Figure 5** shows the gene structure of *SOX10*. SoxE TFs, which include *SOX8*, *SOX9* and *SOX10*, are characterized by a dimerization domain N-terminal to the HMG-box, which allows homodimerization or heterodimerization with themselves or with other TFs. Another structural feature of SoxE TFs is the presence of a transactivation domain in the middle (TAM), which synergizes with the transactivation domain at the C-terminal [166]. *SOX10* is also subject to post-transcriptional and post-translational regulation, as detailed in the **Figure 5**. *SOX10* is well-conserved between humans and mice, with mouse Sox10 sharing 98% amino acid sequence homology with its human counterpart. *SOX10* takes part in lineage specification during the development of neural crest cells (NCC) and oligodendrocytes in the CNS. In NCC, SOX10 promotes their differentiation toward melanocytes and Schwann cells [167]. In NSCs, the expression of SOX10 promote the differentiation toward oligodendrocytes [168].

Haploinsufficiency of *SOX10* has been associated with the Waardenburg-Shah syndrome, a genetic disorder characterized by enteric nervous system abnormalities and skin pigmentation reduction. In addition, *SOX10* mutations have also been shown to be associated with severe periphery demyelination syndromes. Further *in vivo* work confirmed that *SOX10* mutations are causative factors of these diseases [169], whereby truncating mutations of *SOX10* impair its DNA-binding and transactivation capacity to activate lineage specification molecules essential for the differentiation of NCCs into melanocytes [170, 171].

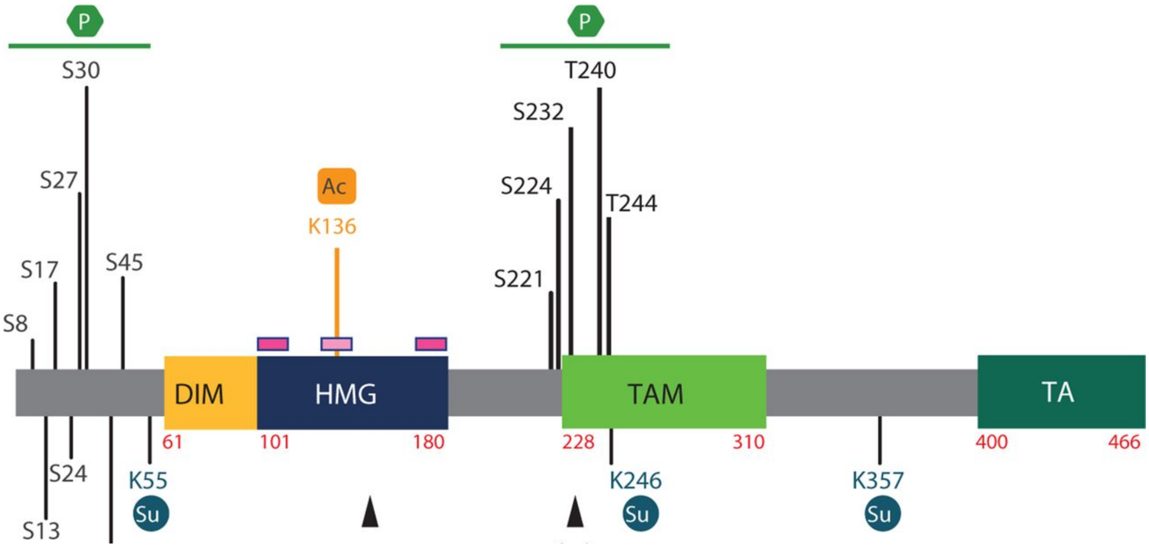

Figure 5. Gene structure of *SOX10*

The schematic drawing above depicts the gene structure of human *SOX10*, highlighting its functional domains and potential sites of post-transcriptional regulation. It consists of a dimerization domain (DIM), a high-mobility box domain (HMG), a transactivation domain in the middle (TAM) and a transactivation domain (TA) at the C terminal. The numbers indicate amino acid residues. SOX10 is subject to various post-transcriptional modifications, including phosphorylation (P) at various serine/threonine residues, acetylation (Ac) at lysine residue K136 and SUMOylating (Su) at different lysine residues. Mouse Sox10 shares 98% amino acid sequence homology with human SOX10. (Figure taken from Pingault et al., 2021 [172])

1.5.3 Positive regulatory functions of *SOX10*

SOX10 exerts its lineage commitment functions by establishing a gene regulatory network (GRN) to activate a cascade of other TFs to activate genes involved in the proliferation and differentiation of these cell lineages. A prime example of this is in melanocytes, wherein this GRN is activated when *SOX10* pairs up with *PAX3* to bind directly to the *MITF* promoter to activate its expression [173]. *MITF* then further interacts with *SOX10* to drive the transcriptional programs involved in melanocyte differentiation and melanin synthesis. In NSCs, oligodendrocytic fate-restricted NSCs (or oligodendrocyte progenitor cells, OPCs) stabilize their Olig2 expression to induce *SOX10* expression [174]. These two TFs regulate the specification, proliferation and maturation of oligodendrocytes, driven by the sequential activation of *PDGFRA*, NG2/CSPG4 and, finally, pro-myelination genes such as *MBP* and *PLP1*. It is important to note that while *SOX10* can bind to the promoter regions of its target genes such in the case of *MITF*, it usually exerts its regulatory functions by altering the chromatin landscapes. Indeed, most of the

SOX10 binding sites fall onto distal regulatory elements, such as the enhancers of its target genes in melanocytes and myelinating glial cells [175, 176]. Meanwhile, *SOX10* also recruits other chromatin remodelers to these distal regions. In melanocytes, Brg1 (SMARCA4) has been shown to interact with *SOX10* [177]. In oligodendrocytes, *SOX10* interacts with chromatin remodelers such as Ep400 and Chd7 to mediate the expression of pro-myelination genes during the maturation of oligodendrocytes [178, 179].

1.5.4 Repressor functions of *SOX10*

Besides its role as a transcriptional activator, *SOX10* also participates in repressor functions to ensure proper lineage commitment and prevent the fate-restricted cells from reverting to the progenitor state. In melanocytes, downregulation of *SOX10* expression increases the expression of the progenitor cell marker KIT [175, 180]. In Schwann cells, *SOX10* activates Krox20 and Zeb2 to reduce *SOX2* expression to prevent demyelination [181]. In late OPC development after lineage specification by *SOX9* and *SOX10*, *SOX10* upregulates mir-335 and mir-338 to inhibit the expression of the *SOX9*, an essential regulator for the neural progenitor cell state, to prevent de-differentiation [182].

1.5.5 *SOX10* in tumors

Perhaps unsurprisingly, *SOX10* is highly expressed in tumors which arise from the anatomical sites where *SOX10* plays a role in development. These include melanoma, schwannoma, and brain tumors, reflecting the “lineage addiction” to *SOX10* in these tumors [172]. Interestingly, *SOX10* is also expressed in tumors from other anatomical locations, including triple-negative breast cancer (TNBC), in which *SOX10* does not participate in normal development. This might suggest that *SOX10* might be able to re-express itself in other tumor types [183].

1.5.5.1 Phenotypic switch mediated by *SOX10* in melanoma

Given that *SOX10* resides at the juncture of two GRNs that control proliferation and self-renewal, and the vast network of TFs it regulates, it is conceivable that tumor cells might exploit this key node of cell identity to their advantage to mediate phenotypic transitions. The phenotypic plasticity mediated by *SOX10* is best-described in melanoma. In fact, although *SOX10* is highly expressed in this tumor type, a subset of slow-cycling but invasive melanoma samples have a lower expression of *SOX10* [184, 185], suggesting that the differences in *SOX10* expression levels may correlate with phenotypic diversity in melanoma. Further stringent transcriptomic analyses also showed that melanoma samples can be classified by their differentiation status. The proliferative, melanocytic-like samples can be de-differentiated upon treatment pressure by BRAF inhibition, the first-line targeted therapy for this tumor type [186]. Interestingly, the expression of *SOX10* decreases while that of *SOX9* increases along this process of de-differentiation, consistent with their antagonist relationship illustrated in normal and tumor cell settings [182, 187]. Indeed, *SOX10* expression is influenced by therapeutic pressure. For example, Sun et al. showed that tumor cells downregulate *SOX10* and upregulate *EGFR* in response to BRAF inhibition, leading to therapeutic resistance [188]. The importance of therapy-induced *SOX10* downregulation in tumor cells was further illustrated by Shaffer et al., showing that the loss of *SOX10* expression in melanoma cell constitutes the first step in mediating the adaptive resistance to therapeutic agents via epigenetic remodeling [189].

Furthermore, *SOX10* downregulation was reported to collapse the proliferative, melanocytic GRN and replace it with one characterized by stress response [190]. *SOX10* expression in melanoma cells is also directly correlated with the proliferative capacity of melanoma cells. The reduction in its expression has been associated with a hypo-proliferative phenotype in tumor cells. More recently, downregulation of Sox10 was associated with a slow-cycling/dormant phenotype in melanoma that fuels tumor regrowth and invasiveness [191]. Taken together, the loss of *SOX10* contributes route(s) of phenotypic plasticity in melanoma, through which tumor cells develop adaptive therapeutic resistance.

1.5.5.2 ***SOX10*** **in GB**

In GB, *SOX10* displays heterogeneous levels of expression but is most highly expressed in the RTK1 subtype of GB. This is consistent with the resemblance of this subtype to the OPC-like cellular state of GB proposed by Neftel et al. and its normal function as an oligodendroglial lineage TF [168]. On the other hand, RTK2 and MES GB, which resemble NSCs/astrocytes or stromal cells, respectively, have low expression of *SOX10*. Our previous integrative transcriptomic and epigenomic study [33] charted the TF networks operative within individual GB subtypes, and we demonstrated that *SOX10* expression is a master regulator of the core regulatory circuitry in RTK1 GB. Specifically, *SOX10* exerts its function via its interaction with *BRD4* to maintain an enhancer landscape conducive to the RTK1 expression program. We also showed that RTK1 cellular state and bifurcate into RTK2 and MES states, accompanied by a decrease in *SOX10* expression along these two branches, suggesting that the reduced expression of *SOX10* is likely associated with transitions from the RTK1 cellular state. Indeed, we showed that the reduction of *SOX10* expression in conventional, differentiated-like GB cell lines re-configured the enhancer landscape, consequently activating master MES-GB TFs such as *FOSL2* [109, 192] and drives MES-transition. In parallel, we and others also noticed that *SOX10* expression strongly anti-correlates with that of *SOX9* and *EGFR*, the master regulators of the RTK2 GB subtype and markers for NSC-derived, more aggressive GBs [133, 193]. Similar to melanoma, therapy-associated downregulation of *SOX10* expression has been observed in GB [194]. Taken together, our findings and others underscore the potential roles of *SOX10* in mediating cell state and phenotypic adaptation in GB tumor cells, particularly under treatment pressure.

1.6 Aims of this thesis

The unmet clinical needs in GB necessitate a deeper understanding of the plasticity of BTSC, entailing a granular inspection of their architecture and dynamics in physiologically relevant models. Prior work from our group has shown that *SOX10* is an essential regulator of a molecular subtype of GB and its reduced expression endowed aggressive phenotypes commonly observed in more progressed GB. Given the pivotal roles of *SOX10* as a lineage TF and its established roles in mediating phenotypic plasticity and adaptive resistance in melanoma, I hypothesized that *SOX10* mediates phenotypic plasticity in BTSCs and enables *SOX10*-low BTSCs to escape therapy and drive tumor progression.

Following this hypothesis, I undertook this project with the specific aims below:

1. To characterize the phenotypic changes mediated by *SOX10* downregulation *in vivo*
2. To delineate the tumor cell sub-populations of *SOX10*-low tumors
3. To provide mechanistic insight into BTSC plasticity mediated by *SOX10* downregulation
4. To explore potential therapeutic interventions

2 Materials and Methods

2.1 Materials

2.1.1 Cell lines

Table 2: List of cell lines used in this work.

Cell Line	Source
A375	ATCC
HEK293	Provided by Cellular Tools / Vector & Clone Repository
LN229	ATCC
MGB1	Provided by Prof.Dr.Peter Angel, Division of Signal Transduction and Growth Control , DKFZ
NCH421k	Provided by Prof. Dr. Christel Herold-Mende, Universitätsklinik Heidelberg
NCH441	Provided by Prof. Dr. Christel Herold-Mende, Universitätsklinik Heidelberg
NCH644	Provided by Prof. Dr. Christel Herold-Mende, Universitätsklinik Heidelberg

2.1.2 Cell culture reagents

Table 3: List of cell culture reagents used in this work.

Reagent	Supplier	Identifier
2-Mercaptoethanol	Life Technologies	Cat#31350010
Accutase	Sigma Aldrich	Cat#A6964
B-27 Supplement, minus vitamin A (100X)	Life Technologies	Cat#12587010
B-27 Supplement, with vitamin A	Life Technologies	Cat#17504044
DMEM/F12 MEdium with HEPES	Thermo Fisher Scientific	Cat#11330032
DMEM/F12 Medium, no glutamine	Thermo Fisher Scientific	Cat#21331020
DMSO, Cell culture grade	Genaxxon Bioscience	Cat#M6323
Dulbecco's Modified Eagle's Medium - High Glucose	Sigma Aldrich	Cat#D5796
Dulbecco's Modified Eagle's Medium - Low Glucose	Sigma Aldrich	Cat#D5921
Dulbeccos's Phosphate Buffer Solution (DPBS)	Sigma Aldrich	Cat#8537
EGF Recombinant Protein	Thermo Fisher Scientific	Cat#PHG0311L

Reagent	Supplier	Identifier
Fetal Calf serum (FCS)	Merck Millipore	Cat#F2442
GlutaMAX supplement	Life Technologies	Cat#35050038
Hanks' Balanced Salt Solution, HBSS+	Sigma-Aldrich	Cat#55037C
Insulin solution human	Sigma Alrich	Cat#I9278
Iscove's Modified Dulbecco's Medium	Thermo Fisher Scientific	Cat#21980032
Laminin (from mouse Engelbreth-Holm-Swarm sarcoma)	Sigma Aldrich	Cat#L2020
L-Glutamine	Thermo Fisher Scientific	Cat#25030081
MEM Non-Essential Amino Acids Solution (100X)	Life Technologies	Cat#11140068
N2 (50X)	Life Technologies	Cat#17502048
Neurobasal medium	Thermo Fisher Scientific	Cat#21103049
Opti-MEM I Reduced Serum Medium	Thermo Fisher Scientific	Cat#31985054
Penicillin/Streptomycin (10000 U/ml, 100 µg/ml)	Thermo Fisher Scientific	Cat#15140122
Polybrene	Merck Millipore	Cat#TR1003-G
Polyethylenimine (PEI)	Polysciences Europe	Cat#17938
Poly-L-Lysine Hydrobromide	Sigma Aldrich	Cat#P2636
rhFGF	Biomol	Cat#50361
Trypsin EDTA solution (0.5 %)	Sigma Aldrich	Cat#T3924

2.1.3 Chemicals and Reagents

Table 4: List of chemicals and reagents used in this work.

Chemical	Supplier	Identifier
16% Formaldehyde (w/v), methanol free	Life Technologies	Cat#28906
AgeI-HF	New England Biolabs	Cat#R3552
Albumin Fraction V, protease-free, Europe	Carl Roth	Cat#T844
BlpI	New England Biolabs	Cat#R0585
BstXI	New England Biolabs	Cat#R0113
cOmplete Mini, EDTA free	Sigma-Aldrich	Cat#11836170001
D-Luciferin, potassium salt	BioVision	Cat#7903

Chemical	Supplier	Identifier
DNaseI solution (1000 U/ml)	Stemcell Technologies	Catalog # 07900
Donkey serum	Sigma Aldrich	Cat#D9663
EcoRI-HF	New England Biolabs	Cat#R3101
Ethanol	Merck Millipore	Cat#1085430250
Fxcycle Violet Ready Flow Reagent	Life Technology	Cat#37166
Glycine	Sigma-Aldrich	Cat#G8790
Goat serum	Life Technologies	Cat#16210064
Isopropanol	VWR International	Cat#423835000
Methanol	VWR International	Cat#364391000
Nuclease Free Water	Life Technologies	Cat#AM9937
NuPAGE 4-12 % bis-Tris 1.5 mm x 15-well	Life Technologies	Cat#NP0335BOX
NuPAGE 4X LDS sample buffer	Life Technologies	Cat#NP0007
NuPAGE MES SDS Running Buffer 20X	Life Technologies	Cat#NP0002
NuPAGE MOPS SDS Running Buffer 20X	Life Technologies	Cat#NP0001
NuPAGE Sample Reducing Agent (10X)	Life Technologies	Cat#NP0004
OneTaq Hot Start 2x Master Mix With Standard Buffer	New England Biolabs	Cat#M0484S
Papain	Stemcell Technologies	Cat#07465
Pierce ECL Plus Western Blotting Substrate	Thermo Fisher Scientific	Cat#32132
Pierce ECL Western Blotting Substrate	Thermo Fisher Scientific	Cat#32106
PrimaQUANT SYBR 2X SYBRGreen Mastermix	Steinbrenner Laborsysteme	Cat#SL-9902B
ProLong Glass Antifade Mountant with NucBlue Stain	Life Technologies	Cat#P36985
RIPA Lysis Buffer	Sigma-Aldrich	Cat#R0278
Spectra Multicolor Broad Range Protein Ladder	Thermo Fisher Scientific	Cat#26634
Spectra Multicolor High Range Protein Ladder	Thermo Fisher Scientific	Cat#26625
Stable Competent E. coli (High Efficiency)	New England Biolabs	Cat#C3040H
T4 Polynucleotide Kinase (PNK)	New England Biolabs	Cat#M0201S
Triton X-100	Sigma Aldrich	

Chemical	Supplier	Identifier
TrueBlack® Lipofuscin Autofluorescence Quencher	Biotium	Cat#23007
Whole milk powder	Carl Roth	Cat#T145
Xylol	Carl Roth	Cat#9713

2.1.4 Antibiotics and Inhibitors

Table 5: List of antibiotics, pharmaceutical drugs and inhibitors used in this work.

Chemical	Supplier	Identiifer
Fimepinostat	Med express	Cat#HY-13522
LY411575	Selleckchem	Cat#S2714
Puromycin	Merck Millipore	Cat#540411
Temozolomide	Sigma-Aldrich	Cat#T2577

2.1.5 Buffers and Solutions

Table 6: List of buffers and solutions used in this work.

Buffer	Composition
1X Transfer buffer	25 mM Tris, 200 mM glycine, 20 % methanol, pH 8.8
1X Tris-buffered saline (TBS)	150 mM NaCl, 10 mM Tris, pH 7.5
Antigen Retreival Buffer (pH 6.0)	10mM Sodium Citrate (Molecular weight = 294.1), 0.05% Tween 20, pH 6.0
Antigen Retreival Buffer (pH 8.0)	1mM EDTA, 0.05% Tween 20, pH 8.0)
Blocking buffer (IF)	5% normal goat/donkey serum in 0.5% Triton-X
Blocking buffer (WB)	5 % milk/BSA in TBS - 0.1 % Tween-20
LB (Luria Bertani) medium	0.5 % (w/v) NaCl, 1 % (w/v) Tryptone, 0.5 % (w/v) yeast extract
LB Agar	0.5 % (w/v) NaCl, 1 % (w/v) Tryptone, 0.5 % (w/v) yeast extract, 1.6 % (w/v) Agarose
Organoid dissociation buffer	125 U/ml papain, 12.5 U/ml DNase I in HBSS (with Ca^{2+}, Mg^{2+})
Papain activation buffer	1.1mM EDTA, 0.067mM mercaptoethanol, 5.5mM cysteine-HCl in 99.5 ml ddH_2O
Stripping Buffer (WB)	2% SDS 10%, 0.8% β-mercaptoethanol, 100 mM Tris HCl, pH6.8
TBS-T	TBS 1X, 1:1000 (v/v) Tween-20

2.1.6 Antibodies

Table 7: List of primary antibodies used in this work.

Antibody	Dilution	Supplier, Catalog Number
Alexa Fluor 647 anti-mouse H-2Kb (RRID: AB_492918)	1:50 (FC)	BioLegend Cat# 116511
Anti-CD3 (RRID:AB_2335677)	1:200 (IF)	Dako, Cat#A0452
Anti-Cleaved Notch1 (Val1744) (D3B8) Rabbit mAB (RRID:AB_2153348)	1:1000 (WB)	Cell Signaling Technology, Cat#4147
Anti-Cyclin D1, mouse mAB (RRID: AB_396432)	1:1000 (WB)	BD Biosciences, Cat#556470
Anti-GFP antibody, chicken pAB (RRID: AB_300798)	1:500 (IF)	Abcam, Cat#ab13970
Anti-Iba1, rabbit antibody (RRID: AB_839504)	1:500 (IF)	FUJIFILM Wako Shibayagi, Cat# 019-19741
Anti-Ki67, rabbit pAB (RRID:AB_443209)	1:200 (FC)	Abcam Cat# ab15580
Anti-p27Kip1, mouse mAB (RRID:AB_395225)	1:1000 (WB) 1:300 (IF)	BD Biosciences Cat#554069
Anti-*SOX10* antibody [EPR4007] (RRID: 2650603)	1:1000 (IF) 1:2000 (WB) 1:500 (FC)	Abcam, Cat#155279
Anti-*SOX2*, rabbit pAB (RRID :AB_2286686)	1 :1000 (WB)	Millipore. Cat# AB5603
Anti-Sox9 (D8G8H), rabbit mAB (RRID:AB_2665492)	1:1000 (WB) 1:500 (IF)	Cell Signaling Technology, Cat#82630
Anti-α-Tubulin, mouse mAB (RRID:AB_477593)	1:10000 (WB)	Sigma Aldrich Cat#T9026
APC Anti-Mouse H-2Db (RRID:AB_2728132)	1:50 (FC)	BioLegend, Cat# 111519

Table 8: List of secondary antibodies used in this work.

Target	Dilution	Supplier, Catalog number
anti-mouse IgG Alexa Fluor 647	1:1000	Invitrogen, A-21245
anti-mouse IgG Alexa Fluor Plus 488	1:1000	Invitrogen, A-32723
anti-mouse IgG HRP-linked	1:5000	Cell Signaling Technology,7076S
anti-rabbit IgG Alexa Fluor 488	1:1000	Invitrogen, A-11034
Anti-rabbit IgG HRP-linked	1:5000	Cell signaling Technology,7074S
Donkey Anti-rabbit IgG (H+L), CF647	1:1000	Sigma ,SAB4600177
Goat anti Rabbit IgG (H+L), Alexa Fluor 555	1:1000	Invitrogen, A-21428
Goat anti-Chicken IgY (H+L) Secondary Antibody, Alexa Fluor 488	1:1000	Invitrogen, A-11039

2.1.7 Plasmids

Table 9: List of commercial plasmids used in this work.

Plasmid	Cat. No, Supplier
MISSION pLKO.1 puro non-mammalian shRNA control	SHC002, Sigma Aldrich, Munich, Germany
pLenti CMV GFP puro	658-5, Addgene, Cambridge, USA
pLenti PGK V5-LUC Neo	W623-2, Addgene, Cambridge, USA
pLKO.1 puro	#10878, Addgene, Cambridge, USA
pLKO.1 puro CMV TurboGFP	SHC003, Sigma Aldrich, Munich, Germany
pMD2.G	#12259, Addgene, Cambridge, USA
pRL-TK	Promega, Madison, WI, USA
psPAX2	#12260, Addgene, Cambridge, USA

Table 10: List of generated plasmids used in this work.

Plasmid	Use
pLKO.1 shSox10-#1 and #2	shRNA-mediated mouse Sox10 knockdown
pU6-sgSox10-#1/#2 and#3	sgRNA-mediated human *SOX10* knockdown in CRISPRi systems

2.1.8 Oligonucleotide sequences

Table 11: List of shRNA sequences used in this work.

Target	Sequence	Targeting site
Mouse_Sox10_sh1	CCACGAGGTAATGTCCAACAT	Coding region (TRCN0000018985)
Mouse_Sox10_sh2	TTGCTCCAGCGATACCTTAAT	3'UTR (TRCN0000244290)
shNT	CAACAAGATGAAGAGCACCAA	NA

Table 12: List of sgRNA sequences used in this work.

Target	Sequence
Human_*SOX10*_sg1	ATTCAGGCTCCGTCCTAACG
Human_*SOX10*_sg2	CGAGCTGGACCGCACACCTT
Human_*SOX10*_sg3	AGTCTCGGGCTGTCCGGCCA
Negative control	GCGCCAAACGTGCCCTGACGG

Table 13: List of qPCR primers used in this work.

Target	Forward Sequence	Reverse Sequence
Human-*SOX10*	CTTTCTTGTGCTGCATACGG	AGCTCAGCAAGACGCTGG
Human-*SOX9*	AGCGAACGCACATCAAGAC	CTGTAGGCGATCTGTTGGGG
Human-LRIG1	GTGTCATCACCAACCACTTTGGC	GCAATCTGAGGGTTTGGGTGAC
Human-NRARP	CAAGGGCAACACGCAGGAGCT	CCGAACTTGACCAGCAGCTTCA
Human-HES5	TCCTGGAGATGGCTGTCAGCTA	CGTGGAGCGTCAGGAACTGCA
Human-TBP	GAACCACGGCACTGATTTTC	CCCCACCATGTTCTGAATCT
Human-*MGMT*	CCTGGCTGAATGCCTATTTCCAC	GCAGCTTCCATAACACCTGTCTG
Mouse-Sox10	GTGCCAGCAAGAGCAAGCCG	CTGCCTTCCCGTTCTTCCGCC
Mouse-Sox9	CACACGTCAAGCGACCCATGAA	TCTTCTCGCTCTCGTTCAGCAG
Mouse-Lrig1	TTCAGCCAACGCTACCCTCACA	TAAGCCAGGTGATGCGTGGTGT
Mouse-Nrarp	CAGACAGCACTACACCAGTCAG	CCGAAAGCGGCGATGTGTAGC
Mouse-Hes5	CCGTCAGCTACCTGAAACACAG	GGTCAGGAACTGTACCGCCTC
Mouse-Tbp	ACCGTGAATCTTGGCTGTAAAC	GCAGCAAATCGCTTGGGATTA

2.1.9 Kits

Table 14: List of commercial kits used in this work.

Kit	Supplier
CellTiterGlo® Viability Assay	Promega, Madison, WI, USA
Click-iT EdU Alexa Fluor 647 Flow Cytometry Assay Kit	Life Technologies GmbH, Carlsbad, CA, USA
FITC Annexin V Apoptosis Detection Kit with 7-AAD	BioLegend, San Diego, CA, USA
Pierce BCA Protein Assay	Thermo Fisher Scientific, Waltham, MA, USA
QIAGEN Plasmid Maxi Kit	Qiagen, Hilden, Germany
QIAGEN Plasmid Mini Kit	Qiagen, Hilden, Germany
QIAquick Gel Extractions Kit	Qiagen, Hilden, Germany
QIAquick PCR Purification Kit	Qiagen, Hilden, Germany
QuantiTect Reverse Transcription Kit	Qiagen, Hilden, Germany
Quick Ligation Kit	New England Biolabs, Ipswich, MA, USA
RNase-Free DNase Set	Qiagen, Hilden, Germany
RNeasy Mini kit	Qiagen, Hilden, Germany

2.1.10 Single cell RNA seq

Table 15: List of reagents and kits used for scRNA-seq

Kit	Supplier
Chromium Next GEM Single Cell 3′ GEM, Library & Gel Bead Kit v3.1	10X PN: 1000128
Chromium Next GEM Chip G Single Cell Kit (1000127), 1 kit	10X PN: 1000127
Chromium i7 Multiplex Kit	10X PN: 120262

2.1.11 Consumables

Table 16: List of consumables used in this work.

Consumable	Supplier
0.45 µm Millex 4mm Durapore PVDF filters	Merck Millipore, Darmstadt, Germany
12 Well Chamber, removable	Ibdis, Germany
96-well plate black	Greiner Bio-One GmbH, Kremsmünster, Austria
96-well plate white	Greiner Bio-One GmbH, Kremsmünster, Austria
Cell culture flasks and multi-well plates	Sarstedt GmbH, Nürnbrecht, Germany

Consumable	Supplier
Cell culture flasks and multi-well plates for adherent cells	BD Biosciences, Heidelberg, Germany
CometSlides	R&D Systems, Minneapolis, MN, USA
Einweg-Zählkammer C-Chip	Biochrom, Berlin, Germany
Eppendorf® Safe-Lock microcentrifuge tubes (1.5 mL, 2.0 mL)	Eppendorf, Hamburg, Germany
FACS tubes	Becton, Dickinson and Company (BD), Franklin Lakes, NJ, USA
Falcon® tubes (50 and 15 mL)	BD Biosciences, Heidelberg, Germany
Nunc® Cryo tubes	Sigma Aldrich, Munich, Germany
Pipette tips (10 µl, 20 µl, 100 µl, 200 µl, 1000 µl)	VWR International GmbH, Darmstadt, Germany
Polyvinylidene fluoride (PVDF) transfer membrane	Merck Millipore, Darmstadt, Germany
Superfrost PLUS slides	Thermo Fisher Scientific, Waltham, MA, USA
Ultracentrifuge tubes 14.0 ml PA thin-walled	Herolab, Heidelberg, Germany

2.1.12 Equipment and Devices

Table 17: List of equipment and devices used in this work.

Instrument	Supplier
Agilent 2100 BioAnalyzer	Agilent Technologies Inc., Santa Clara, CA, USA
Azure c200 Gel Imaging System	Azure Biosystems, Dublin, CA, USA
BD FACS Aria Fusion-3	BD Biosciences, Heidelberg, Germany
BD FACS Canto TM II	BD Biosciences, Heidelberg, Germany
BD FACS LSR Fortessa	BD Biosciences, Heidelberg, Germany
Beckman Ultracentrifuge with SW41 rotor	Beckman Coulter GmbH, Krefeld, Germany
Centrifuge Heraeus Sepatech Varifuge 3.0R	M&S Laborgeräte GmbH, Wiesloch, Germany
Chromium Next GEM Secondary Holder	10X genomics
Eppendorf Thermomixer comfort	Eppendorf, Hamburg, Germany
Forma Steri-Cycle CO2 incubator	Thermo Fisher Scientific, Waltham, MA, USA
Heracell 150i incubator	Thermo Fisher Scientific, Waltham, MA, USA
Heraeus Fresco 17 Centrifuge	Thermo Fisher Scientific, Waltham, MA, USA
Heraeus Varifuge 3.0 Centrifuge	Thermo Fisher Scientific, Waltham, MA, USA
IVIS Lumina LT Series III	Perkin Elmer, Waltham, MA, USA
Leica TCS SP8 confocal microscope	Leica Microsystems, Wetzlar, Germany
MasterCycler EP Gradient S	Eppendorf, Hamburg, Germany

Instrument	Supplier
Mini-PROTEAN 3 Cell	BioRad, Hercules, CA, USA
Mithras LB 940 plate reader	Berthold Technologies, Bad Wildbad, Germany
NanoDrop ND-2000c spectrometer	NanoDrop, Wilmington, NC, USA
NovaSeq 6000	Illumina Inc., San Diego, CA, USA
PIPETBOY acu 2	Integra Biosciences, Biebertal, Germany
Pipettes (2 µl, 20 µl, 100 µl, 200 µl, 1000 µl)	STARLAB International GmbH, Hamburg, Germany
Quantstudio5	Thermo Fisher Scientific, Waltham, MA, USA
Qubit 2.0 Fluorometer	Invitrogen, Karlsruhe, Germany
Sky Line Orbital Shaker	ELMI North America, Newbury Park, CA, USA
Steri-Cycle CO2 Cell Culture Incubator	Thermo Fisher Scientific, Waltham, MA, USA
TC20 Automated Cell Counter	Biorad, Feldkirchen, Germany
Tube Roller	STARLAB International GmbH, Hamburg, Germany
Vi-CELL XR 2.03	Beckman Coulter GmbH, Krefeld, Germany
Voyager 300 8-channel pipette	Integra Biosciences, Biebertal, Germany
Water Bath GFL Type 1002	GFL Gesellschaft für Labortechnik mbH, Burgwedel, Germany
Water Bath Julabo SW-20C	Julabo, Seelbach, Germany
XCell SureLock Mini-Cell Electrophoresis System	Thermo Fisher Scientific, Waltham, MA, USA

2.1.13 Databases and Software

Table 18 :List of public datasets analyzed in this work.

Deposited dataset	Source
Brain tumor stem cell bulk RNA-seq	Marques et al, eLife, 2021 [109]
TCGA-GBM (HG-U133A)	TCGA
Brain tumor single cell RNA-seq	Neftel et al., Cell, 2022 [127]
Primary and recurrent single cell RNA-seq	Abdelfattah et al., Nat. Comm., 2022 [195]
GLASS cohort (2022 updates)	Varn et al, Cell, 2022 [196]

Table 19: List of software used in this work.

Software	Version	Supplier
Affinity Designer	1.8.3.641	Serif (Europe) Ltd., Nottingham, United Kingdom
BD FACS Diva	6.1.3	BD Biosciences, San Jose, USA
BioRender	2021	Free trial (https://biorender.com)

Software	Version	Supplier
EndNote	x9	Thomson ResearchSoft, Carlsbad, CA, USA
FlowJo	v.10.7.0	FlowJo, LLC., Ashland, USA
GraphPad Prism	9.0.0	GraphPad Software, San Diego, USA
ImageJ	1.51n	Open Source, National Institute of Health, Bethesda, USA
INTAS ChemoStar	v60+	INTAS Science Imaging Instruments GmbH, Göttingen, Germany
Living Image	4.7	PerkinElmer, Waltham, MA, USA
Microsoft Excel/PowerPoint/Word	2016	Microsoft, Redmond, USA
QuantStudio Design and Analysis Software	v1.5.1	Thermo Fisher Scientific, Waltham, MA, USA
R	4.0.2	Open Source, R Foundation
RStudio	1.2.1335	Open Source, R Foundation
SnapGene	5.1.5	GSL Biotech LLC, San Diego, USA
QuPath	0.2.3	An open-source software by Bankhead et al., 2017[197]

2.2 General methods

2.2.1 Cell lines and culture conditions

2.2.1.1 NCH human brain tumor stem cells

Human glioblastoma cell stem cells (GSCs) NCH421k, NCH441 and NCH644 were previously established, characterized and were kindly provided by Prof.Dr.Christel Herold-Mende [198]. Cells were cultured in DMEM/F12, HEPES containing 1X B-27 (without vitamin A), 2 mM L-glutamine , 20 ng/ml Epidermal growth factor, 20 ng/ml fibroblast growth factor 2 and 1% Pen/Strep. Cells were maintained as spheres in suspension culture wares. Upon reaching large sphere sizes (usually 1 week after seeding), spheres were first collected in centrifuge tubes and were dissociated with Accutase® at 37 °C with occasional agitation. Cells were then washed with plain DMEM/F12, HEPES medium and were centrifuged at 900 rpm, after which cells were re-seeded in appropriate vessels. All cell lines were kept in a 5 % CO_2 humidified incubator at 37 °C.

2.2.1.2 Mouse GB cells

Murine glioblastoma cell line mGB1 was previously established and kindly provided by P. Angel's laboratory [199]. Cells were cultured in DMEM/F12, HEPES containing 1X N-2 Supplement , 1X B27 (without vitamin A), 1X L-Glutamine , 20 ng/ml Epidermal growth factor, 20 ng/ml fibroblast growth factor 2 and 1% Pen/Strep. Cells were maintained as spheres in suspension culture wares. Upon reaching large sphere sizes (around 3-4 days after seeding), spheres were first collected in centrifuge tubes and were dissociated with Accutase® at 37 °C with occasional agitation to aid dissociation. Cells were then washed with plain DMEM/F12, HEPES medium and were centrifuged at 900 rpm, after which cells were re-seeded in appropriate vessels. All cell lines were kept in a 5 % CO_2 humidified incubator at 37 °C.

2.2.1.3 Other human cell lines

Human glioblastoma LN229 and human melanoma A375 cell lines were cultured in DMEM-low glucose medium supplemented with 10 % FBS and 1% Pen/Strep. HEK-293T were cultured in I*MDM* supplemented with 10% FBS, 2 mM -L-glutamine and 1% P/S. Since these cells are adherent, cell were cultured until they were 90% confluent and were dissociated with 0.5% trypsin. They were then re-seeded to appropriate culture vessels for adherent cells. All cell lines were kept in a 5 % CO_2 humidified incubator at 37 °C.

2.2.2 Lentivirus production

Lentiviral particles were produced using the second generation of lentiviral packaging plasmids. Briefly, early passage (passage number < 5) packaging cell line HEK293T were seeded at 4 x10^6 cells per 10 cm culture dishes. Next day, 4 µg of each second generation lentiviral packaging plasmids, psPAX.2

and pMD2.G and 8 µg of the lentiviral plasmids, were co-transfected into the HEK293T cells using 1 mg/ml polyethylenimine (PEI). The transfection mixes were then incubated at RT for 20 min, after which they were added to the cells dropwise and returned to the incubator for 24 h. The next day, medium was replaced with 6 ml of fresh, completed IMDM. After 48 h of incubation, the viral supernatants were collected, passed through 45 µm syringe filters into SW41 centrifuge tubes, and spun down using an SW41 rotor for 1.5 h at 25,000 rpm at 4 °C. The viral supernatants were carefully removed and the viral pellets were resuspended in 100 µl OptiMEM and left at 4°C for 4 h to fully dislodge the viral pellets. The lentiviruses were then aliquoted and stored at - 80 °C until further use. For each batch of lentivirus production, pLKO.1-TurboGFP lentiviruses were produced in parallel and they were transduced to HEK293T cells for evaluation the viral titer. Briefly, HEK293T cells were seeded at 100,000 cells per well on a 6-well plate one day prior to transduction with serially diluted pLKO.1-TurboGFP lentiviruses in 1 ml medium supplemented with 1 µg/ml polybrene. The medium was changed the next day and GFP-positivity was assessed with flow cytometry 72 h post-transduction.

2.2.3 Knockdown of *SOX10* in mouse and human cells

In mGB1 cells, Sox10 was stably knocked-down using short hairpin RNA (shRNA). The target sequences of shRNA sequences used in this thesis were chosen from the BROAD RNAi Consortium database (sh1: TRCN0000018985, sh2: TRCN0000244290, see **Table 11** for full oligo sequences). These sequences targeted non-overlapping regions of mouse Sox10 transcript and were used in our previous study. For cloning of shRNA plasmids, forward and reverse shRNA oligos with AgeI and EcoRI overhangs were first phosphorylated by T4 polynucleotide kinase for 30 min at 37 °C. Afterwards, they were annealed by first heating to 95°C for 5 min and were then cooled down to RT. The annealed oligos were diluted by 200 times in water and were ligated to AgeI and EcoRI restricted pLKO.1-puro plasmid using Quick Ligase Kit. In each ligation mixture, 1 µl of the diluted oligos were mixed with 50 ng of the restricted plasmids and were left at RT for at least 15 min. The ligation mixture was transformed into competent NEB® Stable Competent E. coli (High Efficiency) by heatshocking at 42°C for 30 seconds, after which outgrowth medium was supplied to the cells and incubated at 37°C for 1 h with shaking. Bacteria were grown on ampicillin selection LB agar plates overnight at 37 °C. Single colonies were picked and Sanger-sequenced to check the presence of shRNA sequence insertion using with hU6 promoter primer (5'-GACTATCATATGCTTACCGT-3'). For the delivery of shRNAs, lentiviruses were produced and transduced into mGB1 cells. Transduced cells were selected with 1 µg/ml puromycin for 48 h and the KD efficiency was checked by both qPCR and Western blot.

In human GSCs, *SOX10* was stably knocked-down using CRISPR-interference method (CRISPRi). In this method, cells were first transduced with a catalytically inactive Cas9 fused to a Krüppel-associated box transcriptional repression domain (dCas9-KRAB). Single clones stably expressing dCas9-KRAB were expanded and transduced with single guide RNA (sgRNA) plasmids previously used in our group (**Table 12)**. To knockdown *SOX10* expression, NCH441 and NCH644 cells were first transduced with dCas9-KRAB-BFP lentiviruses. Three days after the transduction, single cells expressing dCas9-KRAB were sorted by their BFP-positivity using flow cytometry and were seeded onto round-bottom 96-well plates. These clones were allowed to be expanded and the clones were checked for their expression of dCas9 by Western blotting. Clones with high expression levels of dCas9 were chosen and further expanded. Subsequently, these GSC lines stably expressing dCas9-KRAB were transduced with sgRNA plasmids. Transduced cells were selected with 1 µg/ml puromycin for 48 h and the KD efficiency was checked by both qPCR and Western blot.

2.2.4 Reverse transcription quantitative PCR (RT-qPCR)

Cell pellets were first collected and total RNA was extracted with the RNAeasy Mini Kit as per manufacturer's instructions. RNA concentrations were quantified with Nanodrop 2000 spectrophotometer. RNA was reverse-transcribed into complementary DNA (cDNA) using Quantitect Reverse Transcription Kit, following the manufacturer's instructions. Potential genomic DNA co-purified with RNA extraction was eliminated with gDNA wipeout buffer provided with this kit. For mRNA quantification, SYBR-green based qPCR was performed. In each reaction, 25 ng cDNA was mixed with 0.2 µM of forward and reverse primers and 1X primaQuant SYBR Green reagent in a total reaction volume of 10 µl, with the following thermocycling parameters: 50 °C for 2 min, 95 °C for 15 min followed by 40 cycles of 95 °C for 15 sec and 60°C for 1 min. Fluorescence emission was detected by t The reactions were performed on a Quantstudio 5 Real-Time PCR system. Gene expression was normalized with housekeeping genes TBP or DCTN2. The relative expression level was determined by $2^{-\Delta\Delta Ct}$ method. Primers used in qPCR are listed in **Table 13**.

2.2.5 Western blot analysis

Cells were washed with ice-cold PBS and were lysed in 100 – 300 µl RIPA lysis buffer supplemented with 1X cOmplete™, Mini EDTA-free Protease Inhibitor Cocktail and 1X phosphatase inhibitor phosSTOP. Lysates were kept on ice for 30 min with intermittent vortexing to homogenenize the samples. Lysates were then centrifuged at 13,000 rpm at 4°C for 10 min. Afterwards, supernatants were collected and protein concentration was determined by a standard curve plotted against the concentration gradient of bovine serum albumin standards in BCA assays. The protein lysates were normalized to 0.5 µg/ µl with NuPAGE™ LDS Sample Buffer and reducing agent and boiled at 95°C for 5 min. A total of 5 µg of protein samples were loaded and resolved on 4-12% of NuPAGE™ Bis-Tris Protein gels using MOPS-SDS running buffer or MES-SDS running buffer for resolution of smaller protein sizes (less than 40 KDa). Afterwards, gels were equilibrated in transfer buffer for 5 min to remove the salts and detergents in electrophoresis buffer. The proteins were then transferred onto transfer buffer pre-wetted PVDF membrane using Biorad tank transfer system at 100 V for 1.5 h. The membranes were blocked in 5% skimmed milk or 5% bovine serum albumin in TBS-T at room temperature for 1 h with gentle shaking. The membranes were incubated with primary antibodies of the target proteins diluted in appropriate concentrations of either 5% skim milk or 5% BSA at 4°C overnight with gentle shaking. The next day, the membranes were washed three times with TBS-T for a total of

30 min. Corresponding horseradish peroxidase (HRP) conjugated secondary antibodies were added and incubated for 1 h with gentle agitation at room temperature. The membranes were washed again with TBST for three times for a total of 30 minutes before the addition of ECL reagents or ECL plus reagents. The signals were subsequently detected by light-sensitive films. Alpha-tubulin served as the loading control.

2.2.6 Immunofluorescence analysis

One day prior to cell seeding, sterile coverslip (6 mm in diameter) or 12-well immunofluorescence chamber were coated with laminin/poly-L-lysine coating buffer (5 µl laminin + 30 µl poly-L-lysine in 2 ml PBS) at 37°C overnight. The next day, the coating buffer was washed twice with DMEM/F12 medium. Human and mouse GSCs were dissociated by acctuase as described in method. The dissociated cells were seeded on coated coverslip or 12-well immunofluorescence chamber. Upon proper attachment of the cells, medium was removed from the wells and washed once with PBS. Cells were then fixed in 4% paraformaldehyde in PBS for 15 min at room temperature. Cells were then washed twice with PBS and permeabilized with ice-cold 0.5% Triton X-100 in PBS for 20 min. They were then blocked with 5% normal goat or donkey serum in 0.5% Triton X-100 in PBS for another hour. Primary antibodies were diluted at appropriate concentrations in 1% normal goat or donkey serum in 0.1% Triton X-100 in a humidified chamber at 4°C overnight. The next day, the coverslips were washed with PBS-T (0.1% Tween-20 in PBS) for three times for a total of 30 minutes. Fluorochrome conjugated secondary antibodies were diluted at 1:1000 – 1:2000 in PBS-T and were incubated in dark at room temperature for 1 h. Coverslips or slides were washed with PBS three times for 30 min. Upon last wash, slides or coverslips were rinsed with distilled water to remove residual salts. Coverslips were then mounted using Nucblue mounting medium. Fluorescence images were captured using an SP8 confocal microscope. Image analysis softwares ImageJ and QuPath were used to quantify the number of p27 positive and Sox9/p27 double positive cells in each image.

2.2.7 Flow cytometry analysis

2.2.7.1 G0/G1 cell cycle distribution analysis by Ki67 and DNA co-staining

To analyze the distribution of G0 and G1, cells were first spun down and singularized by accutase at 37 ° C. For each stain, around 0.5 million cells were used. Cells were fixed with 70% ethanol at 4 ° C overnight. The next day, cells were first rehydrated with FACS buffer (2% fetal bovine serum in PBS) and then centrifuged at 9,000 rpm for 10 min. Cells were washed again with FACS buffer and were then incubated with Ki-67 antibody at 1:200 dilution in FACS buffer 1 h at room temperature. After primary antibody incubation, cells were washed twice with FACS buffer and stained with AF647 conjugated secondary antibody, donkey against rabbit at 1:1000 dilution in FACS buffer in the dark for 30 min at room temperature. Cells were then washed twice with FACS buffer and stained with FxCycleTM Violet

Stain in the dark for 30 min at room temperature. Samples stained with secondary antibodies only and samples stained with FxCycleTM violet stain were used as secondary controls.

2.2.7.2 MHC-I protein staining

To analyze the expression of MHC-I molecules, cells were spun down and singularized by accutase at 37°C. For each stain, around 0.5 million cells were used. After accutase treatment, cells were washed with ice-cold FACS buffer (2% fetal bovine serum in PBS), transferred to ice and centrifuged at 1,500 rpm for 5 min at 4°C. Cells were then stained with viability dye and conjugated MHC-I antibodies as tabulated in **Table 7** for 30 min at 4°C. The cells were then washed twice and resuspended in FACS buffer. Unstained samples were used as a negative control.

2.2.7.3 *SOX10* intracellular staining in GLICO model

To analyze the expression of *SOX10* in tumor cells after TMZ treatment, tumor cells were harvested as described in. Cells were then washed once with PBS and stained with viability dye at 1:500 dilution in PBS for 30 min at 4 °C. Cells were then fixed with 4% PFA (methanol free) for 15 min at RT in the dark. Cells were washed with FACS buffer and incubated with permeabilization and blocking buffer (5% normal goat serum in 0.5% Triton-X 100) for 1 h at room temperature. After washing with FACS buffer, cells were incubated with rabbit anti-human/mouse SOX10 antibody at 1:500 dilution and chicken anti-GFP antibody at 1:500 dilution in permeabilization and blocking buffer for 1 h at room temperature. Cells were then washed with FACS buffer and stained with conjugated secondary antibodies (anti-rabbit AF647, 1:2000 and anti-chicken AF488, 1:2000) for 30 min at room temperature. Finally, cells were washed and resuspended in FACS buffer and proceeded to flow cytometry analysis. *SOX10* expression levels were measured as the median fluorescence intensity (AF647) of the viable, GFP-positive cells. Samples stained with only secondary antibodies were used as a negative control.

2.2.7.4 Click-iT EdU cell proliferation assays

Cells were seeded at 200,000 cells per well on a 6-well plate and 10 µM of 5-ethynyl-2'-deoxyuridine (EdU) was added to the medium immediately after cell seeding. Cells were then returned to the incubator for 3 h (mGB1 cells) or 6 h (NCH cells) before harvesting by accutase. Cells were washed with PBS once and fixed with 4% PFA for 15 min. They were washed once with FACS buffer and permeabilized with 0.1% Triton-X 100 in PBS for 30 min at room temperature. Subsequently, cells were washed once with FACS buffer and stained with the Click-iT EdU cell proliferation kit, Alexa Fluor 488 or 647 according to the manufacturer's instructions. Briefly, cells were incubated with a reaction buffer reagent consisting of 1X Click-iT reaction buffer, reaction additive, copper sulphate and Azide-647, for 30 min at room temperature. Subsequently, cells were washed with FACS buffer and proceeded to flow cytometry analysis. Samples stained with only AF488 or AF647 were used as a negative control.

2.2.7.5 Annexin V/Live Dead Apoptosis assays

Harvested cells were first washed with PBS and stained with live/dead Pacific blue at 1:1000 with PBS. Cells were incubated at 4°C for 30 min. Cells were then washed with Annexin binding buffer and PE-conjugated Annexin V was added at 1: 20 in annexin V binding buffer. Cells were incubated in the dark for 15 minutes at room temperature before proceeding to flow cytometry analysis.

2.2.7.6 Data acquisition and analysis

Cells were analyzed on the LSRFortessa (BD Biosciences). BD FACSDiva software version 9 and FlowJo version 10 was used for data analysis.

2.2.8 Cell viability assay

Cell viabilities upon TMZ treatment in NCH cells and upon LY411575 and Fimepinostat co-treatment were preformed using CellTiter-Glo® Luminescent Cell Viability assay, which measures the metabolically active cells. Cells were seeded in white 96-well plates at 10,000 cells/well and treated with DMSO or serially diluted inhibitors (TMZ: 25 µM to 400 µM; LY411575: 1.6 nM to 1000 nM) on the same day when cells were seeded. Cells were incubated for 72 h at 37 °C. CellTiter-Glo assay was performed as per manufacturers' instructions. Briefly, the cell culture plates were taken out from the incubator and were were equilibrated to RT for 30 min. To each well, 30 µl of the Cell Titer-Glo reaction substrate was added and the plates were left on a rocking platform to induce cell lysis for 2 min. The plates were then left at RT for 15 min before measuring the luminscence signals on a plate reader. Raw values from the luminscence signals were normalized to DMSO vehicle controls. Whenever IC50 values were calculated, it was done so using GraphPad Prism software.

2.2.9 Growth curves

NCH421k and NCH441 were seeded at 100,000 cells per well on 6-well plates. Cells were treated with DMSO or temozolomide at 100 µM, which corresponds to the maximum concentration of temozolomide. The media (with TMZ) was refreshed every 3-4 days and viable cells were counted using the TC20 automated cell counter (Biorad #1450102) every week. Tumor cells treated with DMSO reached confluence around 10 – 14 days after seeding and were counted for two weeks whereas cells treated with TMZ were counted for 5 weeks before temozolomide was withdrawn.

2.2.10 GLICO model

2.2.10.1 Cerebral organoid generation and maintenance

In collaboration with colleagues Pavle Boskovic and Jasmin Mangei, cerebral organoids (COR) were generated from induced pluripotent stem cells (iPSCs) using protocols developed by Lancaster et al. [200]. CORs at the age of 40 – 50 d were used in this study. CORs were maintained in a 24-well plate in 1 ml mature COR differentiation medium (1:1 mix of DMEM/F12 w/ HEPES and Neurobasal medium, 2.5 µg/ml hr-Insulin, 1X 2-Mercaptoethanol, 0.5X GlutaMAX, 0.5X MEM-NEAA, 1 % P/S, supplemented with 0.5X N2 and 0.5X B-27 + Vitamin A).

2.2.10.2 Cerebral organoid dissociation

For the analysis of tumor cells invaded into the organoids, cerebral organoids were dissociated using a papain/DNase I-based method. Papain was first activated in papain activation buffer for 30 min at 37 °C. Dissociation buffer was then prepared by adding 240 µl of activated papain and 200 U of DNase I in the final 2 ml of HBSS (with magnesium and calcium). To dissociate cerebral organoids (diameter smaller than 5 mm), spent medium were carefully removed from the organoids and washed once with PBS. Organoids were then transferred to 1.5 ml centrifuge tubes and 300 µl of dissociation buffer were added to each organoid. Tubes were then placed on an orbital shaker and incubated at 37°C for 10 min. Afterwards, organoids were gently resuspended with wide bore pipette tips before returning to 37°C for another 10 min incubation. These incubation-resuspension steps were repeated until no large clumps of tissues were visible. An equal volume of trypsin inhibitor was added to the reaction to quench digestion and cells were spun at 1000 rpm for 5 min.

2.2.10.3 GLICO model with NCH644-Ctrl and KD cells

NCH644 stably expressing dCas9-KRAB (NCH644-dCas9 cells) were transduced with pLenti-GFP-blast and were selected with 10 µg/ml blasticidin to ensure all the cells were GFP positive (NCH644-dCas9-GFP). They were then transduced with sgNC and sg*SOX10* viruses as described previously. A total of 10,000 GFP-tagged Ctrl and KD cells were co-cultured with each COR for 24 h without agitation. Next day, the CORs were washed with PBS to remove uninvaded cells and transferred to a new well and grown on an orbital shaker for 14 days at 37 °C, with medium change every 2-3 days. On day 14, fluorescence images were taken using a stereomicroscope. To measure tumor load in each COR, they were dissociated as described above. They were then stained with Live/Dead Pacific blue to label dead cells, and the percentage of viable GFP-pos tumor cells in each COR was determined by flow cytometry.

2.2.10.4 GLICO model with TMZ treatment

NCH644 cells were first transduced with pLenti-PGK-V5-GFP-LUC-Neo. To ensure a uniform expression of luciferase, GFP-positive cells were sorted by flow cytometry. These dual positive cells (NCH644-GFP-luc) were used in the TMZ treatment study. A total of 100,000 NCH644-GFP-luc cells were co-cultured with CORs as described above. Tumor growth was monitored by bioluminescence signals (BLI). Briefly, GLICOs were incubated with 150 µg/ml D-luciferin for 30 min at RT and the BLIs were acquired using IVIS® Lumina LT Series III (PerkinElmer) with an integration time of 1 min. Total proton flux was quantified using the Living Image® software. BLIs before DMSO or 100 µM of TMZ was added to the GLICOs were used as baseline and were measured every 3 days. When the BLI of the DMSO-treated GLIOCOs reached maximum (day 21), all the GLICOs were harvested and were dissociated and *SOX10* expression was determined as described above.

2.2.11 Clariom microarray expression profiling and analysis

mGB1 cells treated with DMSO or 2 µM of LY411575 were collected after 48 h of incubation. Total RNA was extracted as described in the previous section, with the addition of an on-column DNA digestion step to remove contaminating genomic DNA using the RNase-free DNase kit. RNA samples were sent to the microarray core facilities for further quality control steps, including RNA integrity number (RIN) determination by TapeStation4200. In brief, labeled cDNAs were generated from high quality RNA samples using GeneChip WT PLUS Reagent Kit (Affymetrix), which involves cDNA conversion and amplification from RNA, as well as their subsequent labelling and hybridization on the microarray chip. Gene expression was determined with mouse Clariom-S-assay. Upregulated genes (LY411575-treated vs DMSO control, fold change > =1.2) and downregulated genes (LY411575-treated vs DMSO control, fold change <=1.2) in mGB1-sh1 and sh2 cells were further analyzed using clusterProfiler package on R to determine the common upregulated and downregulated pathways in KD cells consequent to LY411575 treatment.

2.3 *In vivo* procedures

2.3.1 Animal housing

All animals used in this thesis were housed under strict specified pathogen-free (SPF) conditions as per recommendations of the FELASA, in animal facility in German Cancer Research Center. Briefly, animals were housed in with at facilities with temperature and humidity controlled at 22.0 ± 2.0°C and 55.0 ± 10.0%, respectively. Animals were given unrestricted access to food and water. The health conditions of the animals were monitored regularly.

2.3.2 Tumor injection

Animal experiments were performed in accordance to relevant ethical regulations and were approved by the Regierungspräsidium Karlsruhe, Germany (reference no. G-156-15). Murine glioblastoma cell line mGB1 was previously established and kindly provided by Angel's laboratory. Prior to intracranial injection, adult C57B6 /J mice (8 weeks female) were ordered from Janvier and were allowed to acclimatize in the animal housing facility. Intracranial injections were performed using 200,000 cells of Ctrl and KD cells (KD#2) in 1 µl volume. Eight-week-old female C57B6 /J mice were then injected with the cells under anesthesia with isoflurane.

2.3.3 Monitoring of tumor sizes by MRI

Tumor sizes were monitored by MRI scanning 1 month after injection and weekly starting at 8 weeks post-injection. Mice with large tumor sizes (above 50 ul as measured by T2 MRI) in both groups were sacrificed and included in this study (4 mice from KD, 3 mice from Ctrl).

2.3.4 Histological analysis

2.3.4.1 Tissue fixation, embedding and sectioning

For histological analysis, paraffin embedded tumor sections were prepared following standard protocols. Briefly, harvested brains were washed in PBS and were fixed with 4% PFA overnight at 4°C with gentle agitation. Next day, the brains were sliced coronally and then placed onto Spin Tissue Processor (STP120), to be dehydrated over an ascending concentrations of ethanol and to be embedded with immersion in Histo-Comp® Tissue embedding-medium (VO-5-1001). Afterwards, the cassettes were placed in the HistoStarTM Embedding Workstation, to be embedded in Histo-Comp® Tissue-embedding-medium (VO-5-1001). Finally, the paraffin blocks were allowed to set on a cool plate before storage. Paraffin blocks were then cut into 4 µm sections using a microtome. Sections were either stained with hematoxylin and eosin (H&E) or subjected to immunohistochemistry, as described below.

2.3.4.2 H&E staining

For H&E staining, slides were first deparaffinized and rehydrated using distilled water. They were then stained in hematoxylin for 1 min, washed with distilled water and then counter-stained in Eosin for 1 min. The stained slides were then dehydrated with a series of ascending concentrations of ethanol and cleared in xylene. Histological features were then examined by Dr. Andrey Korshunov from Department of Neuropathology, Heidelberg University. Brightfield images of the H&E slides were generated by Zeiss Axio Scanner using a 20X objective.

2.3.4.3 Immunohistochemistry

For immunohistochemistry, slides were deparaffinized and rehydrated with sequential immersion in xylene, a series of descending concentrations of ethanol (100%, 90% and 70% ethanol) and finally with distilled water. Next, slides were placed in a cuvette and subjected to heat-induced antigen retrieval. Briefly, slides were immersed in sodium citrate buffer (10 mM sodium citrate, 0.05% Tween-20, pH 6.0) and heated to 100°C for 20 min using a steam cooker. For CD3 staining, a Tris/EDTA-based buffer (10 mM Tris base, 1 mM EDTA, 0.05% Tween 20, pH 9.0) was used and steamed for 20 min. Slides were allowed to cool down to RT before washing with 0.3% Triton-X 100/PBS for 20 min. Afterwards, the slides were permeabilized and blocked with 5% normal serum in 0.3% Triton-X 100/PBS for 1 h. Primary antibodies were diluted at appropriate concentrations using 0.3% Triton-X/PBS supplemented with 1% normal serum. Slides were left in a humidified chamber at 4°C overnight. Next day, the slides were washed with PBS-T (0.1% Tween-20 in PBS) for three times for 30 min. Fluorochrome conjugated secondary antibodies were diluted at 1:1000 in PBS-T and were incubated in the dark at RT for 1 h. After secondary antibody incubation, slides were washed with PBS three times for 30 min. Upon the last wash, slides were treated with TrueBlack to reduce autofluorescence according to manufacturer's instructions. After further washing steps with PBS, slides were mounted using Nucblue mounting medium. Fluorescence images were captured with an SP8 confocal microscope.

2.4 Single cell RNA-sequencing

2.4.1.1 Tissue dissociation

Mice with large tumor sizes (above 50 ul as measured by T2 MRI) in both groups were sacrificed and included in this study (4 mice from KD, 3 mice from Ctrl). After euthanization with carbon dioxide, tumor areas were carefully resected to ensure minimal inclusion of normal brain tissue. Tumors were then finely minced and dissociated using Tumor Dissociation Kit, mouse (Miltenyi Biotech, 130-096-730). Minced tissues were first transferred to gentleMACS C tubes containing 2.5 ml of enzyme digestion mix (100 µl enzyme D, 50 µl enzyme R and 12.5 µl enzyme A, in 2.35 ml plain RPMI-1640 medium). The tubes were then loaded on a gentleMACS dissociator and dissociated using the program h_tumor_02. The C-tubes were then placed in a rotator and gently agitated at 37°C for 15 min, before further dissociation on the gentleMACS dissociator using the program h_tumor_03. The tubes were then placed in a rotator and gently agitated at 37°C for another 15 min. The C-tubes were then subjected to final dissociation using program m_brain_01. The final mixtures were triturated first with 5 ml serological pipettes and then with 1 ml pipette tips to ensure tissue homogenization. The digested tissues were washed with ice-cold HBSS, passed through 70 µm cell strainers and spun down at 350 x g for 10 min at 4°C. To remove myelin debris, cell pellets were resuspended in 10 ml 22% Percoll/HBSS and centrifuged at 950 x g for 30 min at 4°C without brake. Supernatants containing myelin fragments were removed as completely as possible. The pellets were then resuspended in 1% BSA/PBS. To fractionate tumor and stromal fractions, the resuspended cell pellets were sorted on BD FACSAria™ Fusion based on GFP-positivity (**Figure 6**). Cells from both fractions were spun down and resuspended in 1% BSA/PBS for single cell capture and library preparation in the singe cell Open Lab in DKFZ, Heidelberg.

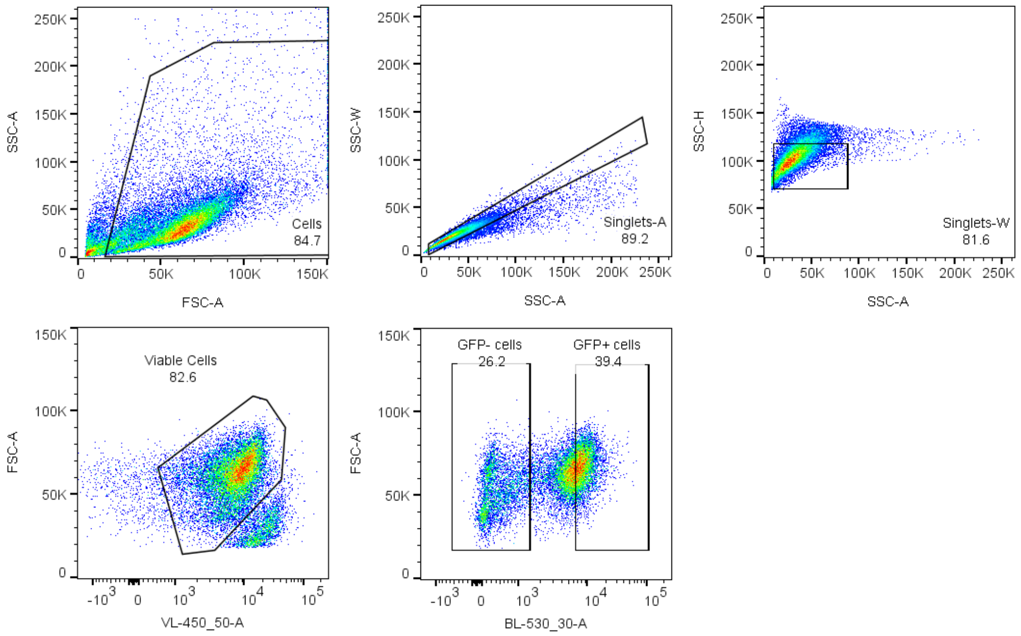

Figure 6. Gating strategies for GFP-pos and GFP-neg cells in scRNA-seq study

2.4.1.2 Single cell library preparation and sequencing

Single cell libraries were prepared using Chromium Next GEM Single Cell 3′ GEM, Library & Gel Bead Kit v3.1 (10X PN: 1000128), closely following the standard protocols recommended by 10X Genomics. Briefly, Single Cell 3’ v3.1 Gel beads (10X PN: 2000164), flow-sorted single cell suspensions (Recovery target = 10,000 cells per sample) and single cell master mix were loaded onto Chromium Next GEM Chip G (10X PN: 1000127) for gel beads-in-emulsion (GEM) formation on Chromium Controller. In each GEM, each cell was lysed and each transcript was tagged with a unique molecular identifier (UMI) associated with the gel beads. Following GEM formation, they were transferred to a thermocycler for reverse transcription (53°C for 45 min, 85 °C for 5 min and 4°C on hold). Afterwards, GEMs were broken with Recovery Agent (PN1000008) and cDNA cleanup was performed using Dynabeads MyOne Silane beads (PN:2000048) and amplified for 12 cycles. Reactions were then cleaned up using SPRIselect Reagent from Beckman Coulter (B23317) and the resultant cDNAs were subjected to quality control and quantification in Agilent TapeStation 4200. Final indexed libraries were then constructed with the following steps: 1. cDNA fragmentation and size selection to optimize the cDNA amplicon size. 2. End repair, A-tailing and adaptor ligation PCR to incorporate P5, P7 primers and TruSeq reads for Ilumina amplification, as well as i7 and i5 indexes (PN-120262) to identify individual samples. Finally, library quality was assessed using the Agilent High Sensitivity DNA kit and libraries were quantified using the Qubit dsDNA HS Assay kit . Equal amounts of the libraries were pooled and sequenced on NovaSeq 6000 with Paired-end (28+94 bp) S2 setup at High Throughput Sequencing Unit of the Genomics and Proteomics Core Facility at the German Cancer Research Center in Heidelberg

2.5 Bioinformatics analysis

2.5.1 Public data analysis

Normalized BTSC and TCGA-GBM data were downloaded from their respectively sources as tabulated in **Table 18**. Top 10% and bottom 10% of the dataset were classified as *SOX10*-high and *SOX10*-low samples respectively. Differentially expression analyses were performed using limma package (contrast= SOX10-low/SOX10-high). Differentially regulated genes, defined as p.adj < 0.05, were sorted by their log2 fold change and gene set enrichment analyses (GSEA) were performed using the GSEA() function in ClusterProfiler package against curated genesets. For TCGA-GBM data, only IDH-wildtype primary tumor samples with available SOX10 expression information were included in the analysis, resulting in 324 samples.

For the analyses of Neftel’s single cell datasets, Smartseq2 data from their study were downloaded. Of the 7930 cells included in the dataset, the following cells were included: (1) cells from adult samples; (2) Cells from tumor cells clusters and (3) With available coordinates on the Neftel’s original cell state plot. (final = 4401 cells). Gene signatures were calculated by AUCell package. Both expression data and gene signature scores were min-max normalized and plotted on the Neftel’s dataset.

2.5.2 scRNA-seq data processing and quality control procedures[1]

For the analysis of single cell RNA-seq data, J. Keding from the Division of Applied Bioinformatics performed the analyses described in Sections 3.3.2 - 3.3.4 and Sections 6.1-6.2 while C. Imbusch from the Division of Applied Bioinformatics performed the analysis described in Section 3.3.7. Methods sections were written individually and incorporated into this method section.

Raw reads in FASTQ format were aligned to the mouse reference genome mm10 version 3.0.0 using the *count* function provided with the Cell Ranger software (10X genomics). A gene-cell count matrix (count = unique molecular identifier UMI) was generated for each samples and these gene-count matrices were used as the inputs for the Seurat package (v4.0). For filtering, cells with feature counts of 200 or less and cells containing 10% or more mitochondrial RNA, defined as features starting with the character string “mt-“, were filtered out. The filter counter matrices were then normalized using NormalizeData() function.

2.5.3 Clustering and dimensionality reduction

To perform clustering and dimensionaliry reduction, 2000 most variable features in the dataset were first identified FindVariableFeatures() provided in the Seurat package. The dataset were then undergone ScaleData() function. Afterward, RunPCA() function was applied to determine the first 30 principal components (PCs) using the 2000 most variable features calculated previously. To perform clusering, the functions FindNeighbours() and FindClusters() from the Seurat package were used. Briefly, FindNeighbors() function determined a K-Nearest Neighbous (KNN) graph to form the basis of heirarchical clustering using the Louvain algorithm to cacluate the clusters between the cells by the FindClusters() function (30 PC used, resolution parameter = 0.5). To visualize the high-demension data, RunUMAP() was used perform Uniform Manifold Approximation and Projection (UMAP), grouping transcriptionally similar cells in a low-dimensional space.

2.5.4 Cell cycle phases scoring

Scran package was used to assign the cell cycle phases in the tumor datasets. Mouse cell cycle marker genes were provided from the scran package and cell cycle scores and phase annotations were calculated using cyclone() function provided in the Scran package. Differences in the number of cells in each cell cycle phase between Ctrl and KD tumor cells were tested for significance while accounting for sample-specific variation using a generalized linear model (GLM) based on a binomial distribution.

2.5.5 Differentially regulated genes and pathways analysis

To determine the differentially expressed genes (DEGs) of each cluster, FindAllMarkers () function was used. The significance of the DEGs were computed using Wilcoxon tests with an adjusted (Bonferroni correction) p-value of 0.05. GSEA between Ctrl and KD tumor cells was performed based on the their

---

[1] Method description was adapted from J. Keding’s Master Thesis (Sections 2.5.2-2.5.6)

DEGs, using MSigDB curated datasets (species parameter = "Mus musculus"). GSEA was performed with GSEA() from the clusterProfiler package.

2.5.6 Analysis of copy number variations

Copy number variation (CNV) analysis were conducted using the R package infercnv using the stromal cells as a reference. CNVs were plotted as heatmap using the plot_cnv() from the infercnv package.

2.5.7 Single-cell gene signature scoring and pathway analysis

Gene signature activity in single cells was evaluated using AUCell (v.1.4.1). Whenever AUCell scores were visualized on heatmaps, signatures were scaled by z-score normalization and plotted with ComplexHeatmap. However, raw AUCell values were used when plotted as violin and scatter plots. Gene signatures were curated from the literature and has been cited throughout the result section.

2.5.8 Drug sensitivity index calculation

To evaluate the effectiveness of the combination treatment, a sensitivity index based on a previous study was calculated [201] . Briefly, the sensitivity index (SI) is the difference beweeen the expected combined effect (ECE) of the compound and 2 μM LY411575 and observed combined effect (OCE). The ECE is the defined as $\frac{Rc}{Cc} \times \frac{Cd}{Cc}$, where Rc and Cd are the luminscence intensities of the compound and LY411575 when used alone, Cc is the luminscence intensity of the DMSO control. OCE is defined as $\frac{Rd}{Cc}$, where Rd is the luminescent intensity when the compound and LY411575 were used together. A positive SI indicates that the ECE is greater than OCE, meaning that the observed survival of the co-treatment is smaller than the expected survival when the drugs were used indivudually (i.e. co-treatment exerts a higher inhibitory effect compared to single treatments). A mean SI from three technical replicates were calculated and SI above 0.2 was used as a cut-off.

3 Results

3.1 *SOX10*-high and *SOX10*-low GB samples occupy different cellular states

To determine the cell state plasticity mediated by *SOX10* in BTSCs, I first analyzed a BTSC transcriptome dataset assembled in a recent study [109] (n=144). Top and bottom decile *SOX10* expression in this cohort of BTSCs were classified as *SOX10*-high and *SOX10*-low BTSCs, respectively. Gene set enrichment analysis (GSEA) indicated that *SOX10*-high BTSCs enriched for OPC/Proneural-GB related cellular states, consistent with its role as a pivotal oligodendroglial TF and a master regulator of the RTK1/PN-GB. In contrast, *SOX10*-low BTSCs are strongly enriched for developmentally related cellular states, including NSC-related Type 1_GB and the recently proposed developmental GB [128], along with the classical and AC-like GB (**Figure 7A**). In line, the expression level of *SOX10* significantly anti-correlates with RTK2 master regulators, including *SOX9* and *EGFR*, along with NSC markers such as NES and *PAX6* (**Figure 7C**).

Next, I analyzed 324 primary GB IDH-WT samples with available *SOX10* expression information from the TCGA-GBM dataset, repeating the enrichment analysis using the same set of cellular state gene signatures with the same *SOX10* expression cut-offs (Top and bottom 10%, n = 33 and n= 32 for high and low samples, respectively). Again, developmental-like states were similarly enriched in *SOX10*-low bulk tumor samples (**Figure 7B**), with matching, significant anti-correlations between *SOX10* expression and these NSC-like markers, further suggesting that the developmentally related cell states associated with *SOX10*-low BTSCs were maintained at the tumor bulk level (**Figure 7D**).

Lastly, to ensure that the cell state changes observed above are tumor cell-intrinsic, I leveraged Neftel's dataset [127] (GSE131928) to include only the tumor cells from adult IDH-WT samples (n = 4401 cells) and visualized the cell state differences between *SOX10*-high and *SOX10*-low cells at the single cell level. *SOX10*-high cells predominantly occupied the OPC-like state. By contrast, *SOX10*-low cells occupied the rest of the cellular states, with a preponderance of the AC-like state, which overlapped with key NSC/Classical GB master regulators *SOX9* and *EGFR* (**Figure 7E and F**).

Taken together, these analyses in BTSCs, bulk tumor samples, and at single cell level supports the anti-correlation between *SOX10* expression on tumor cells and NSC-like developmental-like GB states, which are often associated with the aggressive features of the GBs [83]. Notably, the enrichment of development-GB-related cell states suggests that the *SOX10*-low BTSCs depart from the original OPC-like cell state, likely towards a more AC/NSC-like state commonly described in the TCGA-CL subtype.

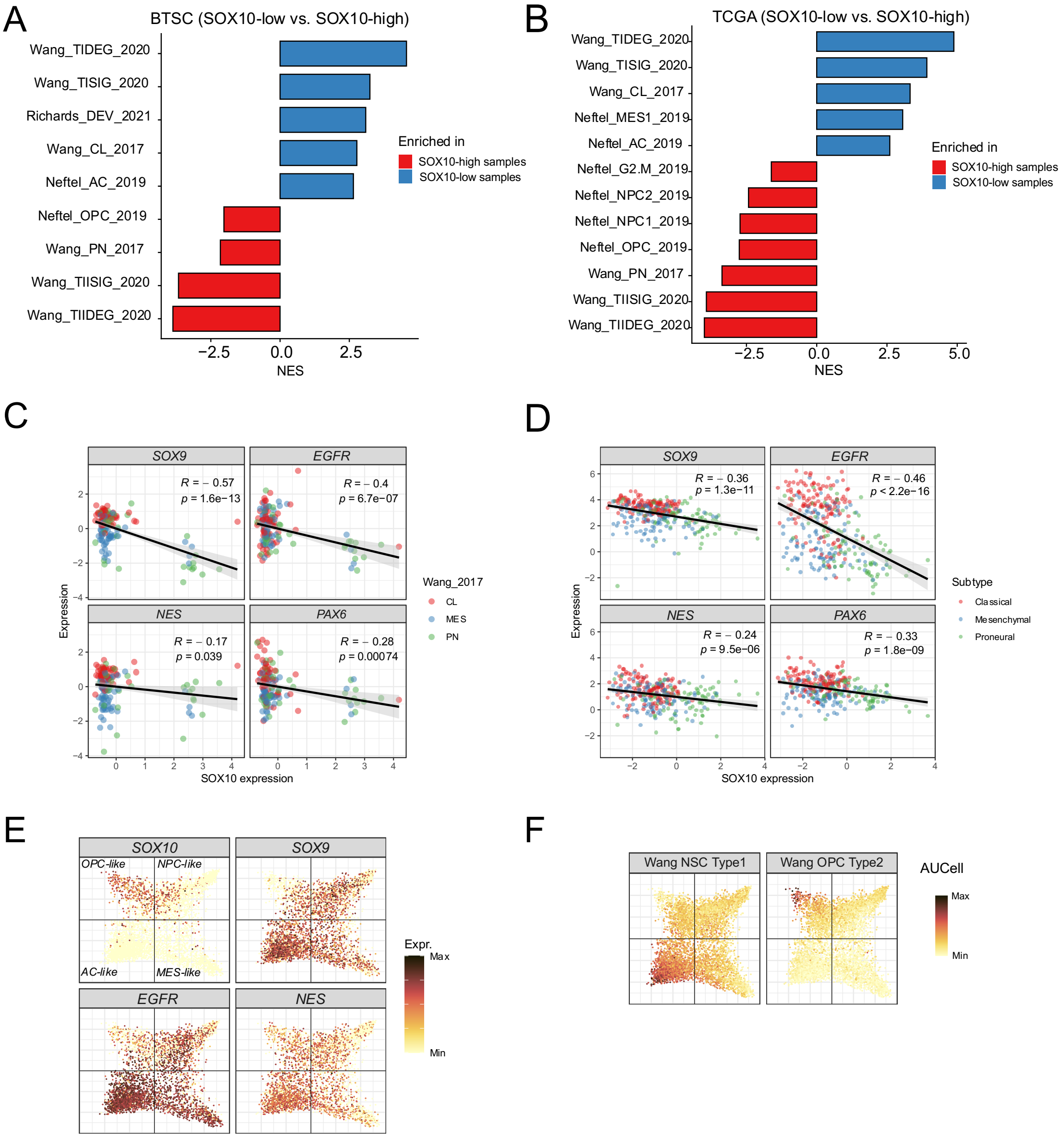

Figure 7. *SOX10*-high and *SOX10*-low samples occupy distinct cellular states on the developmental spectrum

(A,B) Bar plots summarizing the results of gene set enrichment analyses (GSEA) of the indicated gene sets curated from several studies. Differentially expressed genes between the top and bottom 10% of the samples in (A) a BTSC cohort (n=144) and (B) TCGA-GBM (primary IDH-WT GB samples, n=324) were stratified by *SOX10* expression were pre-ranked by log FC and used in this analysis. Positive NES indicates pathways enriched in the *SOX10*-low samples and vice versa. Only significantly enriched genesets (p. adj < 0.05) were shown. NES = normalized enrichment score. (C,D) Correlation between the expression of *SOX10* with other NSC/CL markers in (C) BTSC and (D) TCGA-GBM cohorts. Pearson correlation tests were used to compute R and p values, as indicated in the plots. (E) Scatter plots showing the normalized expression of *SOX10*, *SOX9* and *EGFR* on the scRNA-seq data from Neftel et al. (n=4401 cells). Expression values were scaled by min-max normalization. (F) Scatter plots showing the normalized AUCell score for the NSC- and OPC-like GB (Wang et al., 2020) using scRNA-seq data from Neftel et al. (n=4401 cells). Signature scores of the indicated gene sets were computed with AUCell and scaled by min-max normalization.

3.2 Sox10 downregulation mediates cell state transition in syngeneic GB models

3.2.1 Establishment of Sox10-knockdown (KD) model

To establish the causality between *SOX10* expression and cell state differences in GB cells, I took advantage of recently established murine GB syngraft models, in which a collection of mouse tumor cell lines were derived from Tailess (Tlx)-positive neural stem cells (NSC) through the inactivation of Pten and Trp53 [199]. Hence, these murine GB cells allow for the determination of the cell state changes in tumor cells in a defined genetic and lineage context. To determine the most suitable cell line for developing a mouse Sox10-KD model, I first queried published RNA-seq data of these mouse tumor cells (GSE145559). Gene expression analysis across the collection of cell lines showed that the cell line mGB1 has the highest expression of Sox10. Consistent with our previous observations in human patient data, the expression levels of the GB-subtype master regulators Sox9 and Egfr were anti-correlated with Sox10 expression in this collection of mouse cell lines (**Figure 8A**), suggesting this feature of human GB is conserved in mouse (**Figure 8A)**.

To generate Sox10 loss-of-function cell line models, Sox10 was knocked down in mGB1 using two short-hairpin RNAs (shRNA) targeting non-overlapping regions of Sox10. All shRNA tested achieved substantial KD of Sox10 expression at both the mRNA (**Figure 8B**) and protein levels (**Figure 8C**). In addition, I generated control cell lines using non-targeting shRNA. Hereafter, these cells will be referred to as Ctrl and KD cells, respectively.

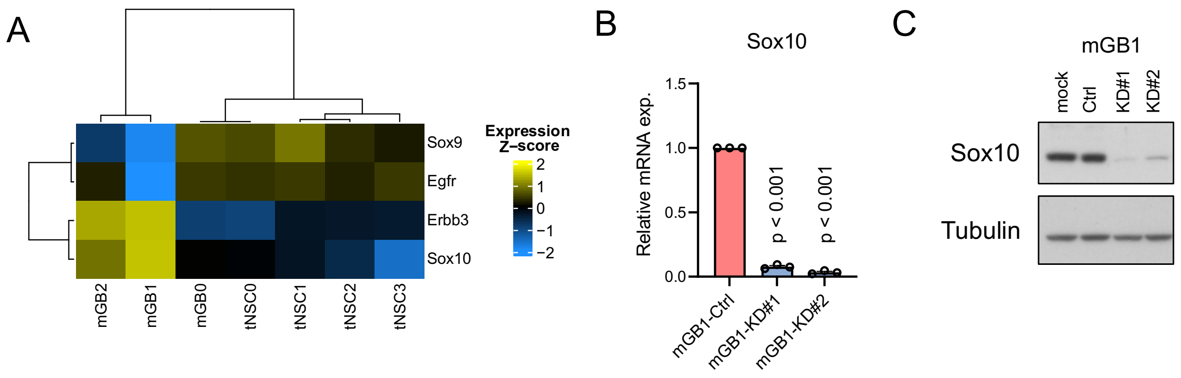

Figure 8. Establishment of Sox10-KD murine mouse cells for this study

(A) Heatmap showing the RNA expression z-scores of selected subtype master regulator genes. The expression data were downloaded from GSE145559 (B) Bar chart showing the relative mRNA expression of Sox10 upon transducing with lentiviral particles containing Ctrl-shRNA (mGB1-Ctrl) or shRNAs against Sox10 (mGB1-KD#1 and mGB1-KD#2). Data are represented as mean ± SEM from three experiments. One-sample t-tests (mean value of 1). (C) Evaluation of KD efficiency by western blots. Mock represents untransduced cells. Tubulin was used as the loading control.

3.2.2 Aggressive features of KD tumors

To assess the effect of Sox10 knockdown on GB growth *in vivo*, Ctrl and KD cells were intracranially injected into the immunocompetent C57BL6/J mice. Tumor growth was monitored by T2-magnetic resonance imaging (MRI). Both Ctrl and KD cells engrafted and developed full-blown tumors within 100 days post-injection, consistent with the original report from which these cell lines were first established [199]. Strikingly, KD cells developed tumors with much shorter latency than Ctrl cells, typically forming large tumors (above 50 µl as measured by T2-MRI) within 8 weeks after injection (**Figure 9A**). Additionally, upon inspection of the T2 MRI images, as tumors developed over time, Ctrl tumors arose from a circumscribed location, while KD tumors were more infiltrative and rapidly spread to other parts of the brain (**Figure 9B**). Dramatic gross appearances were observed in Ctrl and KD tumors after harvesting the tumors. Ctrl tumors formed bulky tumors within the hemisphere where the tumor cells were injected, whereas KD tumors were highly infiltrative and vascularized, suggesting a higher complexity of KD tumors (**Figure 9B**).

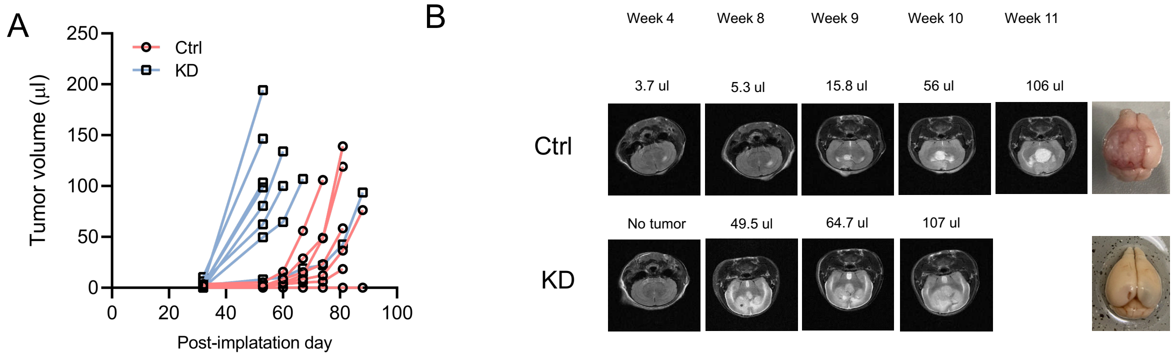

Figure 9. Development of Ctrl and KD tumors in syngeneic hosts

(A) Tumor formation in C57BL6/J mice injected with mGB1 cells expressing non-targeting shRNA (Ctrl) and shSox10 (KD). Each mouse was intracranially injected with 200,000 cells. Tumor sizes were monitored by T2-MRI. (B) Representative MRI images showing the development of Ctrl and KD tumors after the indicated weeks post-implantation. Tumor volumes at the indicated timepoints are given above each image. Colored images on the right show the appearance of tumors upon harvest. Note that Ctrl tumors are circumscribed, whereas KD tumors are highly infiltrative and vascularized.

Histological features of the representative tumors from both genotypes were examined by a pathologist (Dr. Andrey Korshunov, Department of Neuropathology, University Hospital Heidelberg), revealing grade IV GBs in both genotypes. However, despite having similar tumor sizes (around 100 µl in volume) and the same tumor grading, Ctrl and KD tumors displayed distinctive growth patterns - Ctrl tumors were largely hemispheric, whereas KD developed large, "butterfly-like" bi-hemispheric GB with histological features such as numerous necrotic areas, reminiscing the more aggressive form of human grade IV gliomas [202]. This type of bilateral growth pattern of KD tumors further highlights the tumor cells' potential to invade the contra-lateral hemisphere via the white matter tract of the corpus callosum [202, 203]

Upon closer examination of the tumor region, KD tumors' tumor boundaries were less well-defined than Ctrl tumors, with numerous “islands” of tumor cells near the edges. In the tumor core regions, tumor cell density was substantially higher in the KD tumor cells compared to the Ctrl tumors, suggesting that active tumor expansion occurs within the KD tumors (**Figure 10A**). Additionally, immunohistochemistry analysis of tumor sections revealed that KD tumors showed a marked increase in the infiltration of Iba1-positive tumor-associated macrophages (TAMs) in both the tumor core and tumor edges, consistent with the immune phenotype of highly aggressive GB (**Figure 10B**). Reducing Sox10 expression in mouse NSC-derived GB cells collectively enhances the tumorigenicity and aggressive properties of tumors, potentially leading to changes in the landscapes of both tumor and immune cells.

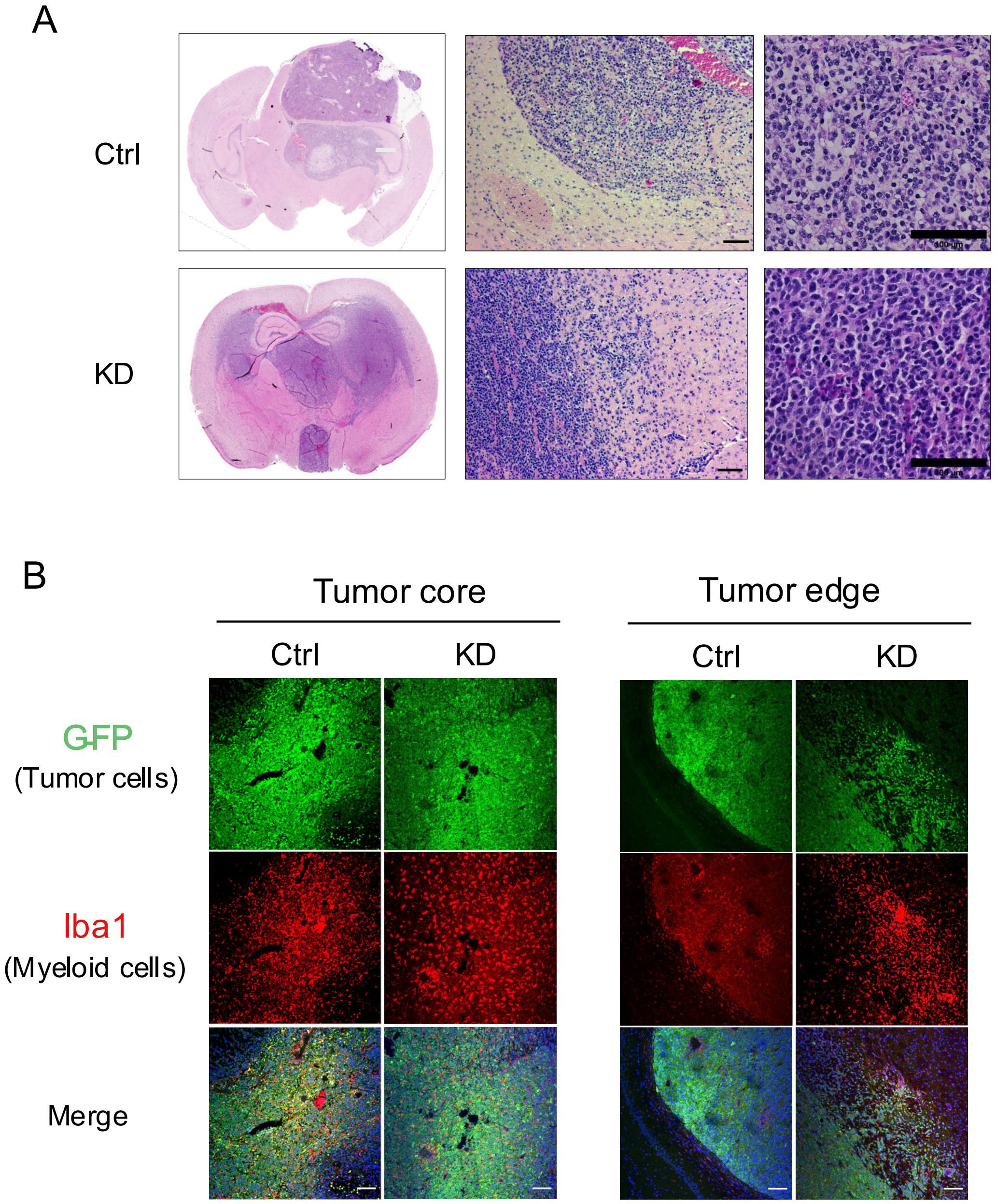

Figure 10. Histological features of Ctrl and KD tumors.

(A) Representative images showing the H&E staining of coronal brain sections of mice bearing Ctrl and KD tumors. Images in the middle show the typical histological features of the tumor edge, and images on the right show the typical histological features of tumor cores. (B) Immunohistological analysis of GFP-labeled tumor cells (green) and Iba1-positive myeloid cells, comprising tumor-associated macrophages and brain-resident myeloid cells (red) in both the tumor core (left) and tumor edge (right). Scale bars = 100 µm.

3.2.3 Expression profiling of KD and Ctrl tumors identified global differences in the biological activities of Ctrl and KD tumors

To gain insights into the mechanisms that lead to the enhanced aggressive properties in the current KD tumor model, I analyzed bulk RNA-seq transcriptomic data of Ctrl and KD tumors (Ctrl: n = 3, KD: n = 5), which was previously generated by our group (GSE121718). In the KD-tumors, an enrichment of MES gene-expression signatures (TCGA-MES [31]), as we had reported in human cell lines cultured in serum-containing media, could not be observed (**Figure 11A**). This suggests that the aggressive phenotypes are unlikely to be mediated through MES transition of KD tumor cells.

Nevertheless, the KD tumors showed enhanced ssGSEA scores related to the TCGA-CL (**Figure 11B**). In addition, further pathway analysis using collections of gene signatures deposited on Gene Ontology-Biological Processes (GO-BP) and Kyoto Encyclopedia of Genes and Genomes (KEGG) revealed substantial differences between these tumors. Specifically, pathways related to the regulation of nervous system development were significantly enriched in the KD tumors. In contrast, Ctrl tumors show enrichment in metabolic pathways such as carbohydrate metabolism, including glycolysis and the pentose phosphate pathway. Hence, pathway analysis of bulk RNA-seq data revealed distinct molecular profiles between Ctrl and KD tumors, wherein KD tumors exhibit characteristics reminiscent of neurodevelopment while Ctrl tumors seem to be sustained by metabolic programs involved in energy production or usage (**Figure 11C and Figure S4**).

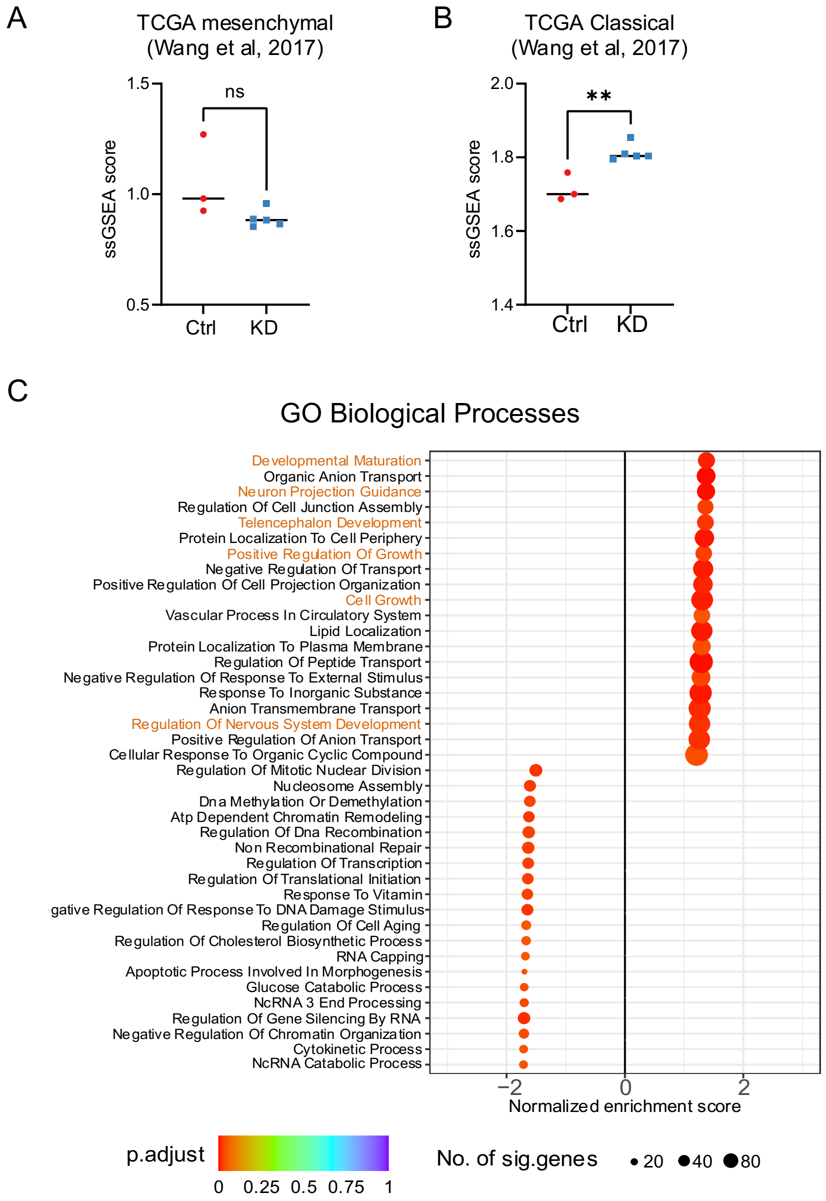

Figure 11. Analysis of bulk RNA-seq data of Ctrl and KD tumors.

(A and B) Scatter plots showing the single sample GSEA (ssGSEA) scores of (A) TCGA mesenchymal and (B) TCGA Classical (both from Wang et al., 2017 [31]) of the Ctrl (n = 3) and KD (n = 5) mice. (Mean value with p values computed using Two-tailed T-tests of the ssGSEA scores). (C) Summary of Gene set enrichment analysis using GO Biological Processes. X-axis depicts the normalized enrichment score (NES) of the geneset. A positive NES means the geneset is enriched in the KD tumor cells, whereas a negative NES means the geneset is enriched in the Ctrl tumor cells. Genesets were arranged by their enrichment scores, and the top 20 enriched genesets of KD and Ctrl tumors were shown. Genesets related to development were highlighted. Further analysis against KEGG pathways deposited on MSigDB were shown in **Figure S4**.

3.2.4 Sox10-controlled GB transcriptional and phenotypic plasticity resembles features of recently proposed GB subtypes

The analyses above indicated the resemblance of KD tumors to development, which is often employed by GB cells to mediate their aggressive properties [124, 127]. In the same vein, during the development of NSCs into OPCs or oligodendrocytes, the expression of *SOX10* in NSC specifies their fate toward oligodendrocytic differentiation. Based on this evidence, I reasoned that by downregulating *SOX10* expression in tumor cells, they might revert to a cellular state similar to NSCs, thereby driving tumor aggressiveness.

In line with my observations, a recently proposed cell of origin-based GB classification also demonstrated higher expression of *SOX10* and *ERBB3* in the oligodendrocyte precursor cells (OPC)-derived Type 2 GB, whereas the more aggressive, neural stem cell (NSC)-derived Type 1 GB showed lower Sox10 expression [133]. Indeed, Type 1 GB proposed in that study bares remarkable histological resemblance to our KD tumors, including shorter latency to full-blown tumors, increased invasive properties and active tumor expression. Importantly, GSEA of our bulk RNA-seq data using Type 1 and Type 2 GB gene signatures revealed that Ctrl tumors resemble Type 2 GBs, whereas Type 1 GB signature is enriched in KD tumors (**Figure 12A**). Concordantly, type 2 GB markers Sox10 and Erbb3 were significantly upregulated in Ctrl tumors, while type 1 GB markers Sox9 and Egfr were significantly upregulated in KD tumors (**Figure 12B and D**).

Collectively, my results presented in this section suggest that the downregulation of Sox10 in tumor cells mediates the cell state switch from the more OPC-like to the more developmental-like GB. Importantly, the data supports a lineage switching role driven by Sox10 downregulation in tumor cells, imparting differential developmental fates in tumors, in line with the plastic hierarchical BTSC model from other recent studies [119, 127].

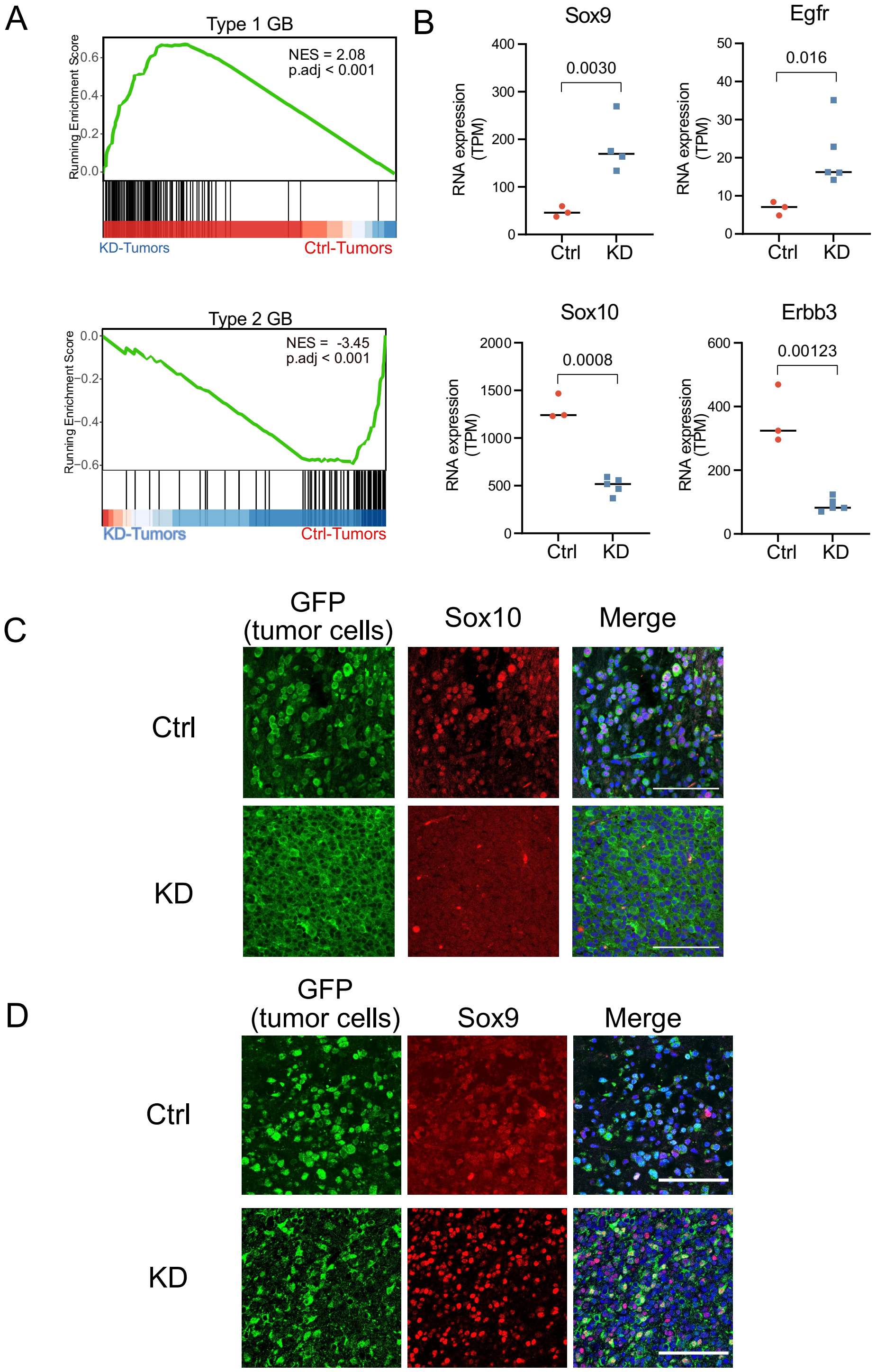

Figure 12. Development of Ctrl and KD tumors in syngeneic hosts.

(A) GSEA plots showing enrichment of Type 1 GB gene signature [133] in KD tumors and Type 2 GB profiles in Ctrl tumors. Genes were pre-ranked by their log2 expression values in KD cells over Ctrl cells.NES: Normalized Enrichment Score, p.adj: adjusted p-value (B) Expression of Type 1-GB genes Sox9 and Egfr (above) and Type 2-GB genes Sox10 and Erbb3 (below). Adjusted p-values between expression values from Ctrl and KD mice were calculated with DESeq2. (C and D) Representative immunofluorescence images of Sox10 (Type 2 GB marker) and Sox9 (Type 1) GB markers in Ctrl and KD mice. Scale bar: 100 µm.

3.3 Single-cell RNA-seq reveals that the loss of Sox10 in tumor cells imparts differential tumor cell fates

In the last section, I demonstrated that Sox10 downregulation leads to a phenotypic switch from the OPC-like, less aggressive Type 2 GB toward the more aggressive, NSC-derived Type 1 GB. While the bulk RNA-seq analysis revealed considerable differences between Ctrl and KD tumors, detailed exploration entails a more granular picture of the cellular architecture and dynamics due to the reduced expression of *SOX10* in tumor cells. As such, single-cell RNA-seq of the KD and Ctrl tumors to comprehensively characterize the tumor and stromal landscapes of KD control and KD tumors at a more granular level.

3.3.1 Establishment of scRNA-seq

To address the tumor cell landscape changes accompanied by Sox10 downregulation in tumor cells, I designed a workflow for the single-cell study, which would enable interrogations of the changes of both tumor cells and immune cells associated with Sox10-KD. As shown in **Figure 13A**, the workflow starts with injecting Ctrl and KD cells into immunocompetent C57BL/6J mice. It has been reported that the landscapes of tumor and stromal cells can differ considerably at different stages of tumor development. To allow for a comparison of tumors at their respective advanced stages, only tumors with sizes above 50 µl (as measured by T2 MRI) were included, leading to 3 Ctrl mice and 4 KD mice in this study. Tumors were harvested ensuring minimal inclusion of normal brain areas, and were dissociated using the tumor dissociation method detailed in Chapter 2. Cells were then sorted by flow cytometry to separate the viable GFP-positive tumor cells and GFP-negative stromal cells using the gating strategy shown in **Figure 6**. The sorted cells were then subjected to 10X single-cell library preparation and sequencing. I worked closely with J. Keding (Division of Applied Bioinformatics) for the initial analyses of the single-cell analysis data. Figures produced by her have been indicated as such.

3.3.2 Overview of the dataset

After sequencing the libraries prepared from tumor and stromal fractions from 3 Ctrl mice and 4 KD mice, raw data were processed by J.Keding. Quality control (QC) procedures, including removing cells with a low number of reads or genes detected and cells with high mitochondrial RNA contents, were applied, yielding a total of 116,533 cells with a median of 1,039 genes detected per cell. For the GFP-positive (GFP-pos) tumor samples, 65,870 cells were retained after QC, whereas 50,621 cells were retained for GFP-negative (GFP-neg) samples.

To gain an overview of the dataset, unsupervised hierarchical clustering of all filtered cells was performed using the Louvain community detection method provided in the Seurat package. This analysis identified 27 transcriptional clusters, further visualized by Uniform Manifold Approximation and Projection (UMAP), a dimensionality reduction method commonly used to visualize high-dimension scRNA-seq data. Expectedly, GFP-pos and GFP-neg cells were clearly separated from each other, suggesting that FACS based on GFP positivity successfully isolated tumor cells and stromal cells, respectively. Interestingly, comparing tumor and stromal fractions between Ctrl and KD on the UMAP space, a clear separation was observed between Ctrl and KD tumor cells, whereas the differences between Ctrl and KD stromal cells were relatively subtle, suggesting that tumor cells constitute a bigger difference in the dataset (**Figure 13B and C**). Collectively, initial data analysis indicated the successful separation of tumor and stromal cells and demonstrated that the biggest difference between the KD and Ctrl tumors likely stems from the tumor cell fractions, implicating that the differences between tumor cells may account for the phenotypic differences between these genotypes.

For the remainder of this section, I will focus on the differences observed in the tumor cell fractions. The differences between stromal cells are beyond the scope of the current study and will be summarized as the supplementary information to this thesis.

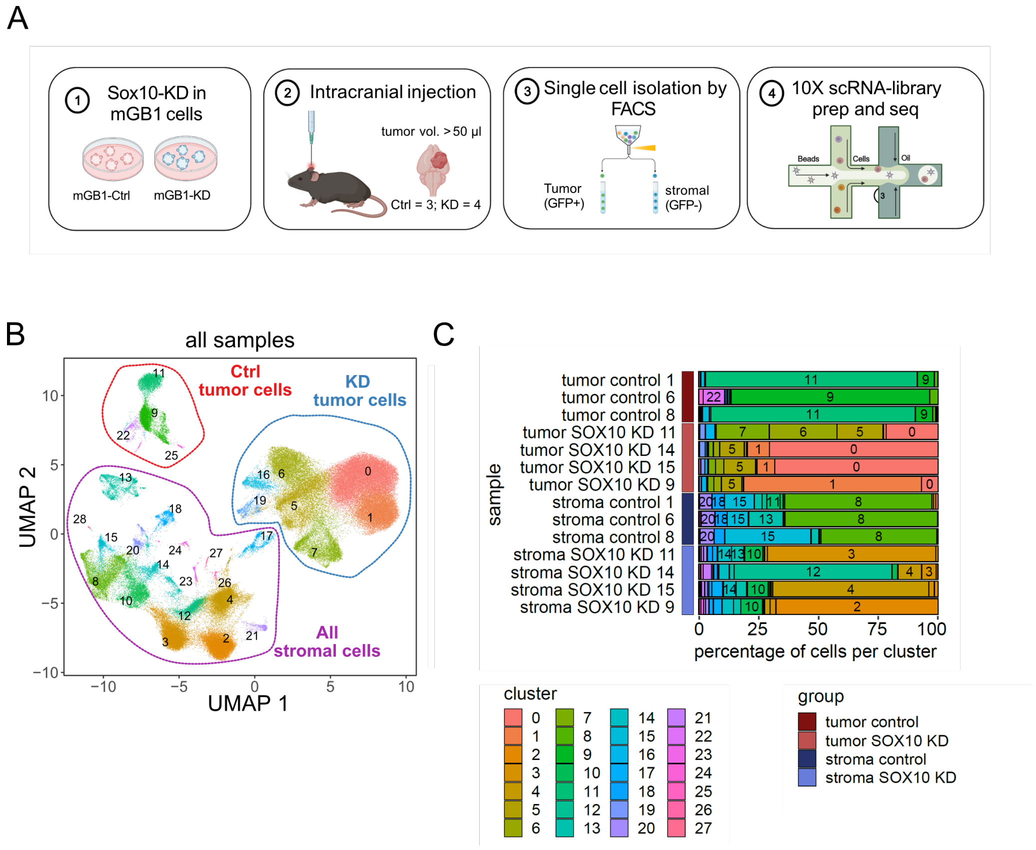

Figure 13. Overview of workflow and the dataset.

(A) Flowchart showing the workflow of the single-cell study. Sox10 expression was knocked-down using shRNA in mGB1 cells. Afterward, Ctrl and KD tumor cells were injected intracranially into immune-competent C57BL/6J mice. Tumors were harvested upon large size (50 µl by T2 MRI; Ctrl = 3 mice and KD = 4 mice). Tumors were resected and dissociated, and then, tumor and stromal fractions of each tumor were separated by flow cytometry based on GFP expression. Tumor and stromal fractions were subjected to 10X scRNA libraries preparation and sequencing**.** (B) A UMAP plot showing the clustering and dimensionality reduction of all cells in this single-cell study. The plot was annotated by samples types, namely tumor cells from Ctrl and KD and stromal cells from Ctrl and KD, respectively. (C) Bar charts show each transcriptional cluster's relative contribution (28 in total) in all the samples. (This bioinformatic analysis was performed by J. Keding, and she generated the figures)

3.3.3 Single-cell analysis reveals global differences between Ctrl and KD tumor cells

The central research question I would like to address through single-cell sequencing analysis is the plasticity mediated by Sox10-KD in tumor cells. To this end, GFP-pos cells in the dataset were extracted. We further compared the CNV profiles of GFP-positive cells (65,870 cells) and identified large-scale chromosomal aberrations compared to GFP-neg stromal cells, confirming that GFP-positive cells are tumor cells (**Figure S5A).**

Unsupervised hierarchical clustering of these tumor cells from Ctrl and KD was then performed, identifying 16 transcriptional clusters, which were further visualized on the UMAP space (**Figure 14A**). KD tumor cells and Ctrl tumor cells were largely separated from each other, indicative of the divergent tumor cell fates between KD and Ctrl cells. In addition, KD tumor cells displayed enhanced heterogeneity, as more transcriptional clusters could be identified, in line with previous histological and molecular observations of these tumors. To ensure that this separation between Ctrl and KD tumors is not due to differences in cell cycle-related genes, another clustering was performed after regressing out the cell cycle effect. The clustering result is largely comparable to that without cell cycle effect regression, with the Jaccard similarity index between best-matching clusters pre- and post-regression being 0.87 (**Figure S5B**). Hence, cell cycle score differences between Ctrl and KD tumors minimally affect the clustering results and would therefore be retained in subsequent analyses.

To pinpoint the differences between Ctrl and KD tumors, gene set enrichment analysis (GSEA) was performed using Hallmark and GO-BP gene sets available on the Molecular Signature Database (MSigDB). Results of this pathway analysis revealed that the significantly enriched pathways (adjusted p-value < 0.05) in KD tumors were mainly associated with their aggressive features, including gene sets related to cell proliferation such as "G2M checkpoint", demonstrative of active tumor expansion within the KD-tumors. Furthermore, consistent with my observations in bulk RNA-seq data, gene-sets related to development, such as "brain development" and "Central nervous system development," were similarly enriched in KD tumors, suggesting the resemblance of KD tumors to development. In contrast, Ctrl tumors showed enrichment in pathways related to immune response, including "Interferon Gamma Response" and "Antigen Processing and Presentation" (**Figure 14C and D**). The enrichment of these immune-related pathways in Ctrl tumor cells indicates that the tumor cells are likely under immune attack from the stromal compartment, leading to restriction in tumor growth compared to KD tumors.

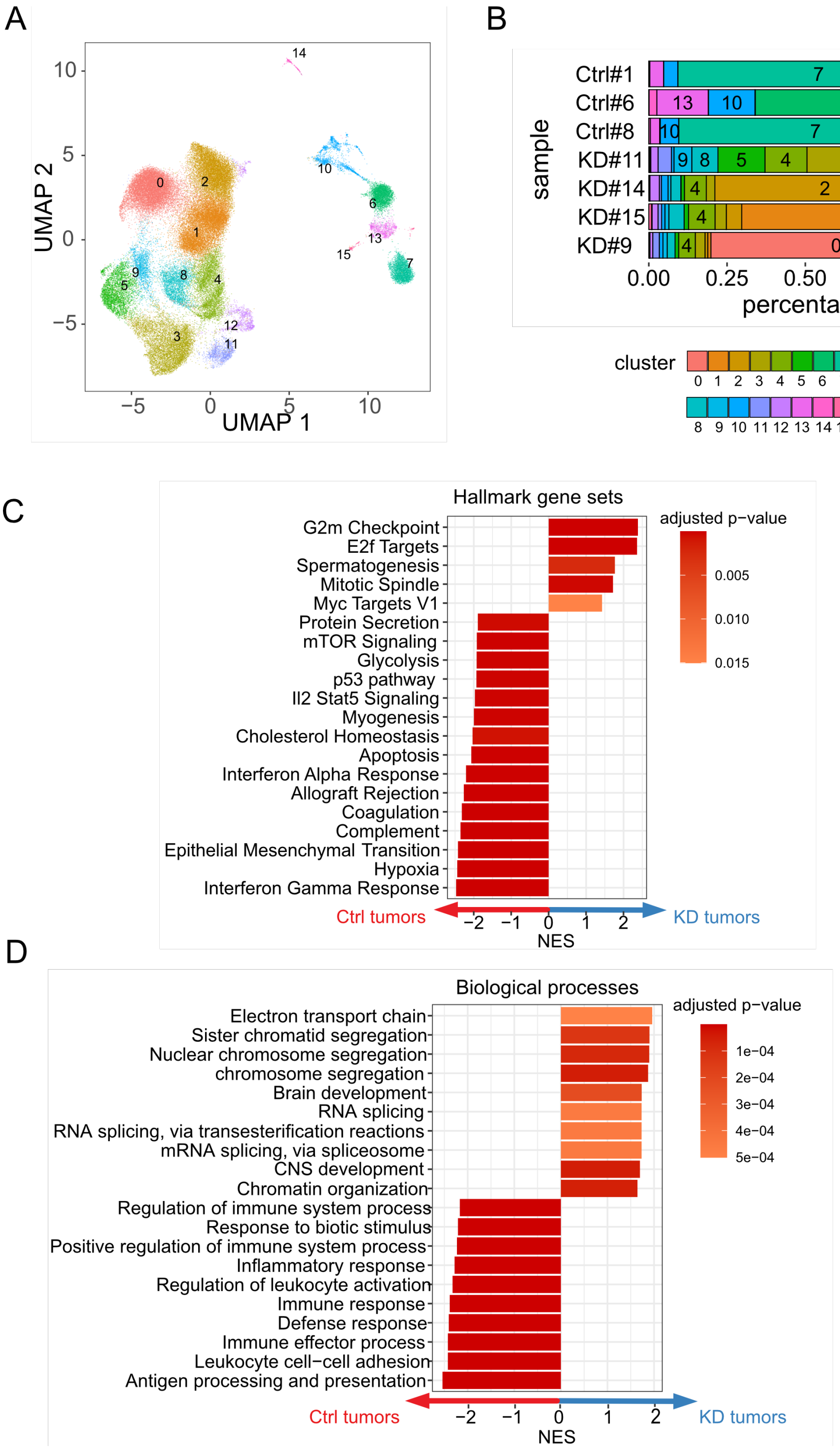

Figure 14. Single-cell RNA-seq analysis revealed global differences between Ctrl and KD tumor cells.

(A) UMAP visualization of tumor cells (n = 65870) by transcriptional clusters. (B) Barcharts showing the contributions of each transcriptional cluster in each sample. X-axis depicts the percentage abundance of the transcriptional clusters in each sample. (C) Bar chart showing the significantly enriched genesets and pathways (adjusted p-value < 0.05) using (C) hallmark genesets and (D) GO- biological processes. X-axis depicts the normalized enrichment score (NES) of the geneset. A positive NES indicates the geneset is enriched in the KD tumor cells, whereas a negative NES indicates enrichment in the Ctrl tumor cells. Top enriched genesets were shown in KD and Ctrl tumor cells (This bioinformatic analysis was performed by J. Keding, and she generated the figures.)

3.3.4 Cell cycle score analysis revealed a higher abundance of rapidly cycling cells in KD tumors

Likewise, cell cycle scoring analysis of the scRNA-seq data revealed that KD and Ctrl tumor cells differ in their proliferative capacity. Specifically, cell cycle scores at G1, S and G2 phases were assigned to each tumor cell according to the expression level of genes involved in these cell cycle phases using the Seurat cell cycle scoring function. Results of the cell cycle scoring analysis showed that KD tumor cells, in general, have significantly higher G2/M cycle scores compared to Ctrl tumor cells ($p < 0.001$) (**Figure 15A**). Accordingly, a significantly higher percentage of KD tumor cells was at the fast-cycling G2/M phase (44.7% in KD vs. 19.3% in Ctrl) (**Figure 15B**). Overall, the analysis here indicated that a greater proportion of KD tumor cells were at the G2/M phase than in the control cells, in agreement with the rapid expansion of the KD tumors. (**Figure 10**).

Interestingly, despite having a higher abundance of fast-cycling tumor cells, KD tumors were heterogeneous regarding their proliferative capacity. Notably, the highly proliferative tumor cells were mainly found in large clusters such as clusters 0, 1 and 2, whereas clusters such as 3, 11 and 12 were in a slow-cycling phase. This tumor cell proliferative capacity disparity was not as pronounced in Ctrl tumor cells, where most tumor cells were at the G1 phase (**Figure 15C to F**). Hence, expression-based cell cycle scoring in the current scRNA-seq dataset revealed the abundance of rapidly cycling cells within KD tumors, even though heterogeneity in proliferative potentials exists.

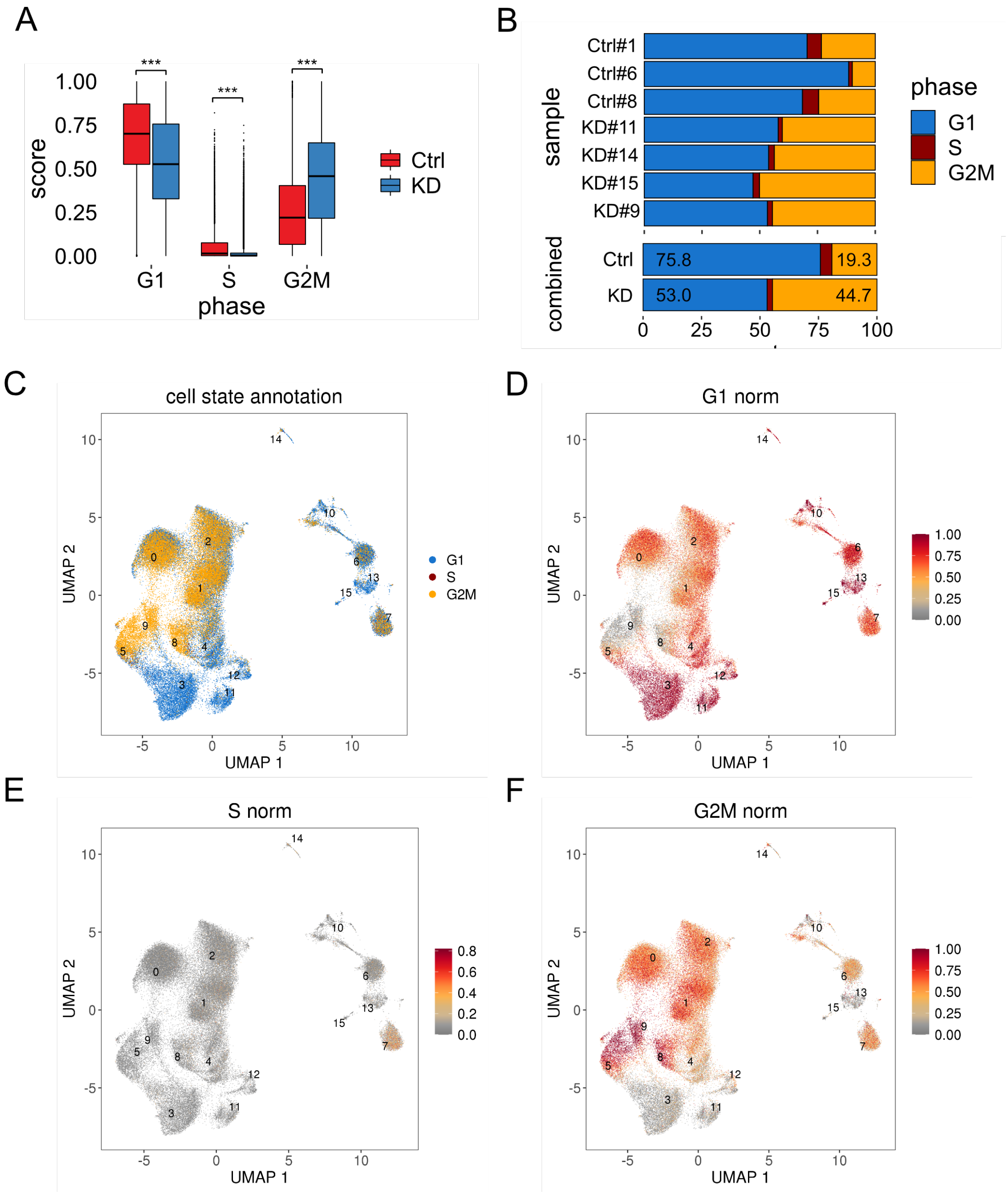

Figure 15. Cell cycle analysis of the tumor cells.

(A) Boxplots showing G1, S and G2/M phase scores of each cell in Ctrl and KD tumor samples. Data are represented as median cell cycle score +/- 1.5 IQR. P vaues were computed two-tailed Wilcoxon's rank sum tests.***P<0.001 (B) Percentage of cells in each cell cycle phase per sample (top) and group (bottom). (C to F) UMAP plots depicting the distribution of the cell cycle phases in the dataset (This bioinformatic analysis was performed by J. Keding, and the figures were generated by her)

3.3.5 Stemness and Developmental GB

Analyses in both bulk RNA-seq and scRNA-seq highlighted that KD tumors mirror the development of NSCs. Therefore, I compared our dataset with other relevant gene sets to better characterize this property. To accurately perform signature-scoring in scRNA-seq data, I chose AUCell, which computes the activity of a given gene-set or signature by calculating its area under the curve (AUC) over a pre-ranked list of genes based on their expression values in a given cell. Hence, the resultant AUCell score represents the proportion of genes in the gene sets that were highly expressed in a given cell [204].

In keeping with the roles of *SOX10* in oligodendrocyte differentiation, Ctrl tumors have significantly higher gene signature scores for oligodendrocytes-related gene-sets compared with KD tumors (mOL: mature oligodendrocytes and OD: oligodendrocytes; both $p < 0.001$), with concurrent upregulation of key markers in this process such as Plp1 and Mbp (both $p < 0.001$) (**Figure 16A and B**). Coupled with the cell cycle scoring analysis above, these indicate that Ctrl-tumor cells were more differentiated and thereby less proliferative than KD tumor cells, tying in with their less aggressive features. Interestingly, Ctrl tumor cells have a higher AUCell score for Injury-GB compared to the KD tumors ($p < 0.001$) (**Figure 16E**). This increase in differentiation and injury response in Ctrl-tumor cells is consistent with a previous report suggesting that *SOX10*-high GBs become differentiated due to the injury response impinged on tumor cells as they migrate along the white matter tract in the corpus callosum in a human PDOX model [205].

In contrast, KD tumor cells showed elevated AUcell scores for cancer stemness gene signatures derived from two studies [122, 124] (both $p < 0.001$), implying that KD tumors possess more prominent stem cell features (**Figure 16C**). Indeed, Sox10 KD in Type 2-like mGB1 cells rendered the tumors more Type 1-like, as indicated by significantly higher Type 1 GB AUCell scores ($p < 0.001$), in line with my observations in bulk RNA-seq data (**Figure 16D**). Along the same line, signature-scoring analysis using another recently proposed Developmental-Injury GB signatures revealed that KD tumors show a striking resemblance to the developmental subtype of GB [128](derived from $p < 0.001$), consistent with the association of Type 1 GB with NSC development [128] (**Figure 16E**). Likewise, KD-tumors showed a strong upregulation of markers related to NSCs, including Sox2, Nes and Ptprz1, indicative of a more stem/progenitor-like state, which is often associated with enhanced tumor aggressiveness [83, 124, 206] (**Figure 16F**). Taken together, findings from scRNA-seq here support my hypothesis that reduced expression of Sox10 in tumor cells mediates plasticity via switching to a more stem/progenitor cell-like state. Furthermore, my findings further highlight the divergence of tumor cell fates between Ctrl and KD tumors, strongly implicating Sox10 as one of the transcription factors regulating this tumor cell plasticity.

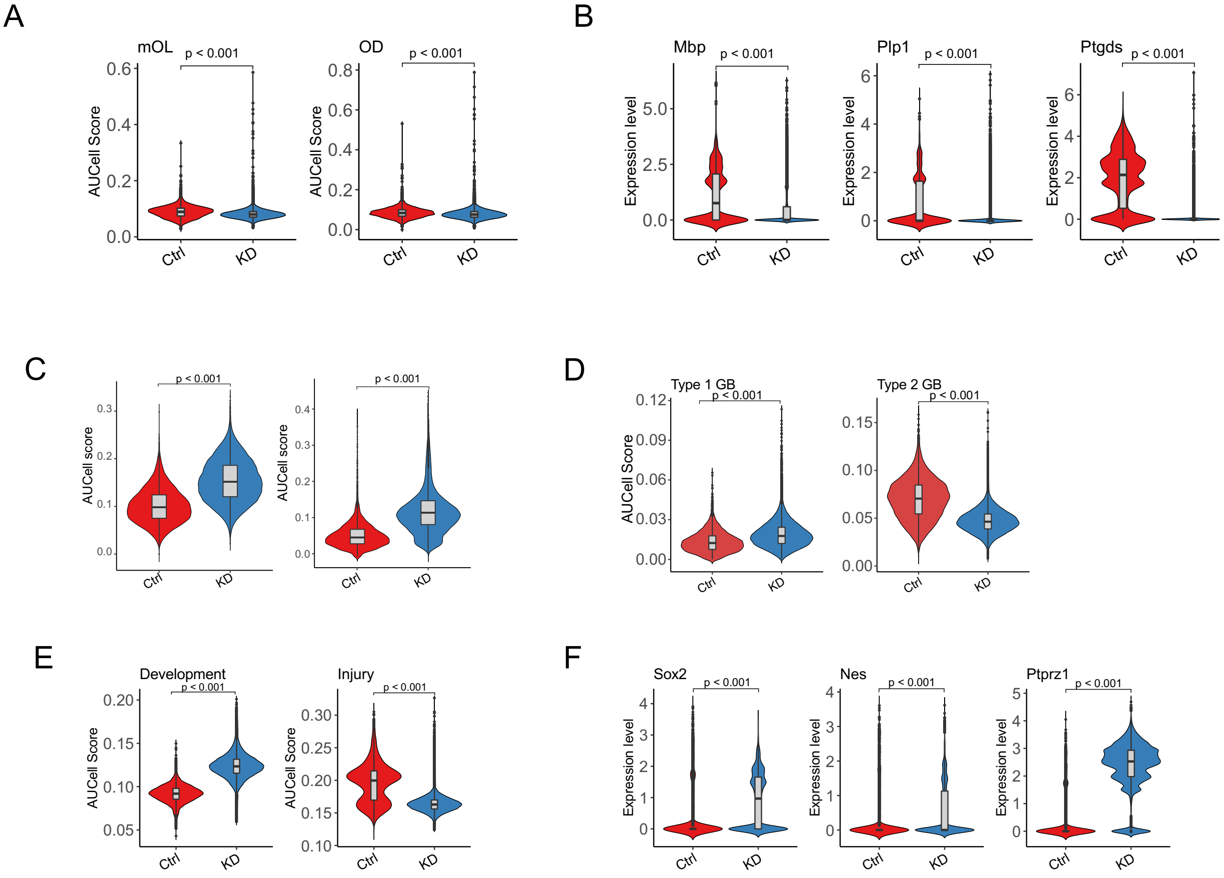

Figure 16. Signature scoring revealed enhanced stemness and developmental-like features in the KD tumor cells.

(A) Violin plots showing the AUCell scores for the genes signatures related to oligodendrocytes (mOL: mature oligodendrocytes gene signature extracted from Weng et al. OD: oligodendrocytes gene signature extracted from Kalamakis et al.) in Ctrl and KD tumors. (B) Violin plots showing the expression levels of genes related to oligodendrocyte development (Mbp, Plp1 and Ptgds) in Ctrl and KD tumors. (C) Violin plots showing the AUcell scores for the gene signatures related to glioblastoma stemness extracted Triosh et al., 2016 [124] (left) and Couturier et al., 2020 [122] (right). (D) Violin plots showing the AUCell scores for Type 1 and Type 2 GB gene signatures derived from Wang et al., 2020 (E) Violin plot showing the AUCell scores for Development and Injury like GB from Richards et al., Nature Cancers, 2020 in Ctrl and KD tumors. (F) Violin plots showing the expression of representative NSC-related genes (Sox2, Nes and Ptprz1). AUCell score was used to compute the scoring of the indicated signature. The median AUCell scores ± interquartile ranges are reported in the grey box in each violin plot. For both AUCell scores and gene expression values comparisons, levels of significance were calculated using unpaired two-tailed Wilcoxon's rank sum test, and p values were reported above each violin plot.

3.3.6 Comparison of KD tumor cells to normal NSC development

Next, I examined the markers of each transcriptional cluster to further dissect the intratumoral heterogeneity within Ctrl and KD tumors. **Figure 17** shows each transcriptional cluster's top 3 differentially expressed genes ($p < 0.05$, Wilcoxon tests). Tying in with pervious pathway and cell cycle analyses, clusters in Ctrl tumors (clusters 6, 7 and 13) upregulate markers implicated in oligodendrocyte differentiation (Plp1 and Mbp) [207], injury response (Erol1) as well as carbohydrate usage (Pgk1) [127]. Most of these clusters had lower expression of genes involved in cell proliferation (red dashed-boxes in **Figure 17A**).

On the contrary, clusters in KD tumors can be roughly grouped into four classes based on their marker genes, as summarized in (**Figure 17B and C**). Clusters 0,1 and 2 are the predominant clusters within the KD tumor cells, and they possess markers indicating stem/progenitor cell features involved in the NSC or GB, including Fabp7/Blbp [208], Ppp1r14b [206] and C1ql1 [132]. Some clusters within this progenitor cell category, for example, clusters 4 and 8, also possess cell cycle and proliferation programs, indicating their presence in KD tumors may be important in fueling tumor growth. The second group of clusters (clusters 5 and 9) had the strongest expression of genes related to the cell cycle and possessed markers reminiscent of intermediate progenitor cells or transit-amplifying cells during neurogenesis, including Chd7 and Ascl1. The third group of KD tumor cells comprises clusters 3 and 11, which express genes related to more differentiated progenies along NSC lineage progression, such as S100b, a mature astrocyte marker [209], and well-known markers for neuronal lineages such as Map2, S100a1 and Gap43. This group of cells is also largely devoid of expression programs related to cell proliferation, consistent with their more differentiated-like properties. Finally, cluster 12 expresses early or quiescent NSCs (qNSC) markers. These genes and markers include Sox9, an important regulator of the quiescence state of NSCs [68]. Target genes involved in the Notch signaling pathway, such as Hes5 and Hey1, critical in maintaining NSCs in quiescent or dormant states, were also upregulated in this cluster. Interestingly, radial glial cell (RGC) markers such as Hopx, Vcam1 and Lifr [210, 211] were also upregulated in this cluster. During murine postnatal development of NSCs in the SVZ, this group of qNSC preserves the pool of progenitor cells and gives rise to both glial and neuronal progenies through activation of cell cycle programs upon suitable cues in the environment [67, 68]. Collectively, cluster-wise investigation of marker genes in each cluster further revealed the stemness properties of KD tumor, in that the clusters bear a resemblance to each of the sublineages along NSCs development.

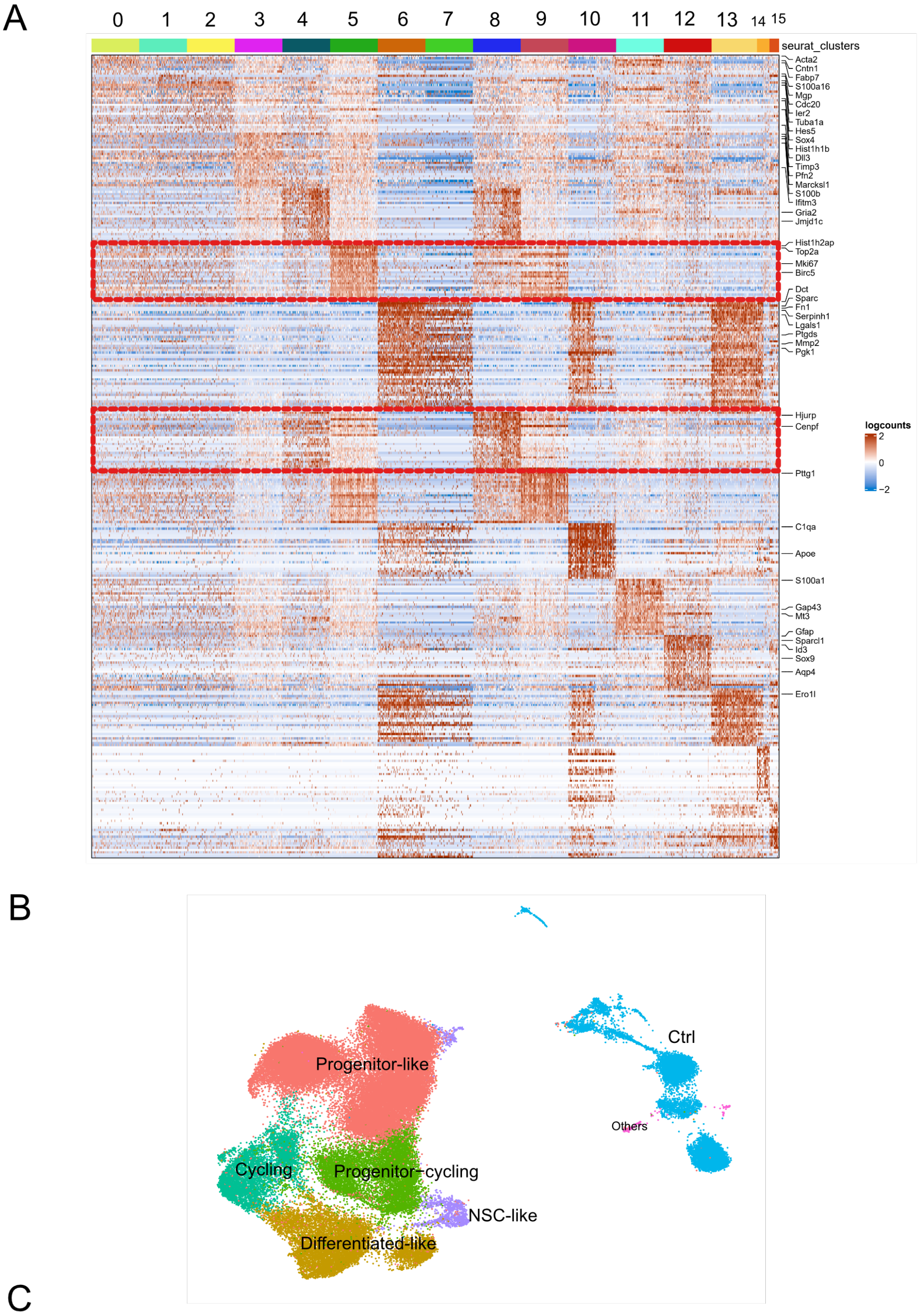

C

Class	Cluster(s)	Marker genes
Progenitor-like	0,1,2	Fabp7, Serpine2, Ppp1r14b, C1ql1,Gadd45g, Cdc20, Cenpf, Nfia, Nfib
Differentiated-like	3,11	Timp3, S100b , Sox4,S100a1, Gap43, Map2,Map1b
Progenitor-cycling	4,8	Top2a, Ascl1,Birc5, Rbbp4, Mcm6,Qk,Chd7
Cycling	5,9	Birc5, Top2a, Cenpf, Mki67, Cxcl10,
NSC-like	12	Gfap, Mt3. Apo3, Id3, Hes5, Sox9, Vcam1, Lrig1, Ntrk2, Sox2 ,Lifr
Ctrl	6,7,10,13	Ptgds,Plp1, Mbp, Sox10

Figure 17. Cluster-wise investigation

(A) Heatmap showing the top 5 marker genes in each cluster. Clusters were labeled at the top of the heatmap, while the marker genes were labeled on the right. Normalized expressions are shown. (B) UMAP depicts the major groups of tumor cells in the current scRNA-seq dataset. (C) Marker genes of each major group of cells.

3.3.7 Developmental relationship between KD clusters

In light of the resemblance of KD tumors to the development-like GB and the distinct expression pattern identified through cluster-wise marker expression analysis, I speculated that a certain degree of developmental relationship akin to NSC development should be present among the transcriptional clusters within the KD tumor cells. As such, I proceeded to interrogate the developmental states of the transcriptional clusters within KD tumor cells, focusing on what the KD-clusters most resemble along the lineage progression of NSCs. To this end, I took leverage of the gene signatures derived from a published scRNA-seq study on NSC lineage progression and the other one on the tumor cells [67, 206] and computed the AUCell scores of these neural/glial cell type gene signatures within the KD tumor cells in the single cell dataset.

Cluster 12 most closely resembles qNSC during the development of NSCs in adult mouse SVZ (**Figure 18A and B**). They also resemble radial glial (RG) cells and astrocytes. Still, they are unlikely to be differentiated as they express high levels of stem cell markers Sox2 and Nes (**Figure 18D**), consistent with previous reports suggesting the transcriptional similarity between qNSCs, RGCs and astrocytes during normal NSCs development [68]. Clusters 5 and 9 resemble activated neural stem cells (aNSCs) and transit amplifying cells, consistent with their higher expression of genes related to cell cycling. Clusters 3 and 11 seem to be situated at the end of this differentiation spectrum, with signatures close to the more differentiated neuroblasts, suggesting that these clusters could be differentiated cells. The rest of the clusters contribute the largest proportion of the KD tumor cells and seem to be in a rather progenitor cell-like state, as they resemble pri-OPC, with proliferative capacities [206]. KD clusters bear expressional resemblance to the development of the NSCs, in which both quiescent, activated/proliferative, and differentiated cell types were found.

Given the role of qNSCs in giving rise to different sub-lineages of cells along the NSC lineage progression, I reasoned that the general resemblance of Sox10-KD tumors to NSCs and progenitor cells could be the consequence of the *in vivo* activation of qNSC-like clusters (clusters 12). To test this, I worked closely with Dr. Charles Imbusch (Division of Applied Bioinformatics, German Cancer Research Center) to determine the differentiation dynamics of the KD cells using RNA velocity. In agreement with my analysis above, trajectory inference using RNA velocity analysis revealed qNSC-like cluster (cluster 12) is the potential root of the KD tumor cells (**Figure 18C**). Specifically, cluster 12 is at the non-proliferative G0/G1 phase but with the highest Sox2 and Nes expression levels.

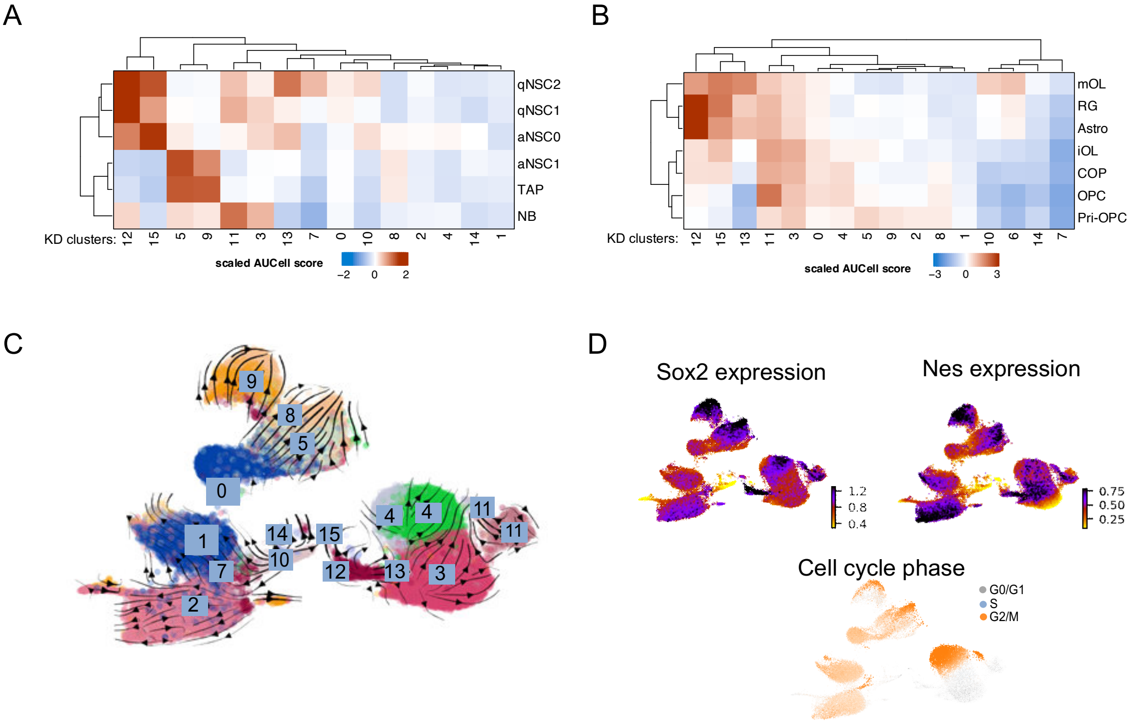

Figure 18. Resemblance of KD clusters to NSC development.

(A) Heatmap showing the scaled AUCell scores of gene signatures derived from Kalamakis et al [67]. (B) Heatmap showing the scales AUCell scores of gene signatures derived from Weng et al., Cell Stem Cell, 2020 [206] (C) UMAP visualization of (i) RNA velocity analysis of KD tumor cells. Cells are color-coded by the Seurat clusters in (A). The streamlines indicate the integrated paths that links to extrapolated future state. (D) Expression of Sox2 and Nestin and cell cycle phases of the KD tumor cells. Note that cluster 12 is at the non-proliferative state with the highest Sox2 and Nes expression.

3.4 Sox10-KD cells displayed quiescence stem cell features

Based on my findings in the previous sections, as well as the earlier findings regarding the roles of Sox10 in governing the onset of slow-growing phenotypes [188, 191], I speculated that the downregulation of Sox10 in GSCs would first lead to the emergence of a qNSC-like state, which, upon injection into the animals, becomes activated and yielded the more developmental-like tumors. In this section, I tested this hypothesis and examined whether KD cells exhibit qNSC-like features using mouse tumor cells and human patient-derived GSC models. I also interrogated the phenotypic consequences of the qNSC-like tumor, which contributes to the aggressive phenotypes in KD tumors.

3.4.1 Sox10-KD cells acquire quiescent stem cells' expressional and phenotypic features *in vitro*

I first tested whether the mGB1-KD cells showed the enrichment of the quiescent stem cell gene signature. GSEA using the gene signatures derived from the study from Kalamakis et al. [67], showed that the qNSC signature is significantly enriched in the KD tumor cells *in vitro* (NES = 1.64, adjusted p-value = 0.0016) (**Figure 19A**). Importantly, KD tumor cells *in vitro* also showed enrichment of gene signature of the qNSC-like cluster (cluster 12) in my scRNA-seq dataset. (NES = 1.41, adjusted p-value = 0.0014), further supporting the trajectory analysis that tumor cell development starts with this qNSC-like cluster (**Figure 19B**). I further performed qPCR and confirmed the upregulation of qNSC-related regulators and markers, including Sox9 [68] and Lrig1 [212], as well as Notch pathway target genes such as Hes5 and Nrarp [213] in the KD cells using two different shRNAs targeting non-overlapping regions of the Sox10 (hereafter known as KD#1 and KD#2 cells, respectively). **Figure 19C** shows that these Notch pathway genes were significantly upregulated in the KD cells versus the Ctrl cells. At the protein level, the upregulation of Sox9 and the Notch intracellular domain, a key effector protein of the Notch pathway, could be validated by Western blot (**Figure 19D**). Hence, the data here suggest that the KD cells have acquired a transcriptional program resembling quiescent stem cells prior to injection into the animals.

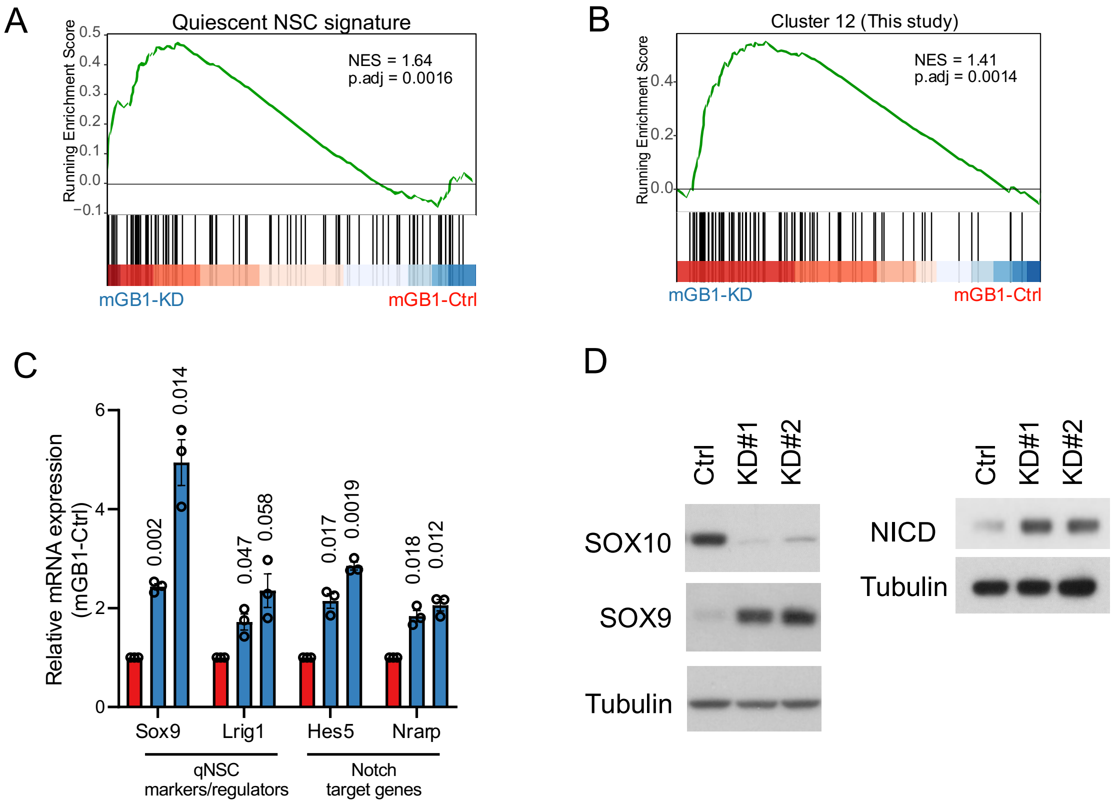

Figure 19. mGB1 cells acquire quiescent NSCs-like program upon downregulation of Sox10.

(A and B) GSEA plots showing the enrichment of (A) qNSC gene signature (Kalamakis et al., Cell, 2020) and (B) Gene signature of qNSC cluster (cluster 12) in this study (significantly upregulated genes in cluster 12 with log2 fold greater than 0.5 were taken) mGB1-KD cells vs. mGB1-Ctrl cells. Genes were pre-ranked by their log2 expression values in KD cells over Ctrl cells. NES = Normalized enrichment scores, p.adj = adjusted P values (C) Barplots are showing the qPCR quantification of relative expression of genes involved in qNSC markers and regulators (Sox9 and Lrig1) as well as Notch target genes (Hes5 and Nrarp). Data are represented as mean ± SEM expression level relative to mGB1-Ctrl from three experiments. P values were calculated using one-sample t-tests (compared to a mean value of 1). (D) Western blot analysis of the upregulation of Sox9 and NICD (Notch intracellular domain) in mGB1-KD. Tubulin was used as a loading control.

3.4.2 Phenotypic resemblance of Sox10-KD cells to qNSCs

Having shown that the KD cells acquired a transcriptional program related to qNSC, I interrogated whether Sox10-KD cells would display phenotypes resembling quiescent stem cells. To test this, I cultured the mGB1 Ctrl and KD tumor cells under reduced growth factor conditions (1 ng/ml of EGF and FGF2 vs. 20 ng/ml in standard culture conditions), after which the cells were recovered in standard culture conditions to test whether KD cells resumed proliferation. To distinguish G0 and G1 cells, I co-stained cells with DNA and Ki67, which is not expressed in G0 or early G1 cells [214], and gated on the DNA-low/Ki67-negative quadrant Q4.

As shown in **Figure 20**, fewer than 10% of cells were in G0 phase in both Ctrl and KD cells, while the majority (>80%; Q1+Q2) expressed the Ki67 proliferation marker under standard culture conditions. When cells were cultured in low-GF conditions, both cell types became less proliferative, as evidenced by the lower percentage of cells in the cycling non-G0/G1 phase (**Figure 20A and B**). However, more Ctrl cells were arrested at G1 phase (DNA-low/Ki67-positive quadrant), whereas KD cells preferentially exited the cell cycle and remained at the G0 phase (DNA-low/Ki67-negative quadrant). Importantly, when growth factors were re-introduced to the culture medium, they re-entered the cell cycle and resumed proliferation, precluding the possibility that these cells were senescent or terminally differentiated (**Figure 20C**).

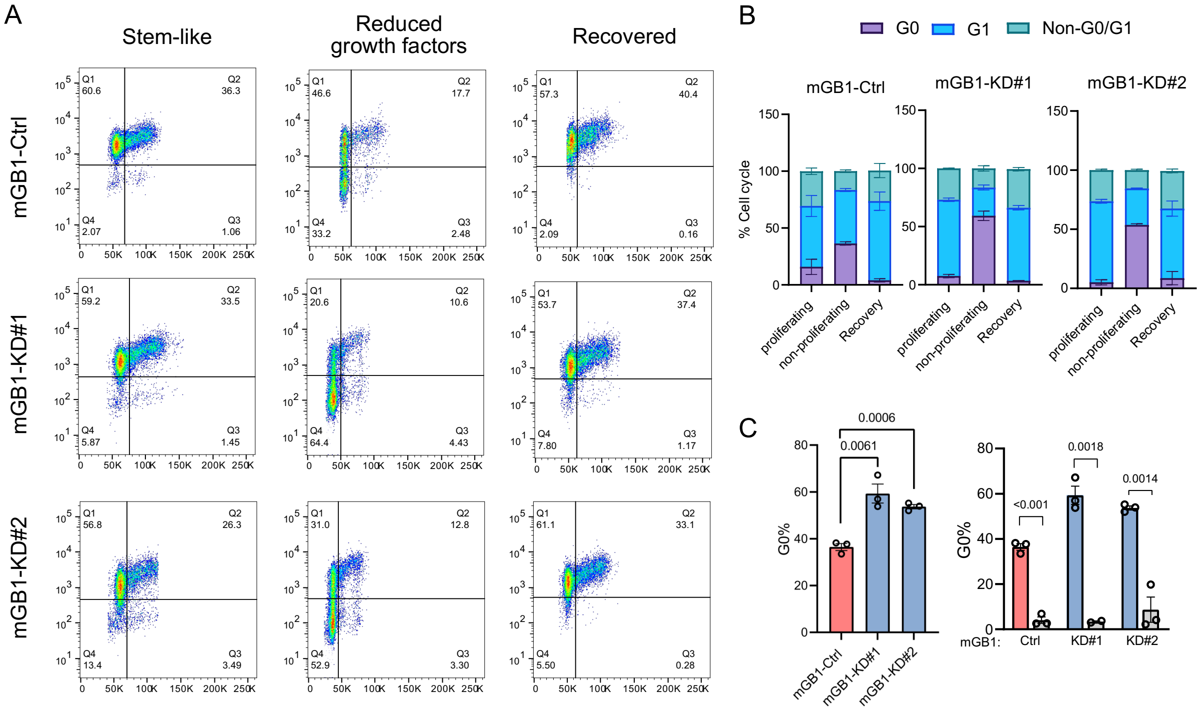

Figure 20. Sox10-KD mouse cells displayed an increased abundance of quiescent G0 phase cells under non-proliferating conditions.

(A) Scatter plots showing the cell cycle distribution of mGB1-Ctrl and KD cells (KD#1 and KD#2) under stem-like conditions, reduced growth factor conditions for 7 days and recovered conditions. To distinguish between G0 and G1 phases, Ki67 was co-stained with DNA dye FxCycle 450; hence G0 phase cells are marked by DNA-low (x-axes) and Ki67-negative (y axes). (B) Bar plots showing the distribution of cell cycle of mGB1-Ctrl and KD cells in G0, G1 and non-G0/G1 phases (G2/S/M) phases. (C) Barplots comparing the abundance of G0 phase cells under reduced growth factor conditions (left) and upon recovery with full growth factors (right). The percentages were reported as mean ± SEM from three experiments. P values were computed using two-tailed unpaired T-tests between Ctrl and KD cells.

To further confirm the findings using a positive marker of quiescence, I co-stained cells with Sox9 and p27 (a commonly used quiescent cell marker [215, 216]) to mark quiescent/dormant cells with NSC features. Immunofluorescence analysis revealed an increase in the abundance of Sox9 and p27 double-positive cells in KD cells under reduced growth factor culture conditions. Collectively, the data presented here suggest that *SOX10*-low GSCs enter a quiescent neural stem cell (qNSC)-like state. This also supports the findings of RNA velocity analysis in the previous section that the overall resemblance stems from a group of qNSC-like tumor cells.

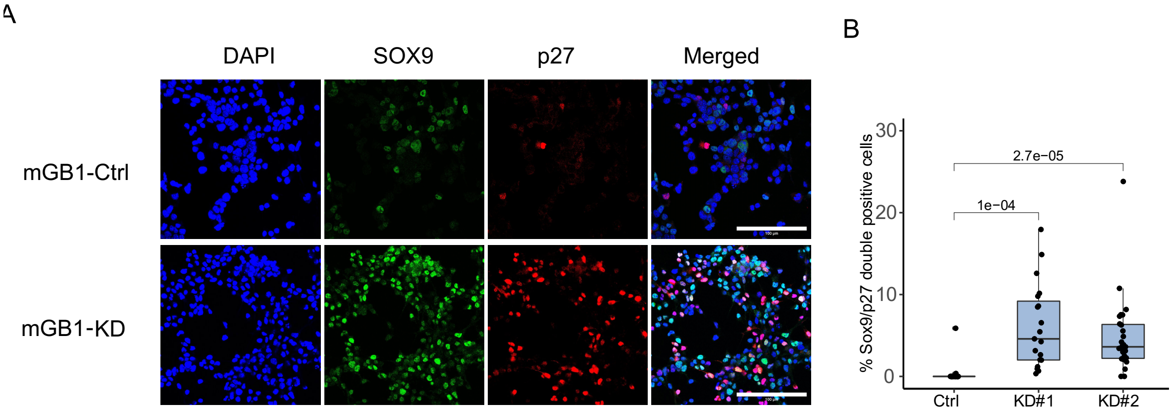

Figure 21. Sox10-KD mouse cells displayed an increased abundance of Sox9 and p27 double-positive cells under non-proliferating conditions.

(A) Representative immunofluorescence images of mGB1-Ctrl and KD cells (KD#1 and KD#2) stained with Sox9 and p27. Scale bars = 100 µm. (B) Boxplots show the quantification results of the percentages of Sox9 and p27 double-positive cells. Each dot represents the percentage of cells from an image (n = 16 images). Reported in the boxes are the median ± interquartile range. P values were computed using two-tailed unpaired T-tests.

3.4.3 Phenotypic consequences of qNSC-features

The brain presents a particularly hostile tumor microenvironment for the survival of tumor cells, including the lack of nutrients, niche factors promoting the differentiation of stem-like tumor cells, and immune surveillance programs that eliminate tumor cells. Tumor cell quiescence has been shown to be correlated with better endurance in the TME [217, 218]. In light of this, I examined the phenotypic consequences of qNSC-like tumor cells, which would be advantageous to tumor development.

3.4.3.1 Reduced differentiation

Single-cell data indicated that the Ctrl tumor cells were more differentiated, while KD tumor cells have more pronounced stem cell properties. I speculated that such phenotypic differences could be attributed to the fact that as KD tumor cells enter a quiescent state, they could better preserve their stem cell properties in response to differentiation. In normal NSCs, this is achieved through Notch pathway activation, which prevents differentiation processes. To test this, I treated Ctrl and KD cells with 10% FBS, a commonly used condition to differentiate NSCs. As **Figure 22A** shows, after 7 days of treatment in FBS, Ctrl cells showed differentiated morphologies, whereas KD cells remained free-floating spheres, suggesting KD cells retained self-renewal properties. Consistently, Western blotting showed that Sox2 expression decreased in FBS-treated Ctrl tumor cells but remained high in KD cells treated with FBS, compared to its expression in cells cultured under serum-free conditions (**Figure 22B**). Collectively, this differentiation experiment showed that qNSC-like KD cells preserve their self-renewal potentials in the face of differentiation signals, consistent with the normal functions of qNSC in maintaining the pool of cells with stem cell properties.

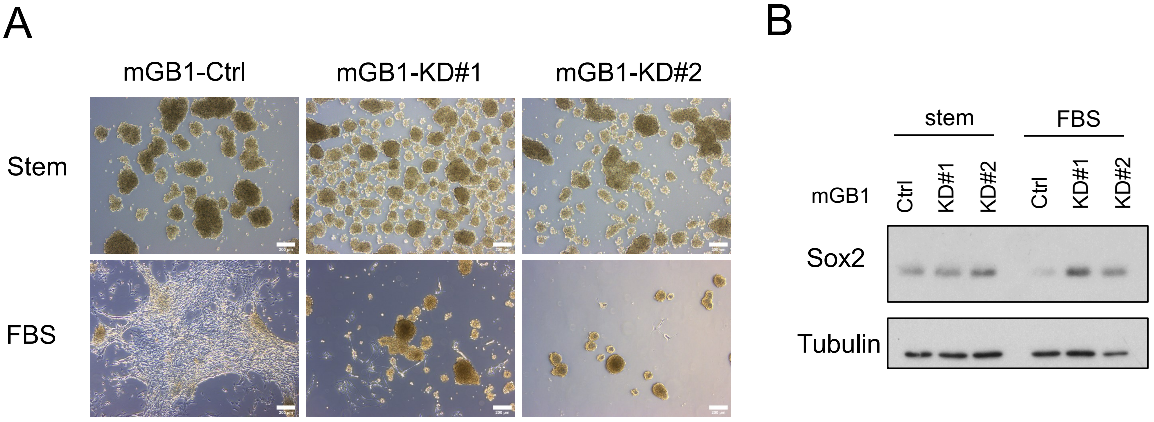

Figure 22. Sox10-KD tumor cells are resistant to differentiation by serum.

(A) Representative brightfield images of mGB1-Ctrl and KD cells (KD#1 and KD#2) cultured in stem cell conditions (top) or 10% fetal bovine serum (FBS) for 7 days to induce differentiation (below). Scale bars = 200 µm. (B) Western blotting of the protein expression of Sox2, a stem and progenitor cell marker, in mGB1-Ctrl and KD cells cultured under stem or FBS conditions. Tubulin was used as the loading control.

3.4.3.2 Immunological quiet state via lowering of MHC-I molecules expression

Another facet pertinent to the development of full-blown tumors is their ability to evade immune surveillance by reducing their antigen presentation level, which has been previously demonstrated in normal quiescent cells and cancer stem cells [219], As shown in **Figure 23**, KD cells have a lower mRNA expression of MHC-I molecules H2-D1 and H2-K1 than Ctrl cells, consistent with the scRNA-seq data that KD tumors have a lower expression of MHC-I molecules (**Figure 23A**). To further validate the differences between the expression of the MHC-I molecules at the protein level, I analyzed the expression of the MHC-I molecules of Ctrl and KD cells in stem-cell and differentiating conditions using flow cytometry. While the expression levels of H2-D1 and H2-K1 were not different between Ctrl and KD cells at the stem cell condition, KD cells had lower MHC-I levels compared with Ctrl cells when grown in differentiation-inducing conditions (**Figure 23B**). This result is consistent with the immune cell analyses of the scRNA-seq data, in which less pronounced immune surveillance occurred within the KD tumors (Supplementary information). However, the extent to which this observation leads to less frequent T cell attacks is beyond the scope of this thesis and hence remains to be experimentally validated.

Taken together, by entering a qNSC-like cellular state via the downregulation of Sox10 expression in tumor cells, they were more capable of withstanding the harsh TME lacking differentiation-inducing TME by preserving their self-renewal potentials while keeping themselves in a relatively immunologically quiet state by lowering their antigen presentation, potentially leading to the escape of immune surveillance.

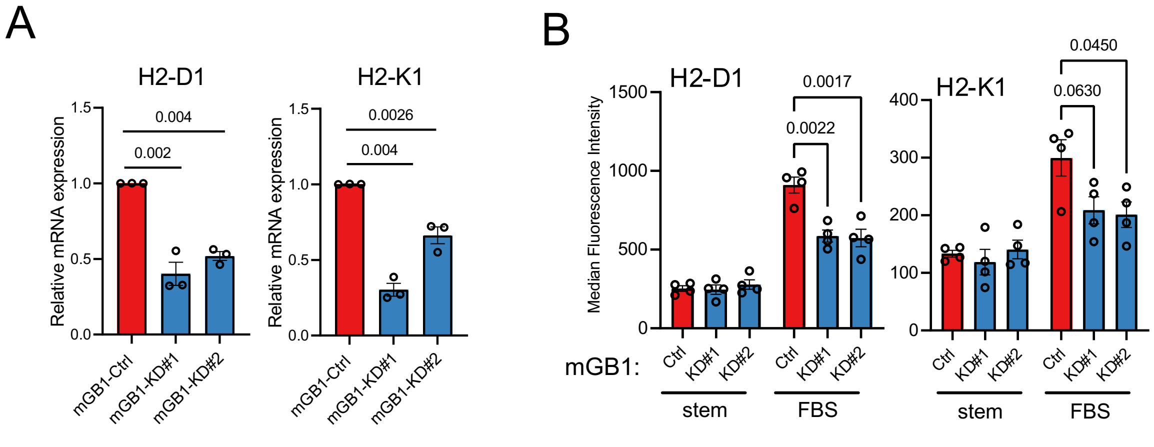

Figure 23. Lower expression of antigen-presenting MHC-I molecules in KD cells upon differentiation cues.

(A) Barplots showing the qPCR quantification of relative expression of MHC-I molecules (H2-D1 and H2-K1) in mGB1-Ctrl and KD cells (KD#1 and KD#2). Expression values are represented as mean ± SEM expression level relative to mGB1-Ctrl from three experiments. P values were calculated using One-sample t-tests (compared to a mean value of 1). (B) Bar plots show the median fluorescence intensity of H2-D1 (left) and H2-K1 (right) in Ctrl and KD cells under normal stem cell or differentiation conditions by 10% FBS. Data are represented as mean ± SEM median fluorescence intensity from four experiments. P values were calculated using two-tailed unpaired t-tests.

3.4.4 Downregulation of *SOX10* in human GSC

I further examined the effects of *SOX10*-KD in human GSCs and interrogated whether the quiescence stem cell phenotypes observed in mouse GB cells also occur in human GSCs. I initially tried using shRNA-mediated KD in the human GSCs. However, only one shRNA construct substantially downregulated *SOX10* expression (data not shown). Therefore, I established the CRISPR-interference (CRISPRi) KD systems in patient-derived, *SOX10*-high human GSC lines, NCH421k, NCH441 and NCH644. Briefly, these GSCs were first stably transduced with dead Cas9 (dCas9) linked to a transcription repressor Krüppel-associated box domain (KRAB). Afterward, these dCas9-expressing cells were further transduced with sgRNA constructs targeting *SOX10* (hereafter known as sg1-3) so that the transcriptional repressor could be recruited to the region to silence *SOX10* expression. Efficient KD was achieved in all three cell lines with different sgRNA constructs targeting different regions of *SOX10* at both the mRNA and protein levels (**Figure 24B**).

In agreement with my findings in mouse tumor cells, *SOX10* downregulation significantly upregulates qNSC regulators such as *SOX9* and *LRIG1* and Notch pathway target genes *HES5* and *NRARP* in human GSCs NCH441 and NCH644 (**Figure 24A**). Consistently, I observed the upregulation of *SOX9* and p27 at the protein level upon the downregulation of *SOX10* in these human GSCs (**Figure 24B**). Hence, the results here clearly indicate that human GSCs similarly initiate a qNSC-like transcriptional program upon the reduction of *SOX10* expression in tumor cells.

I also performed similar experiments in mouse tumor cells to confirm the phenotypic resemblance of the KD cells to quiescent stem cells. Cell cycle analysis using co-staining of DNA and Ki67 revealed their departure from the cell cycle to the G0 phase (DNA-low/Ki67-neg) upon *SOX10* downregulation in these GSCs (**Figure 24C**). The KD cells also had a higher abundance of *SOX9*/p27 double-positive cells, indicating that they entered a quiescent or dormant cellular state with NSC features (**Figure 24D**).

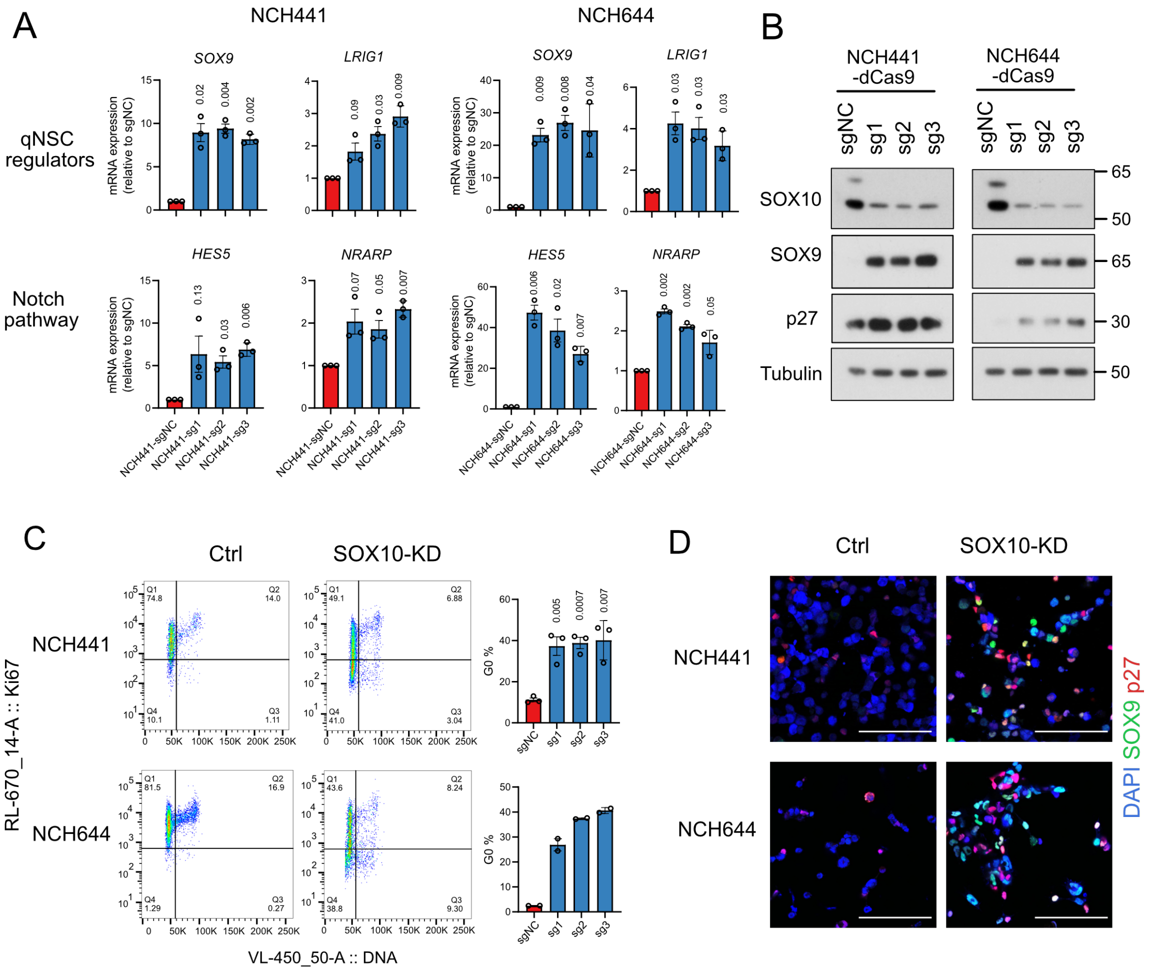

Figure 24. Downregulation of *SOX10* in human GSCs results in quiescent stem cell-like phenotypes.

(A) Barplots showing the qPCR quantification of relative expression of genes involved in qNSC markers and regulators (*SOX9* and *LRIG1*) as well as Notch target genes (*HES5* and *NRARP*) in human GSCs. Data are represented as mean ± SEM expression level relative to mGB1-Ctrl from three experiments. P values were calculated using one-sample t-tests (compared to a mean value of 1). (B) Western blotting of the upregulation of *SOX9* and p27 in Ctrl cells (sgNC) and KD cells (transduced with sg1-3) in *SOX10*-high NCH441 and NCH644 cells. Molecular sizes of targets (in KDa) are indicated on the right. (C) Scatter plots showing the cell cycle distribution of NCH441 and NCH644 Ctrl and KD cells. To distinguish between G0 and G1 phases, Ki67 was co-stained with DNA dye FxCycle 450; hence G0 phase cells are marked by DNA-low (x-axes) and Ki67-negative (y axes). The bar plots on the right show the abundance of G0 phase. The percentages were reported as mean ± SEM from two to three experiments. P values were computed using two-tailed unpaired t-tests between Ctrl and KD cells. (D) Representative immunofluorescence images of NCH441 and NCH644 Ctrl and KD cells co-stained with SOX9 and p27. Scale bars = 100 µm.

To determine the tumorigenic potential of human KD cells, I co-cultured NCH644-Ctrl and KD cells with cerebral organoids derived from human-induced pluripotent stem cells (iPSCs). While Ctrl and KD cells could invade and proliferate in the cerebral organoids, the KD cells expanded much more rapidly than Ctrl tumor cells (**Figure 25A)**. Upon harvesting and dissociating the cerebral organoids after 14 days of co-culture, tumor load was assessed based on the percentage of GFP-expressing tumor cells within the organoids, revealing a higher tumor load of the cerebral organoids co-cultured with KD tumor cells (**Figure 25B**). In addition, the tumor cells isolated from the GLICO models also had a higher sphering forming ability and higher SOX2 level compared to control cells (**Figure 25C).** These data are consistent with our observations in the syngeneic mouse model.

A *Proliferation within cerebral organoids*

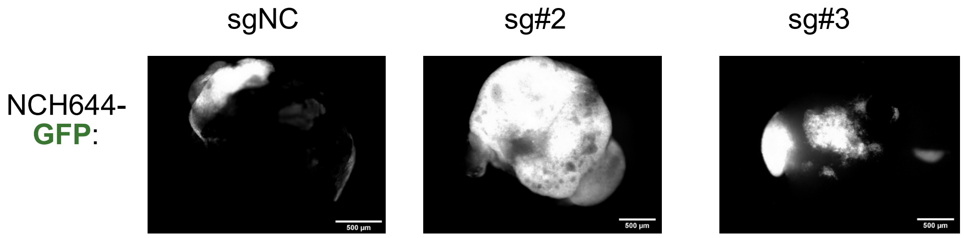

B *Tumor load measurement by flow cytometry*

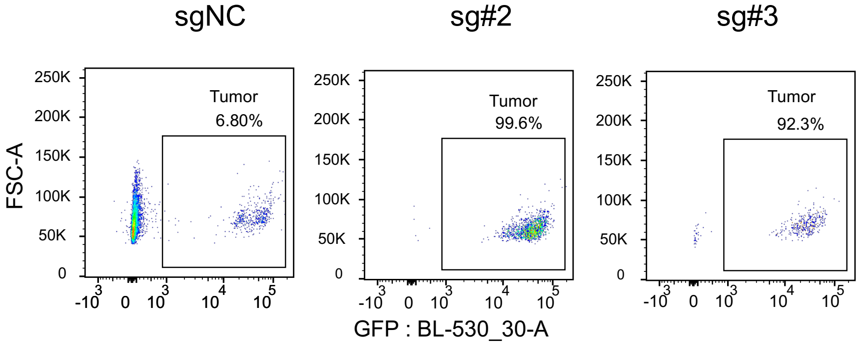

C *Sphere-forming abilities of dissociated tumor cells*

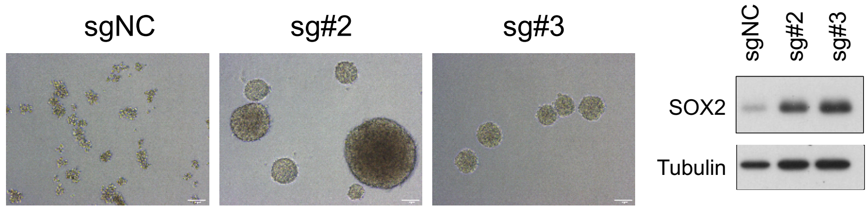

Figure 25. Tumorigenicity of KD-GSCs in cerebral organoid co-culture models (GLICO).

(A) Stereoscopic fluorescence images showing the growth of Ctrl cells (sgNC) and KD cells (sg#2 and sg#3) in iPSC-induced cerebral organoids on day 14 after co-culture. Scale bar = 500 µm. (B) Flow cytometry analysis of the tumor load in the cerebral organoids, represented by the percentage of GFP-positive tumor cells. (C) Brightfield images of the tumor cells (NCH644-sgNC, sg#2, and sg#3) dissociated from the organoids. The dissociated cells were cultured in a stem-cell medium and allowed recovery for 3 days. Western blotting of the protein expression of *SOX2* in the dissociated cells. Tubulin was used as the loading control.

3.5 *SOX10*-mediated cell fate changes in the context of treatment pressure

In the context of normal and neoplastic NSC development [82, 98, 131, 220], it has been demonstrated that anti-proliferative standard therapy such as temozolomide (TMZ) treatment preferentially removes cycling cells while sparing stem cells with quiescence features. However, these therapy-resistant quiescent cells re-seed tumors upon recurrence. Additionally, Sox10 expression has been shown to be downregulated upon irradiation in a GB mouse model [194] and upon targeted therapy in melanoma [188, 189]. Hence, I speculated that therapy would induce similar phenotypic adaptation in tumor cells. In this section, I further examined the effects of treatment pressure on the cell states of tumor cells. Specifically, I investigated whether treatment pressure imposed by TMZ would downregulate *SOX10* expression in GB cells, leading to the emergence of quiescent stem-cells like phenotypes. Furthermore, using *in vitro* models and analyzing relevant published datasets, I addressed whether quiescent stem cells play a role in tumor recurrence.

3.5.1 Treatment pressure by TMZ downregulates *SOX10* expression in human GSCs

I first examined whether TMZ treatment would cause the downregulation of *SOX10* expression in human BTSCs. To this end, I treated *SOX10*-high, *MGMT* promoter methylated NCH421k and NCH441 cells with 25 µM and 100 µM of TMZ for 7 days. Western blotting showed that TMZ treatment resulted in the consistent downregulation of *SOX10* expression and concurrent upregulation of *SOX9* (**Figure 26A)**, analogous to the transcriptional alterations observed upon *SOX10*-KD in human BTSCs (Section 3.4.1). Then, I further tested the effect of TMZ treatment using the GLICO model described in the previous section. Briefly, GFP and luciferase dual-labeled NCH644 cells were co-cultured with iPSC-derived cerebral organoid models, wherein tumor growth was monitored by bioluminescence imaging. NCH644 cells were chosen here because I have shown in Section 3.4.4 that these cells could invade and proliferate within the organoids (**Figure 25**). Once the tumor cells started growing in the organoids (6 days after co-culture), TMZ was added to the GLICO models. TMZ treatment at 100 µM significantly reduced the proliferation of NCH644 cells in the organoids **(Figure 26B, left)**. Interestingly, tumor cells seemed to resume their proliferation toward the end of the treatment. When the DMSO-treated GLICOs reached the maximal tumor size, both treated and untreated GLICOs were dissociated, and the expression of *SOX10* of tumor cells (viable GFP-pos cells) was analyzed by flow cytometry, revealing lower expression of *SOX10* on the tumor cells in the TMZ-treated organoids (**Figure 26B, right)**. Independently, the downregulation of Sox10 expression upon TMZ treatment was also observed in an RCAS (Replication-Competent Avian sarcoma-leukosis virus long terminal repeat with Splice acceptor) spontaneous mouse GB model driven by Pdgfb, and Akt [112], which was further validated by immunohistochemistry, lending additional support to treatment-induced downregulation of *SOX10* in tumor cells occurs in physiologically relevant models.

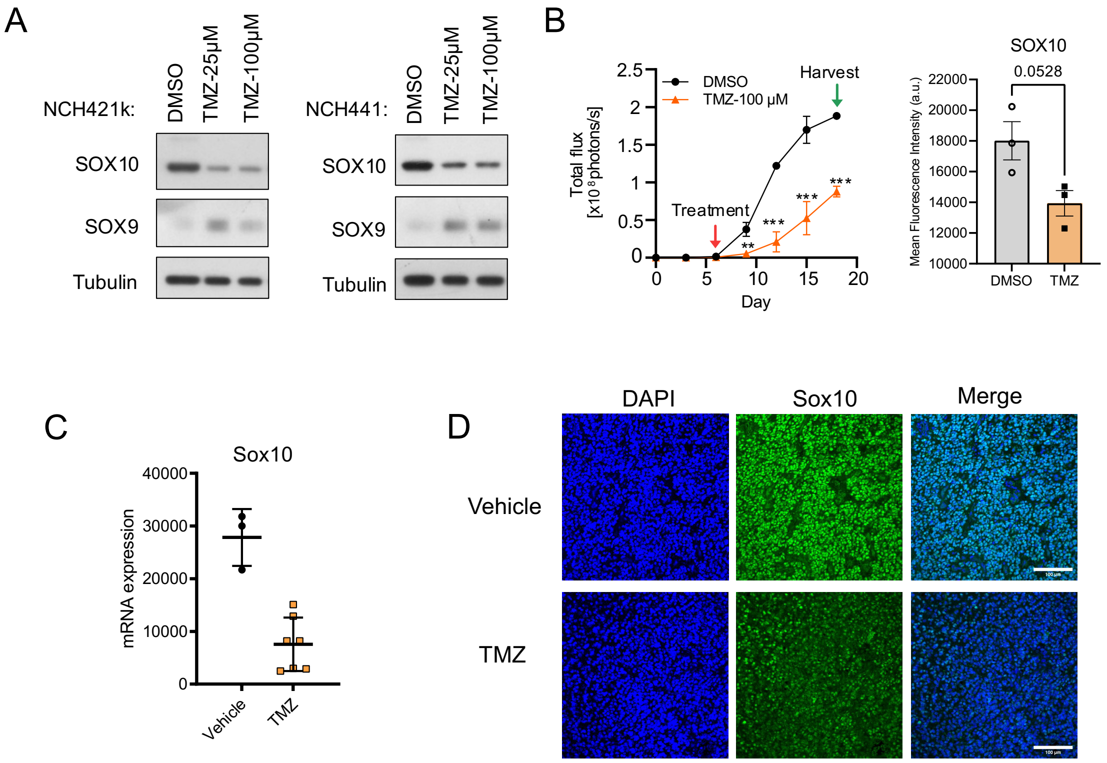

Figure 26. Treatment pressure by TMZ downregulates *SOX10* expression in different pre-clinical models.

(A) Western blotting showing short-term treatment pressure (indicated treatments for 7 days) on *SOX10* and *SOX9* expression in NCH421k and NCH441 cells. (B) Therapy-induced reduction of *SOX10* expression on tumor cells was further validated using the GLICO model by co-culturing GFP and luciferase dual-labeled NCH644 cells in iPSC-induced cerebral organoids. Tumor cell growth in the organoids was monitored by bioluminescence imaging every 3 days. The line graph on the left depicts the bioluminescence signals (in terms of photon influx per second) during the co-culture experiment. Treatment (DMSO or 100 µM TMZ) was given on day 6, while organoids were harvested and analyzed for *SOX10* expression on day 18. The bar graph on the right shows the mean fluorescence intensities of *SOX10* expression on tumor cells (viable GFP-positive cells) as analyzed by flow cytometry. Data were reported as mean ± SEM from three organoids. P value was computed with a two-tailed unpaired T-test. (C) Normalized read counts of Sox10 in vehicle (n = 3) and TMZ-treated (n = 7, 100 mg/kg of TMZ, for 5 consecutive days) Pdgfb/Akt RCAS spontaneous GB mouse model from an unpublished study from Dr. H.K. Liu's group. (D) Tumor sections were kindly provided by Dr. Liu's group, and representative immunofluorescence staining of *SOX10* and vehicle and TMZ-treated mice were shown. Scale bar = 100 µm.

Intriguingly, I observed that the treatment-induced downregulation of Sox10 seems to be related to the activation of the TGF-beta pathway. As the Western blotting in **Figure 27** shows, when tumor cells were treated with 2 ng/ml to 10 ng/ml of recombinant TGFβ1 for 5 days, a substantial reduction in *SOX10* expression was observed in different *SOX10*-high tumor cell lines. This TGFβ1-induced downregulation of *SOX10* is consistent across the cell lines I have tested, including both human and mouse GB cell lines LN229, ZH487, and mGB1, as well as melanoma cell line A375. TGFβ1 suppresses *SOX10* expression in neural crest stem cells and has been implicated in treatment [221]. Hence, the present data indicate that TMZ-induced *SOX10* downregulation may be linked to the therapy-induced release of TGFβ1 from either tumor or stromal cells. More importantly, it also demonstrates that the expression of *SOX10* in tumor cells can be controlled by extracellular cues, consistent with the observations in normal settings [221, 222]

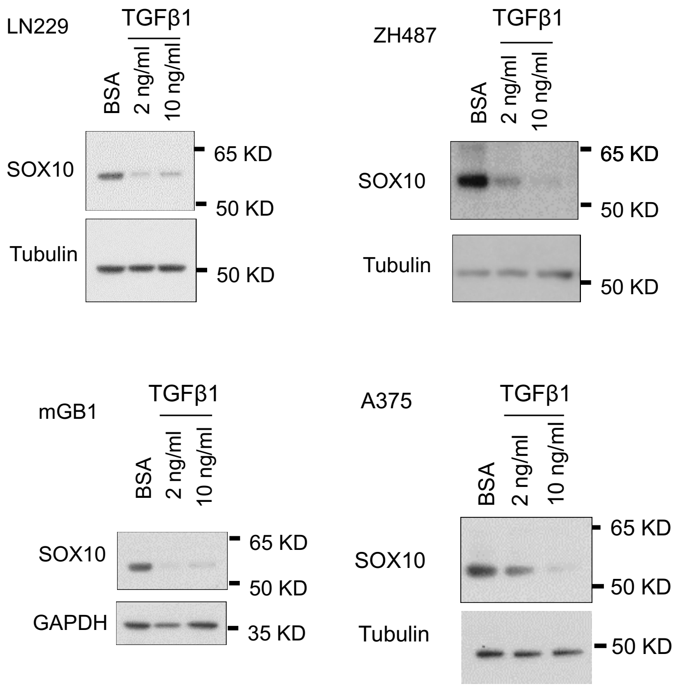

Figure 27. Activation of TGFβ pathway downregulates SOX10 expression in tumor cells.

Representative Western blotting of the effects of recombinant TGFβ1 treatment (2 ng/ml to 10 ng/ml for 5 days) on the SOX10 expression in tumor cells. The cell lines tested here included human GB cells (LN229 and ZH487), mouse GB cells (mGB1) as well as human melanoma cells (A375).

3.5.2 *SOX10*-low tumor cells are TMZ resistant

Having shown that tumor cells downregulate *SOX10* expression upon TMZ treatment pressure, I next asked whether the *SOX10*-low cells would display increased resistance to TMZ treatment. To address this, I tested the sensitivity of the KD cells to TMZ compared to Ctrl cells. As shown in **Figure 28**, KD cells showed increased TMZ resistance in mGB1 cells and in NCH421k and NCH441 cells. Coupled with the quiescence stem cell phenotypes observed in the KD cells in the last section, I propose that TMZ treatment results in the downregulation of *SOX10* in the tumor cells, thereby driving them toward a slow-cycling, drug-resistant state.

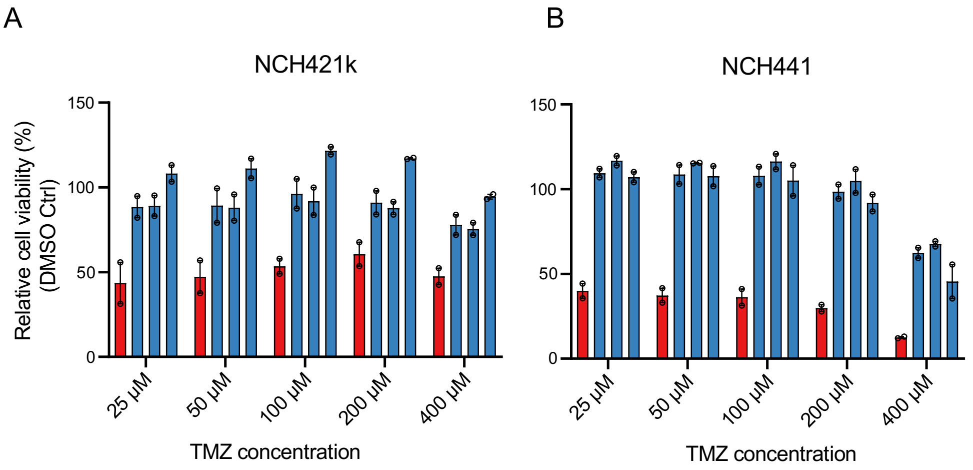

Figure 28. *SOX10*-KD cells are more resistant to TMZ treatment.
Bar plots show the relative cell viability of Ctrl (red) and KD cells (blue) of (A) NCH421k and (B) NCH441 treated with varying concentrations of TMZ for 72 h. Data are reported as mean ± SEM from two experiments.

3.5.3 Long-term treatment of TMZ in GSCs

It has been well-established that in response to standard treatment, tumor cells can enter the drug-resistant quiescence state and later re-seed the tumors when the therapeutic pressure is lifted. As a result, recurrent tumors are often more aggressive and resistant to therapy. As the next step to understand the phenotypic transition accompanied by therapy-induced *SOX10* downregulation, I further investigated the effect of long-term TMZ treatment on the tumor cells, focusing on the phenotypic switch upon release of treatment pressure.

NCH421k and NCH441 cells were treated continuously with 100 µM TMZ, a more clinically relevant concentration (corresponding to the maximal cumulative plasma concentration of TMZ in these studies [223-225]) for up to 35 days. Consistent with their *MGMT* promoter methylation status, both GSC lines were sensitive to TMZ treatment, and their proliferation was consistently inhibited during the treatment period (**Figure 29A**). Against the backdrop of suppressed proliferation, small non-cycling or slow-cycling spheres emerged from TMZ-treated NCH421k and NCH441, suggesting that a subpopulation of cells survived continuous exposure to TMZ and these cells can self-renew and are TMZ-resistant (**Figure 29B**). Upon the withdrawal of TMZ, these surviving cells regrew, further confirming that they were not permanently arrested. In line with this, I observed up-regulation of *SOX9*, the master regulator of qNSC and other dormant cancer stem cells [68] and HES5 (**Figure 29C and D**), the direct target gene of the Notch pathway, which is critical for maintaining the state of qNSC. Collectively, these data suggest that the resistant/tolerant cells showed qNSC features, and these cells can resume proliferation after TMZ withdrawal.

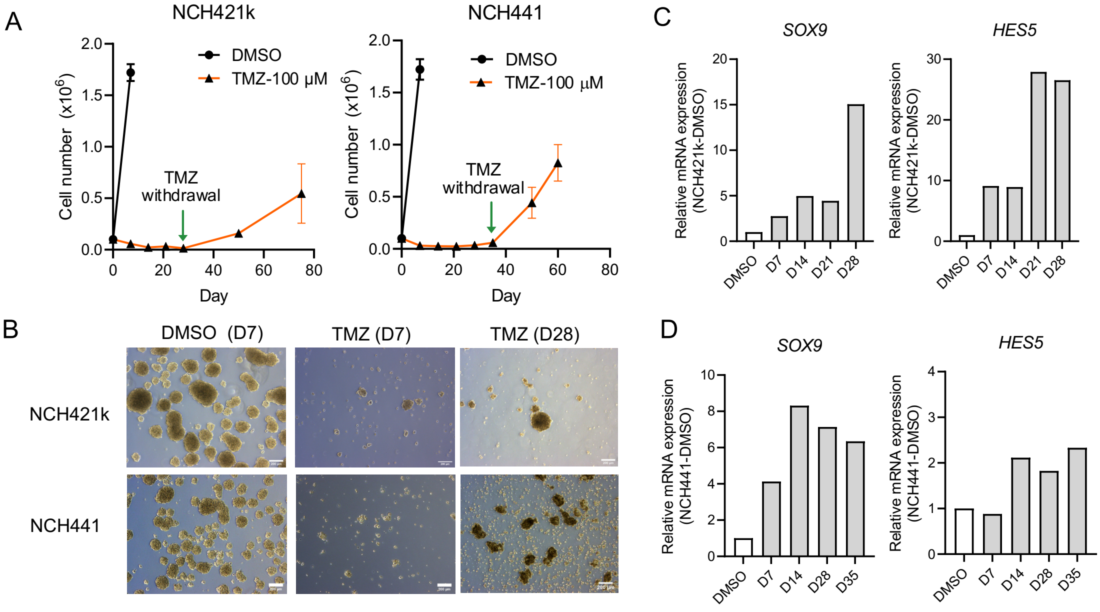

Figure 29. Long-Term TMZ treatment in human GSCs.

(A) Growth curves showing the number of cells in DMSO- and TMZ-treated NCH421k (left) and NCH441 (right). In each condition, 100,000 cells were seeded, and cell numbers were counted weekly, with TMZ withdrawn at the indicated timepoints. For DMSO-treated cells, cells reached confluency after 7 days; hence, cell numbers were not determined afterward. Mean +/− SEM from two experiments. (B) Representative brightfield images showing the morphologies of DMSO-treated and TMZ-treated NCH421k (top) and NCH441 (bottom) at D7 and D28. Note the emergence of small, slow-cycling spheres upon continuous TMZ treatment. (C and D) Bar plots show qPCR quantifications of the expression of quiescent stem cell markers *SOX9* and Notch-responsive gene HES5 over the course of long-term TMZ treatment in (C) NCH421k and (D) NCH441. Mean values from technical duplicates of one experiment are shown.

As **Figure 30A** shows, the recovered cells maintained the downregulation of *SOX10* and the upregulation of *SOX9*. Interestingly, I observed the recovered cells grew slower than their parental counterparts, even weeks after recovery (**Figure 30B**). When I re-challenged the recovered cells with TMZ, they showed significantly lower sensitivity to TMZ than the parental cells (**Figure 30C)**. *MGMT* was not re-expressed in the recovered cells (tested by qPCR, with the Ct values of *MGMT* transcript in parental and recovered cells above 30), suggesting that the decreased sensitivity to TMZ is unlikely mediated by a genetic mechanism. Double immunostaining of *SOX9* and p27 in the recovered cells also showed that they harbored more *SOX9*/p27 double-positive cells (**Figure 30D and E**), suggesting that the qNSC-like tumor cells that emerged upon TMZ treatment were maintained in the recovered cells. Taken together, GSCs recovered cells can resume proliferation showed quiescent stem cell features, which could be attributed to the downregulation of *SOX10* and the upregulation of *SOX9* in tumor cells upon therapeutic pressure.

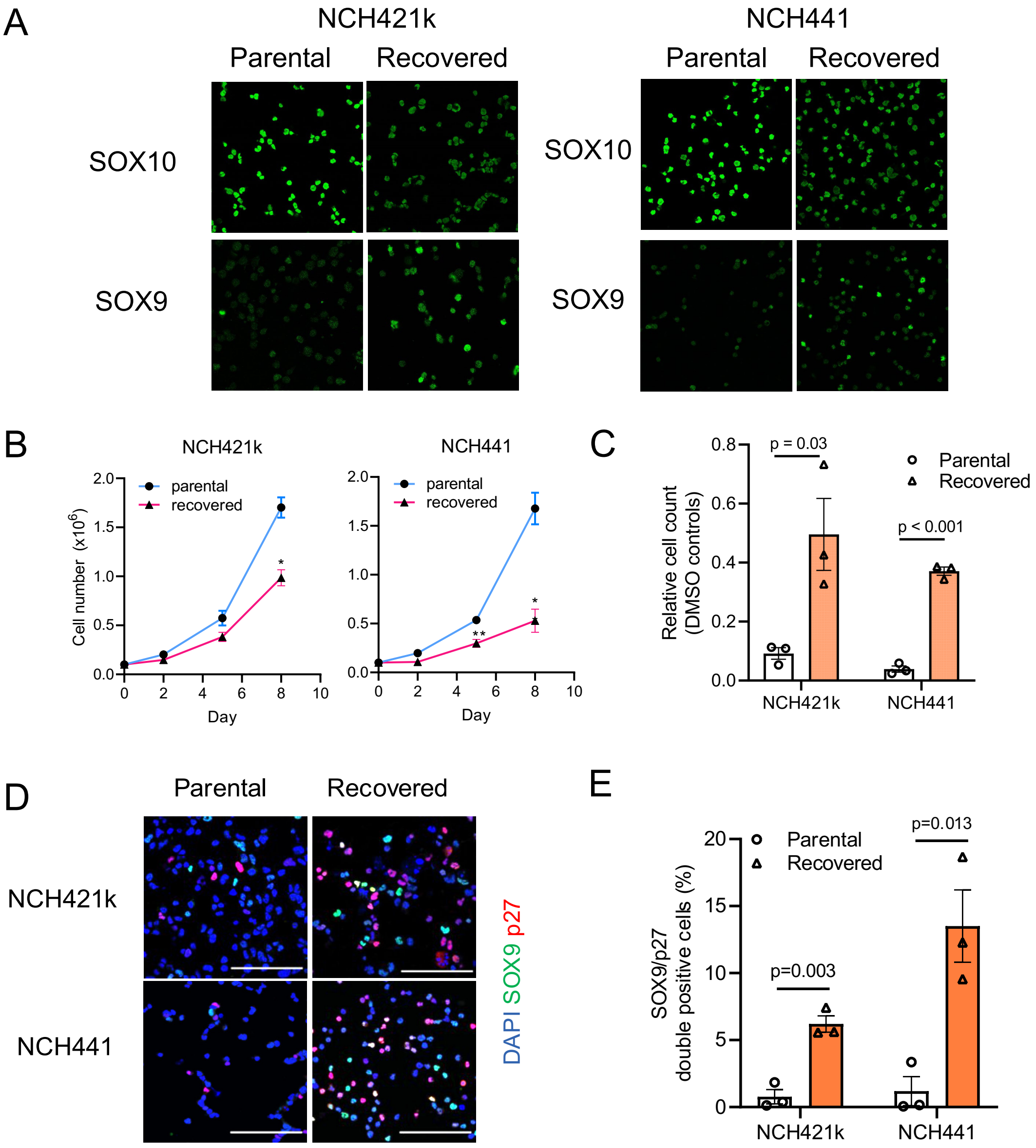

Figure 30. Human GSCs recovered from long-term TMZ treatment harbored qNSC-like tumor cells.

(A) Immunofluorescence analysis of *SOX10* and *SOX9* expression in NCH421k and NCH441 parental cells, as well as cells recovered from continuous treatment with 100 µM of TMZ. (B) Growth curves of NCH421k and NCH441 parental and recovered cells. Mean +/− SEM from three experiments. P values were calculated using a two-tailed unpaired t-test. * P < 0.05, ** P <0.01 (C) Bar chart showing NCH421k and NCH441 parental cell numbers and recovered cells in response to a 7-day treatment with 100 µM of TMZ. Cell counts were normalized to their respective DMSO controls. Mean +/− SEM from three experiments. P values were calculated using a two-tailed unpaired t-test. (D) Immunofluorescence analysis of co-staining Sox9 and p27 in NCH421k and NCH441 parental and recovered cells. Scale bar: 100 µm. (E) Quantification of *SOX9*/p27 double positive cells. Mean +/− SEM from three experiments, 5 fields of views were taken from each experiment. p values were calculated using Two-tailed students' T-tests.

3.5.4 Clinical relevance of *SOX10* downregulation in recurrent GBs

The data above indicated that treatment pressure from TMZ causes the reduced expression of *SOX10* in tumor cells, resulting in the acquisition of a quiescent stem cell-like phenotype. Upon the withdrawal of TMZ, these quiescent stem cells recovered their proliferation and gave rise to drug-resistant tumor cells, potentially resulting from a subpopulation of tumor cells, which remained in their quiescence states. To understand the clinical relevance of the findings above, I queried our own and a published patient dataset of matched primary and recurrent tumors, focusing on the expressional changes of *SOX10* and quiescent stem cell features upon GB recurrence.

I first examined the RNA-seq data from matched primary and recurrent GB pairs from the RNA-seq data from our laboratory (HIPO043 [27], n = 37 pairs) and from the most recent updates of the Glioma Longitudinal Analysis (GLASS) consortium [196] (n = 114 pairs of IDH-WT GB samples). As shown, while the expression of *SOX10* between matched primary and recurrent pairs was not significantly different when the entirety of both cohorts was considered (**Figure 31A and C, left**), *SOX10*-high primary GB samples (top quartiles of *SOX10* expression values, n = 10 pairs and n = 29 pairs, respectively), representative of RTK1/Type 2 GB, did show a significant reduction in *SOX10* expression upon recurrence (p = 0.0645 and p = 0.00515, Wilcoxon's paired T-tests) (**Figure 31A and C, right**). Specifically, 7 out of 10 (70%) and 21 out of 29 (72.4%) of these *SOX10*-high primary GB samples downregulate *SOX10* in their matched recurrent GB samples. This reduction of *SOX10* downregulation can also be validated by immunohistochemistry in patient samples (**Figure 31G**). Additionally, ssGSEA using qNSC1 and qNSC2 as gene signatures showed that recurrent GB samples tended to have higher ssGSEA scores for these quiescent stem cell signatures, consistent with my *in vitro* observations that recovered tumor cells showed enhanced qNSC-like features (**Figure 31B and D**).

Finally, I leveraged a recent scRNA-seq dataset with newly diagnosed and recurrent GB tumor cells to see whether the trends observed in bulk RNA-seq data could be recapitulated if only tumor cells were considered [195]. Indeed, re-analysis of this tumor scRNA-seq showed that *SOX10* expression is downregulated in the recurrent tumor cells, accompanied by an upregulation of *SOX9* and an increase in gene signature scores related to quiescence stem cell properties (**Figure 31E and F**).

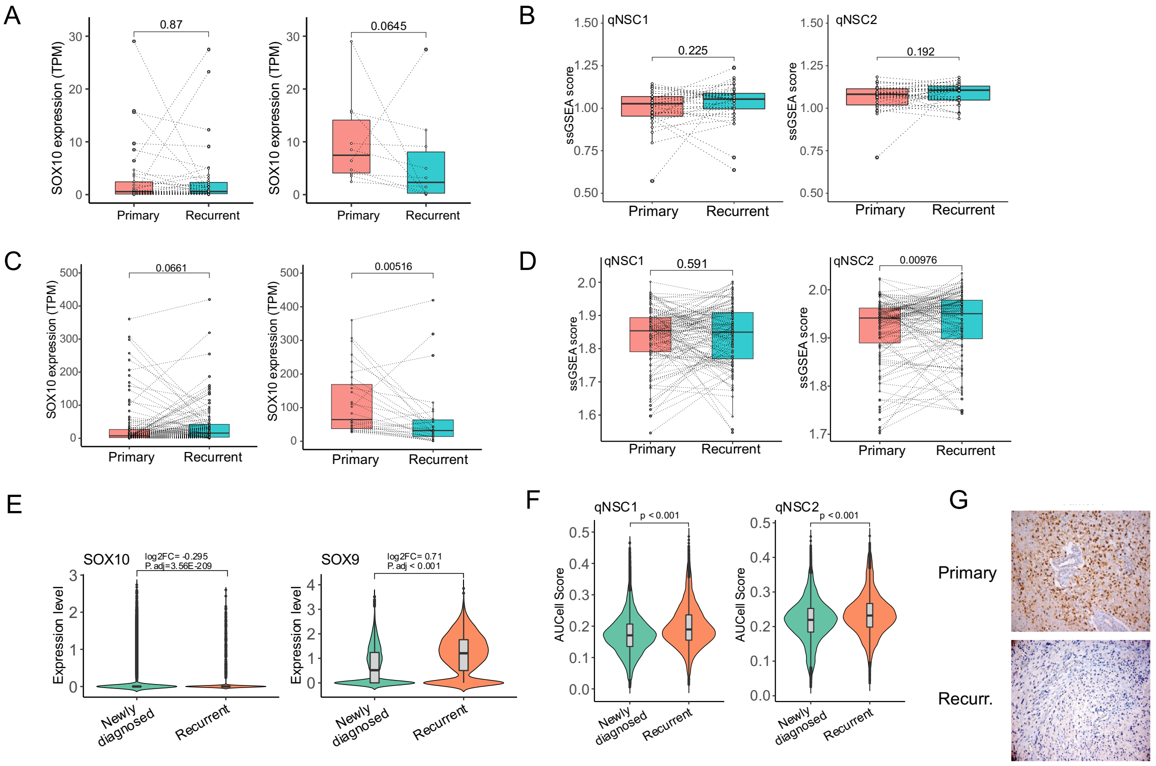

Figure 31. Analysis of published primary and recurrent GB patient data.

(A and B) Analysis of our own matched primary-recurrent GB pairs [27] (n = 37 pairs). (A) *SOX10* expression level in the entire cohort (left, n=37 pairs) and primary samples with the top 25% of *SOX10* expression (right, n = 10 pairs). (B) ssGSEA scores of qNSC1 and qNSC2 (Kalamanis et al., 2020) of primary and recurrent tumors in this cohort (n = 37 pairs). (C and D) Analysis of the 2022 updates of the GLASS cohort of matched primary-recurrent GB pairs [196] (114 pairs). (C) *SOX10* expression level in the entire cohort (left, n=114 pairs) and primary samples with the top 25% of *SOX10* expression (right, n = 29 pairs). (D) ssGSEA scores of qNSC1 and qNSC2 (Kalamanis et al., 2020) of primary and recurrent tumors in this cohort (n = 114 pairs). In both cohorts, only IDH-WT samples were considered. Median ± IQR is shown. P values were calculated using Wilcoxon's paired t-tests. (E and F) Single-cell RNA-seq data of unmatched newly diagnosed (n = 11) and recurrent tumors (n = 5) from Abdelfattch et al., 2022 [195] were re-analyzed. Only tumor cells were considered in this analysis. (E) Violin plots showing the expression levels of *SOX10* and *SOX9* in newly diagnosed and recurrent tumors. Log2 fold change (recurrent vs. newly diagnosed) and adjusted p values (unpaired two-tailed Wilcoxon's rank sum test and adjusted p values based on Bonferroni corrections) were reported above the plots. (F) Bar plots show the AUCell scores of qNSC1 and qNSC2 gene signatures in newly diagnosed and recurrent tumor cells. P-values were calculated by two-tailed Wilcoxon's rank sum tests. (G) Representative images of *SOX10* IHC validate its downregulation upon recurrence in a patient whose primary sample has a high *SOX10* expression in our cohort.

3.6 Potential treatment strategies

Results above indicated the cellular plasticity mediated by the downregulation of *SOX10* in tumor cells through the upregulation of *SOX9* and the activation of Notch signaling pathways.These *SOX10*-low cells were able to enter a slow-cycling state to safeguard their cancer stemness, leading to their resistance to differentiation cues and therapeutic pressure by TMZ. Therefore, in this section, I explored the possibility of a “state-inducing” therapeutic strategy, whereby the quiescent-like tumor cells are first pushed out of their slow-cycling state and then targeted by another compound, which aims at their subsequent fast-cycling state. Since Notch inhibition can drive the qNSC-like state to a more proliferative state [68, 226, 227], I considered the Notch inhibitor as the starting point for this exploratory endeavor.

3.6.1 Notch inhibition by gamma-secretase inhibitor stimulates the proliferation of KD-tumor cells

To examine the effects of Notch pathway inhibition, I chose the gamma-secretase inhibitor LY411575, which has been shown to attenuate Notch signaling [230] effectively. Application of LY411575 at 2 μM caused marked ablation of Notch intracellular domain (NICD) (**Figure 32A**), accompanied by a drastic decrease in the expression of Notch-responsive gene Hes5, suggesting that LY411575 potently suppressed Notch pathways in both Ctrl and KD cells (**Figure 32B**). Notably, cell death as a result of LY411575 (up to 10 μM) was minimal, as determined by annexin V apoptosis assays, suggesting that LY411575 exerts its inhibitory function without having cytotoxic effects at these concentrations (**Figure 34D**).

To gain an overview of the cell state changes associated with Notch inhibitor treatment, total RNA was extracted from the Ctrl and KD cells treated with DMSO or LY411575 (2 μM) for 48 h and expression profiling was performed. GO-biological process (GO-BP) pathway analyses of the upregulated and downregulated genes in the KD cells revealed that LY411575-treated KD cells downregulated genes involved in carbohydrate and lipid metabolism, suggesting a metabolic rewiring occurring as a result of the Notch inhibition (**Figure 32C**). In contrast, treated KD cells upregulated pathways involved in DNA replication, RNA splicing and cell cycle transition. These pathway alterations indicating decreased lipid metabolism and increased cell cycle gene activity are reminiscing the phenotypic changes which occur as cells switch from a slow-cycling to a fast-cycling state (**Figure 32D**) [228]. Interestingly, genes involved in neuronal differentiation were also upregulated upon LY411575 treatment, likely mediated through the increase in histone acetylation of the neuronal lineage-related genes, as previously reported [229]. In addition, some genes which were related to qNSC activation and proliferation, including Ascl1, were validated by qPCR. (**Figure 32E**). Notably, treated cells increased the protein level of cyclin D1, a key cell cycle regulator, upon treatment with LY411575, lending additional support that the treated cells assume more proliferative status upon Notch inhibition treatment (**Figure 32F**).

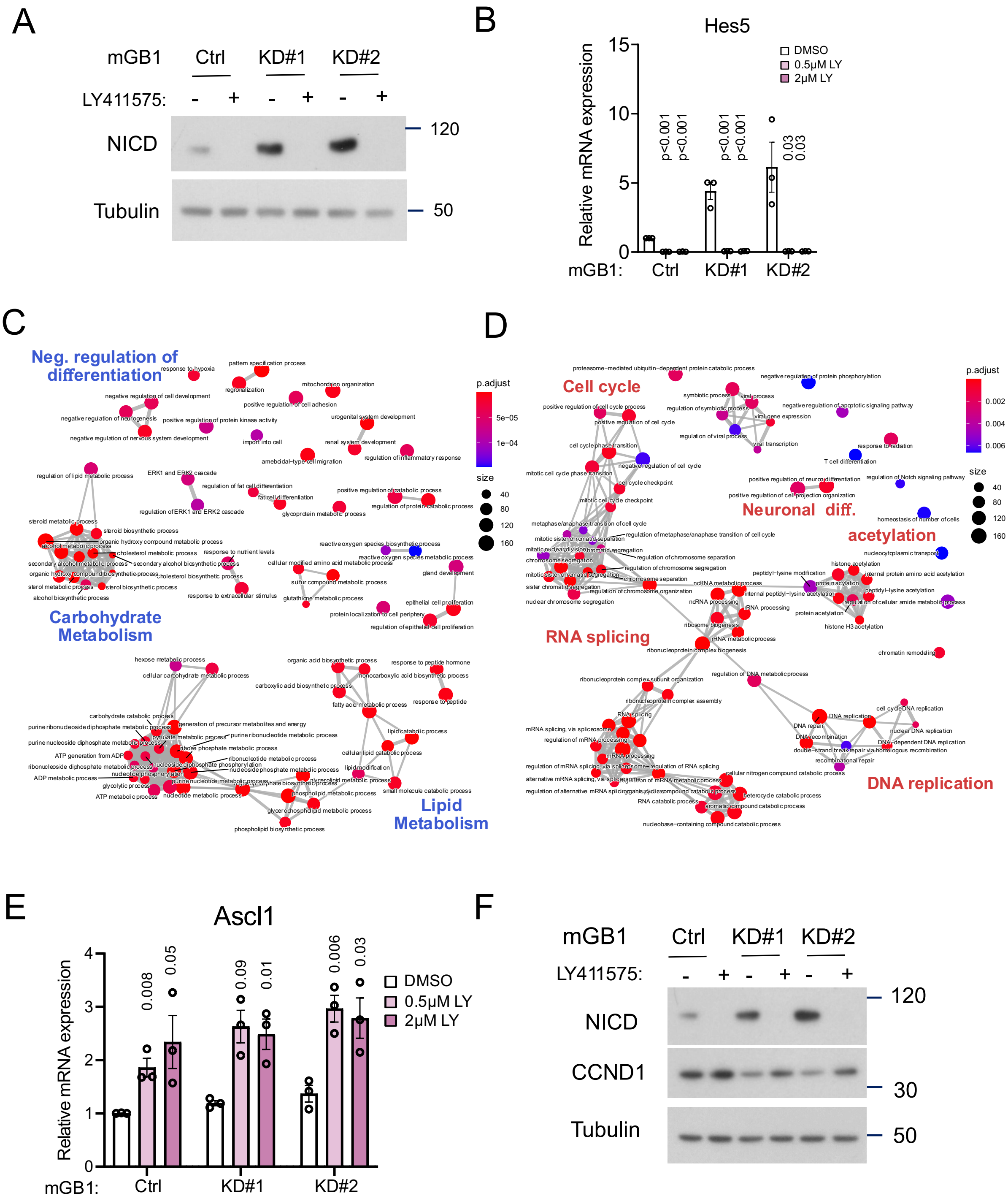

Figure 32. Notch inhibition by LY411575 in mGB1 cells.

(A) Western blot analysis of NICD expression upon LY411575 (2 μM, for 48h) in mGB1 Ctrl and KD cells. Tubulin was used as a loading control. (B) mRNA expression of Notch target gene Hes5 upon DMSO or LY411575 treatment at 0.5 μM and 2 μM for 48h. P values were calculated with unpaired t-tests. (C and D) Enrichment maps of the GO-BP terms enriched in (C) downregulated genes and (D) upregulated genes. GO terms with semantic similarity are arranged into a functional module with edges connecting to similar genesets. (E) mRNA expression of Ascl1 upon LY411575 treatment at 0.5 μM and 2 μM for 48h. P values were calculated with unpaired t-tests. (F) Western blot analysis of NICD expression and cyclin D1 expression upon LY411575 treatment for 48 hrs. Tubulin was used as a loading control.

Phenotypically, Notch inhibitor treatment decreased the proportion of p27-positive KD cells under reduced growth factor conditions (**Figure 33A and B**). In line with this, LY411575-treated cells had a higher percentage of Edu-positive cells (**Figure 33D**). Notably, *SOX9* and p27 positivity seems to be uncoupled with each other in KD cells, suggesting that the stem cell compartment left its slow-cycling state upon LY411575 treatment, lending additional support that the slow-cycling state mediated by *SOX10*-KD is reversible and that Notch inhibition drives them out of this quiescent or slow-cycling state.

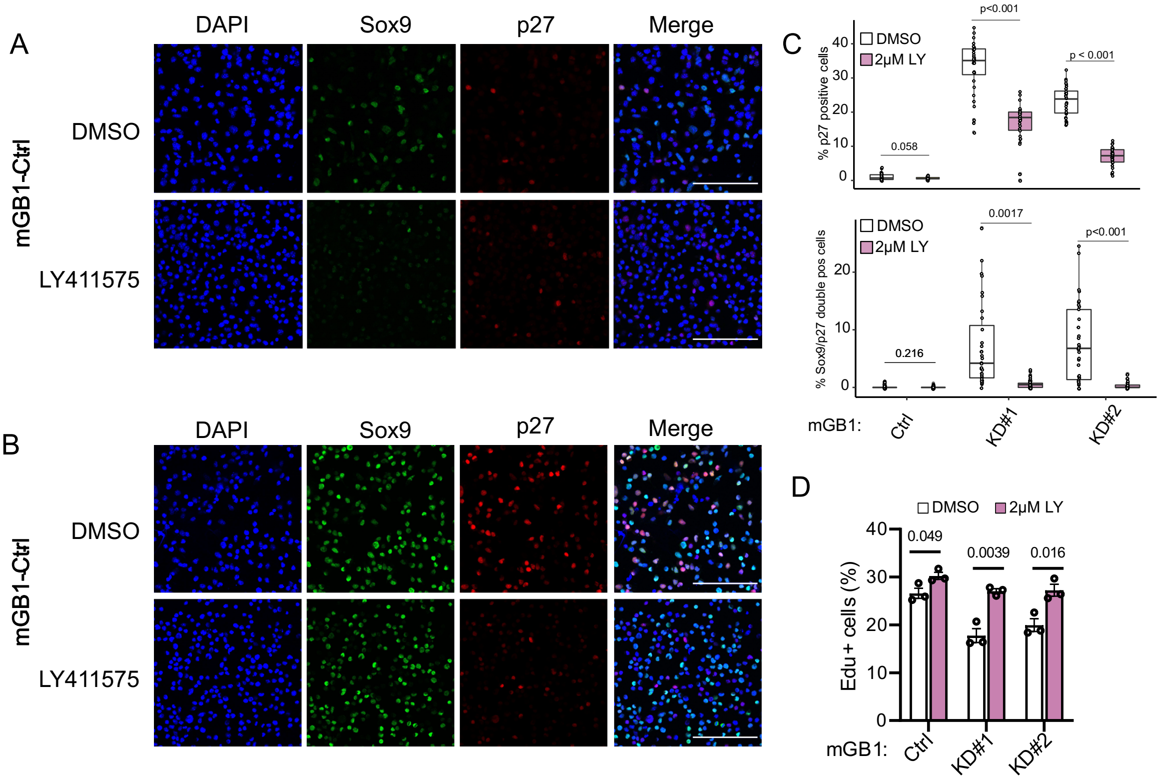

Figure 33. Phenotypic changes associated with Notch inhibitor treatment.

(A and B) Representative immunofluorescence images of (A) mGB1-Ctrl and (B) KD cells stained with Sox9 and p27 upon reduced growth factor conditions with and without LY411575 treatment. Scale bars = 100 μm. (C) Boxplots showing the results of quantifying the percentages of p27-positive (top) and Sox9 and p27 double-positive cells (below). Each dot represents the percentage of cells from an image (n = 30 images for each condition). Reported in the boxes are the median ± interquartile range. P values were computed using two-tailed unpaired T-tests. (D) Bar plots show the percentages of Edu-incorporated cells under each condition. Mean +/- SEM from three experiments. P values were calculated using a two-tailed unpaired t-test.

3.6.2 Combinatory treatment with Notch inhibitor

Given that LY411575 treatment drives cells to a relatively fast-cycling state, I explored whether its pre-treatment would sensitize KD cells to other anti-proliferative compounds. To this end, I worked closely with Dr. Yonghe Wu (Shanghai Institute for Advanced Immunochemical Studies (SIAIS), ShanghaiTech University, P.R.China), who performed a small-scale compound screen encompassing 78 therapeutic compounds targeting various proliferation-related signaling pathways, including ERK and PI3K-mTOR pathway, as well as other pertinent inhibitors such as those targeting redox homeostasis and epigenetic regulators (**Figure 34A and B**). mGB1-Ctrl and KD cells were first treated with DMSO or LY411575 at 2 µM for 24 h, and the compound libraries (2 µM) were added afterward for another 48 h treatment. A sensitivity index (SI) [201], which evaluates the effectiveness of the combination treatment by considering the difference between the observed and expected combined effect, was calculated. A positive SI indicates that the combination treatment exerts a more substantial inhibitory effect than LY411575 or the compound used alone. Using SI = 0.2 as a cutoff, several inhibitors targeting common pathways were identified for KD cells. These include compounds targeting cell cycle regulators, redox homeostasis and other epigenetic regulators, likely indicating the dependence of these pathways as KD cells were driven from the slow-cycling state by Notch inhibition (Tables of **Figure 34A and B**).

Of note, the HDAC/PI3K dual inhibitor Fimepinostat is an attractive hit for the following reasons. First, it has been shown to target Myc-and Ccnd1-upregulated cells, whose expression was also upregulated in the LY411575 treated cells. Secondly, it has been used in pre-clinical brain tumor models with good tolerability and brain penetration. Lastly, its dual inhibition of HDAC/PI3K limits potential compensatory pathways. Therefore, I chose this compound to perform further *in vitro* validation. Pre-treatment of KD cells with LY411575 enhanced their killing by Fimepinostat at the low-nanomolar range (**Figure 34C**). Additionally, annexin V apoptosis assays showed that the combination of LY411575 and Fimepinostat increased the percentage of apoptotic KD cells (**Figure 34D**).

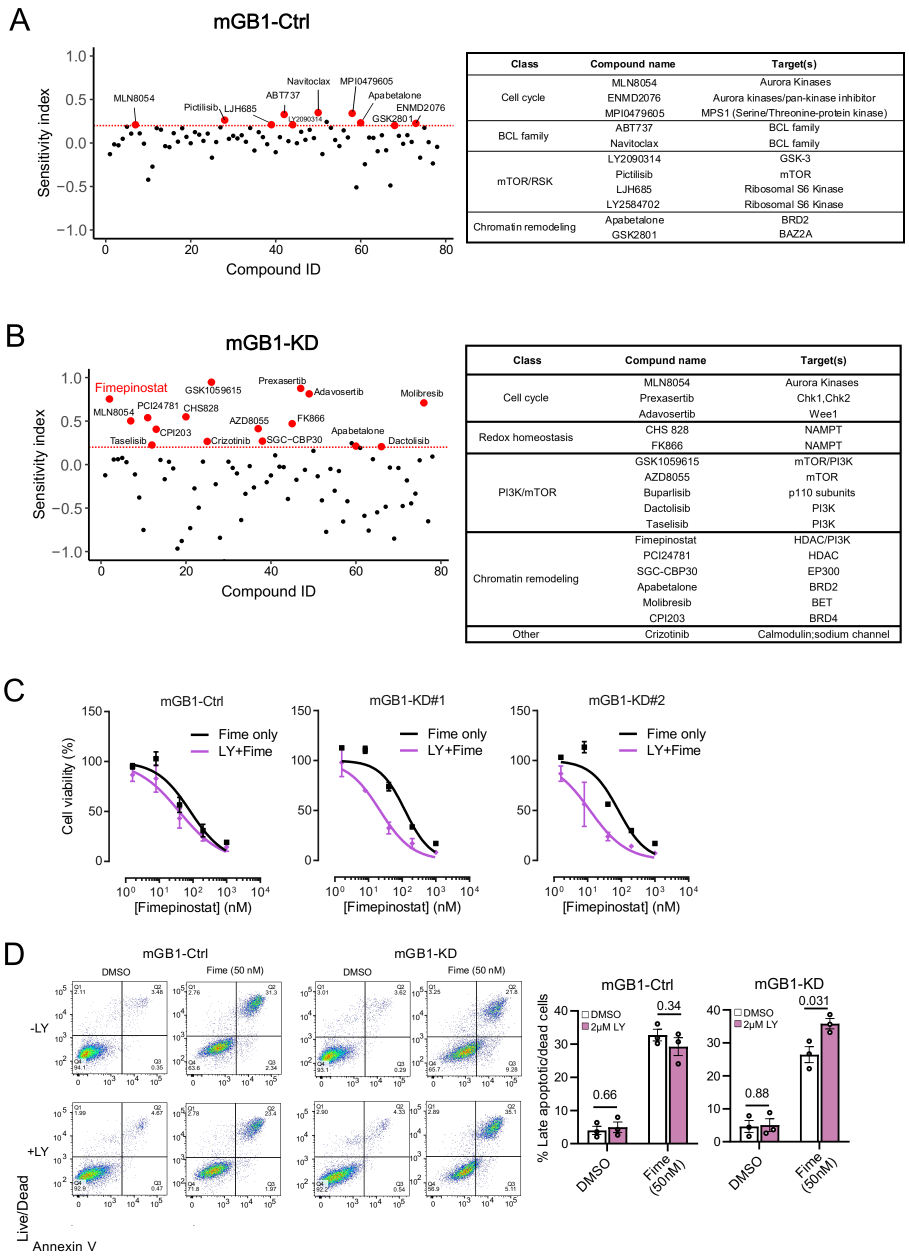

Class	Compound name	Target(s)
Cell cycle	MLN8054	Aurora Kinases
	ENMD2076	Aurora kinases/pan-kinase inhibitor
	MPI0479605	MPS1 (Serine/Threonine-protein kinase)
BCL family	ABT737	BCL family
	Navitoclax	BCL family
mTOR/RSK	LY2090314	GSK-3
	Pictilisib	mTOR
	LJH685	Ribosomal S6 Kinase
	LY2584702	Ribosomal S6 Kinase
Chromatin remodeling	Apabetalone	BRD2
	GSK2801	BAZ2A

Class	Compund name	Target(s)
Cell cycle	MLN8054	Aurora Kinases
	Prexasertib	Chk1,Chk2
	Adavosertib	Wee1
Redox homeostasis	CHS 828	NAMPT
	FK866	NAMPT
PI3K/mTOR	GSK1059615	mTOR/PI3K
	AZD8055	mTOR
	Buparlisib	p110 subunits
	Dactolisib	PI3K
	Taselisib	PI3K
Chromatin remodeling	Fimepinostat	HDAC/PI3K
	PCI24781	HDAC
	SGC-CBP30	EP300
	Apabetalone	BRD2
	Molibresib	BET
	CPI203	BRD4
Other	Crizotinib	Calmodulin;sodium channel

Figure 34. Identification of compounds for combinatory treatment with LY411575.

(A and B) Summary of the results of the compound screen in (A) mGB1-Ctrl cells and (B) mGB1-KD (KD#2) cells. The effectiveness of the combination with LY411575 pre-treatment was evaluated by the sensitivity index (SI) using the formula adopted from Chen et al. [201] and described in the method section 2.5.8. Compounds with SI above 0.2 (red horizontal lines) were labeled in red in the plots, and their targets were summarized in the tables on the right. (C) Dose-response curves of Fimepinostat alone (black curve) and LY411575 + Fimepinostat (purple curve) in mGB1-Ctrl and KD cells. Error bars represent mean ± SD from a representative experiment. (D) Scatter plots showing the Annexin-V and Live/Dead co-staining to label Annexin V and Live/Dead double positive, late-apoptotic cells. Bar plots show the percentage of later apoptotic cells (Annexin-V and 7-AAD double-positive cells) in mGB1-Ctrl and KD cells. Reported in the boxes are the mean ± SEM. P values were computed using two-tailed unpaired T-tests.

4 Discussion

GB is a devasting disease for which there is no effective treatment. Despite intense research efforts in comprehensively characterizing its genomic and epigenomic landscapes, no proposed therapies targeting the driver events in each GB subtype have substantially extended patients' survival so far [42, 230, 231]. Tumor progression and treatment failure are caused by intratumoral heterogeneity driven by the BTSCs, which preside over a hierarchy of tumor cells and mediate fundamental properties in GB progression, such as invasiveness and their resilience to therapeutic pressure. Findings from recent single-cell transcriptomic profiling substantiate the existence of this group of BTSCs and shed much-needed light on their phenotypic diversity and cellular architecture [122, 124, 127, 128]. Importantly, BTSCs often co-opt the gene regulatory networks in normal tissue stem cells and mediate their resilience toward immune surveillance and treatment pressure [98]. As such, novel therapeutic strategies necessitate a detailed understanding of the phenotypic plasticity mediated by the hijacking of BTSCs of these transcription networks. Prior work in our group identified *SOX10*, a pivotal oligodendroglial TF [168], as a master regulator of the RTK1 subtype [33]. We further showed that its downregulation leads to a more aggressive phenotype *in vitro*, likely driven by MES transition. Hence, this indicates that the transcription network driven by Sox10 can be exploited to mediate GB progression.

In my work presented here, I aimed to delineate the phenotypic plasticity mediated by the reduced expression of *SOX10* in the context of BTSCs and its relevance in therapeutic resilience. *In vivo* findings from this thesis suggest that Sox10 downregulation triggers lineage erosion in BTSCs, reverting them to a more NSC-like state. Single-cell transcriptomic profiling further supports such a transition and uncovers a quiescent founder state that drives this process. Furthermore, I showed that downregulation of Sox10 leads to the emergence of quiescent stem cell-like phenotypes in both mouse and human GSCs, which occurs similarly in TMZ-treated cells, suggesting that Sox10-low tumors may preserve a latent pool of quiescent neural stem cell-like tumor cells which fuel tumor regrowth. Further functional work demonstrated the feasibility of state-inducing therapeutic strategies depleting the quiescent stem cell state through Notch pathway inhibition and exposing the tumor to anti-proliferative treatment.

4.1 *In vivo* investigation of the phenotypic plasticity mediated by *SOX10*-low tumors

Following the hypothesis that the reduced expression of *SOX10* in tumor cells mediates phenotypic plasticity in BTSC, I first embarked on the *in vivo* investigation of phenotypic changes associated with *SOX10*-KD cells using a previously established NSC-derived mouse syngraft model [199]. This mouse model was chosen for the following reasons. First, unlike other existing syngeneic GB mouse models commonly used in the field, such as GL261 (carries mutations in K-Ras, which is rarely mutated in GB [16, 232]), they captured the frequently inactivated Trp53 and Pten in GB and hence the findings arising from this model would represent the phenotypic consequences of *SOX10* downregulation in GB cells in a more general genetic context. Second, these tumor cells were derived from NSCs, one of the proposed cell-of-origin of GB [50]. Therefore, they were maintained in non-differentiating conditions, allowing the study of the effects of *SOX10* on the BTSCs and the differentiation dynamics with this model. Finally, these cells can be injected into immunocompetent hosts, hence providing a unique opportunity to enable holistic determination of the phenotypic changes associated with *SOX10*-downregulation.

Intracranial injections of the KD tumor cells in syngeneic hosts revealed enhanced tumor aggressiveness, exemplified by rapid tumor development, increased invasive properties and enhanced immune cells infiltration (**Figure 9**), leading to shorter overall survival in the KD tumor group. These phenotypic changes showed a remarkable resemblance to the more progressed GB, demonstrating that *SOX10* reduction plays a role in mediating GB progression. Indeed, the aggressive features observed in this study echo a recent report from Brooks et al., who showed that *SOX10*-low human BTSCs initiated more rapid and invasive tumors in immuno-deficient mice [205]. As such, the parallel between my findings and that of Brooks et al. strongly supports the tumorigenicity of KD-tumor cells. Furthermore, it indicates commonality in the acquisition of tumor aggressiveness in both human and mouse BTSCs driven by Sox10 downregulation. Moreover, the observation that *SOX10*-KD cells developed aggressive tumors irrespective of the immune background of the mouse model speaks for the predominant roles of the tumor cell compartment in mediating the aggressive phenotypes subsequent to the reduction of *SOX10* in BTSCs.

I initially speculated that the aggressive properties were brought by the phenotypic transition of the KD cells to a more MES-GB-like cellular state. This working hypothesis is based on our group’s previous findings that downregulation of *SOX10* alters the enhancer landscape in tumor cells, leading to the activation of master regulators of the MES subtypes, including the AP-1 family of TF *FOSL1* and *FOSL2* [33]. Nevertheless, pathway analysis using TCGA-subtype gene signatures [31] on the bulk RNA-seq data on the Ctrl and KD tumors showed that the MES signature was not significantly enriched in the KD tumors (**Figure 11A**). Likewise, key MES-GB TFs and target genes, particularly Fosl2, along with other MES-GB signature chemokines or cytokines such as Ccl2, were not upregulated in the KD tumors (data not shown). Hence, mesenchymal transition is unlikely to be responsible for the aggressiveness observed in this *in vivo* model. One possible explanation for the discrepancy is the alteration of the enhancer landscape mediated by *SOX10* expressional reduction in more differentiated vs. more stem-like background, which highlights the context-dependent function of the SOX family TFs [172, 233, 234] (reviewed in Section 1.5.1). Moreover, recent findings showed that an immune attack is necessary for the MES-GB transition. Indeed, less T cell infiltration was noticed in the KD tumors, and hence KD tumors may lack the required immune attack from the immune surveillance program to drive the MES-GB transition (**Figure S2**) [34, 35].

Nevertheless, further analyses of the bulk RNA-seq data of the Ctrl and KD tumors revealed an alternative route of phenotypic transition driven by the reduction of *SOX10* in BTSCs. First, I observed that the KD tumors had higher ssGSEA scores for the classical subtype of GB (**Figure 11B**), whose expression signatures have been associated with the NSC development [15, 29, 30]. In line, pathway analysis using GO-BP demonstrated that the KD tumors enriched pathways related to development. Thus, these observations led to the hypothesis that the *SOX10*-KD tumors revert to a more NSC-like state (**Figure 11C and D**). Indeed, we and others have consistently observed the anti-correlation between the expression of *SOX10* and other RTK2/Classical subtypes master regulators such as *SOX9* and *EGFR* in cell lines and patient data [182, 188], indicative of the potential cellular state transition toward a developmental-like state via *SOX10* downregulation. This hypothesis is further corroborated by the marked phenotypic similarities observed in another study, where distinct lineages of the NSCs could give rise to tumors with different phenotypes. Specifically, the KD tumors resemble the Type 1, NSC-derived tumors, whereas the *SOX10* high tumors resemble the relatively less aggressive OPC-derived Type 2 tumors (**Figure 12**) [133].

During the development of normal NSCs, the expression of *SOX10* governs the core regulatory circuitry to sequentially activate genes responsible for oligodendrocyte differentiation and myelination to restrict their oligodendrocytic fate [168, 235]. Hence, it is conceivable that *SOX10*-high tumors retain such lineage memory and are committed to the more OPC-like, Type 2-like cellular state. Strikingly, my work here demonstrates that the reduction of the expression of Sox10 in tumor cells alone is sufficient to yield more Type 1, NSC-like tumors with more aggressive phenotypes (**Figure 12**). My *in vivo* observation here seems to indicate that the epigenetic memory for the lineage propensity of tumor cells could be overcome by modulating the critical lineage transcription factor network, resulting in the erosion of their original identity. In fact, lineage infidelity is one of the key phenotypic adaptations utilized by BTSC to contribute to tumor progression (reviewed in [49]). For example, Suva et al. reported that the cancer stemness of BTSCs is governed by a limited number of pluripotent TFs and their re-expression de-differentiates GB cell lines [107]. In another example, the expression of NG2 (an oligodendrocyte marker) fluctuates in tumor cells to reach an equilibrium where NG2$^+$ and NG2$^-$ BTSCs co-exist [119]. Finally, BTSCs can also trans-differentiate into endothelial cells, contributing to angiogenesis in GB [236]. This lineage flexibility of BTSCs is rendered possible through a more permissive epigenomic background that they often possess. The permissiveness of the epigenome BTSCs is highlighted in a recent multi-modal single-cell study, showing that stem-like states were maintained by the hypomethylation of PRC2 targets and the deposition of bivalent histone marks at the lineage-specific genes, permitting their reactivation under appropriate cellular contexts [134]. Thus, the less stringent epigenetic landscape in IDH-WT may allow for a lower “activation energy” to overcome the lineage barrier in the BTSCs. Indeed, Chaligne et al. also proposed a mathematical model which predicts that IDH-WT GB are characterized by concurrent differentiation and de-differentiated events, further demonstrating the fluidity of the BTSCs [134]. Hence, the downregulation of *SOX10* in these more permissive genetic and epigenetic backgrounds may drive the conversion of the tumor cells to hierarchically higher ranks, leading to the emergence of the tumors' resemblance to neurodevelopment. Importantly, the present data here accentuates the role of “lineage erosion” mediated by the downregulation of *SOX10* in BTSCs, speaking for a plastic developmental hierarchy operating in BTSCs.

4.2 Single-cell transcriptomic analysis revealed divergent cell fates mediated by SOX10 KD

Having shown that the KD tumor cells initiated aggressive tumors in the syngeneic host, I further elucidated the process of "lineage erosion" of BTSC driven by the downregulation of *SOX10*, bringing the cellular architecture of the KD tumors under sharper focus with scRNA-seq. Single-cell transcriptomic profiling is an indispensable part of the current study for the following reasons. First, scRNA-seq discerns the intra-tumoral heterogeneity after lineage erosion by Sox10-KD. Recent single-cell profiling studies have shed light on the phenotypic diversity of tumor cells within GB, which manifest themselves as a continuum of phenotypes spanning gradients of metabolomic [129], proliferative [130] or developmental states [83, 206]. Hence, findings from scRNA-seq would provide valuable insights into the phenotypic adaptations of KD tumor cells, particularly when faced with microenvironmental influence, which our syngeneic GB model uniquely recapitulates. Second, trajectory inference tools can also delineate the transition dynamics leading up to the development of aggressive tumors. Such information sheds light on the key events that occur during this process. Importantly, unlike other scRNA-seq studies, which relied on a marker-based selection of tumor cells [83, 122], our syngeneic GB model allows for an unbiased approach to isolate the totality of tumor cells based on the GFP expression, hence rendering a comprehensive determination of the cellular architecture by scRNA-seq feasible.

In keeping with the findings from the transcriptomic and phenotypic differences identified in the first part of the study, scRNA-seq analysis revealed striking differences in terms of their cellular potentials between Ctrl and KD tumors, even though both tumors were compared at their respective advanced stages. To begin with, more transcriptional clusters could be identified in the KD tumors relative to the Ctrl tumors, indicative of their extensive intra-tumoral heterogeneity (**Figure 14**). Second, more KD tumor cells were fast-cycling (**Figure 15)** and comprised the predominant components in the KD tumors, tying in with their rapid tumor development compared to the Ctrl tumors. Finally, the further signature analysis showed that the KD tumors possessed widespread cancer stemness features. This is manifested by the high expression of genes related to cancer stemness, such as *SOX2*, and other genes associated with neural stem cell development, such as Ptprz1 and Nes, whose functions in tumor development have been well-described (**Figure 16**). This vibrant cellular architecture is in sharp contrast to Ctrl tumors, where they showed more differentiated OPC/OL-like gene signatures and lower proliferation, tying in their higher expression of *SOX10* and their less aggressive features.

The cellular potentials of BTSCs define the possible phenotypes that they can assume. It also describes the potential "escape routes" available to the BTSCs. Hence, the higher the cellular potentials, the more possible "escape routes" are available to BTSCs to resist the harsh brain tumor microenvironment or treatment pressure [111]. For example, the presence of stem-like proliferating cells drives tumor expansion [122, 124]. On the other hand, recent reports show that neuronal-like tumor cells can also form a network to resist therapeutic intervention [237, 238]. Overall, the present data here indicate that upon lineage erosion via downregulation of Sox10, the rapid tumor growth observed at the phenotypic level is mediated by the proliferative and stemness cellular potentials. These results are congruent with previous scRNA-seq studies, which demonstrated the widespread presence of the stem and proliferative cellular states in aggressive GB [83]. Therefore, the present data indicate the emergence of stem and proliferative cells in the tumors, further underscoring the cellular potentials conferred by the downregulation of Sox10 in tumor cells.

Upon closer examination of the transcriptional clusters in the KD tumors, a clearer portrait of the dynamic cellular network within KD tumors was charted, revealing the likely origins of the cellular potentials upon lineage erosion by Sox10 downregulation. Importantly, KD tumors mirror neurodevelopmental trajectory, consistent with their resemblance to NSC-like tumors. Notably, a group of qNSC-like tumor cells was identified in the KD-tumor clusters (**Figure 18)**. This group of tumor cells is unique because they retain the proliferative and stemness capacity by maintaining a slow-cycling state during normal adult NSC development [68]. Upon activation, they can give rise to transit-amplifying progenitors and other differentiated progenies. Indeed, by comparing the gene signatures derived from normal NSC lineage progression from quiescent to activated or differentiated states, similarities between the KD transcriptional clusters and the normal NSC counterparts were drawn (**Figure 18**). The resemblance was further supported by the findings arising from RNA-velocity trajectory inference, where the more proliferative transcriptional clusters seemed to have stemmed from this group of quiescent stem cell-like tumor cells (**Figure 18**). It is worth pointing out that while the transcriptional similarities between cluster 12 and qNSCs are apparent, the possibility that it resembles other slow-cycling progenitor cells during NSC development, such as radial glial cells, cannot be precluded, given that these quiescent progenitor populations often share similar molecular profiles. The presence of quiescent stem cells has been long observed in tumor progression in response to therapeutic pressure [98, 131]. More recently, the multi-lineage potential of quiescent stem cells was demonstrated in scRNA-seq [220]. The quiescent-to-proliferative axis observed here is also supported by several other scRNA-seq studies. For example, Wang et al. proposed an axis of ascending proliferative capacities in GB tumor cells, where the root of this axis begins with quiescent tumor cells with astrocytic marker genes such as *GFAP* and *AQP4*, many of these genes are also shared with the qNSC-like tumor cells identified in this study [130]. In mouse GB models, Weng et al. observed that the development of proliferative and stem-like features in full-blown tumors entails the transition of astrocyte-like progenitor cells into a pri-OPC-like state [206]. On the other hand, Bhaduri et al. argue that the widespread stemness observed in GB is driven by a group of radial glial cell-like progenitor cells, which are the NSCs in the embryonic stage [83]. Finally, by analyzing the scRNA transcriptomes during different time points of the tumor development, Wang et al. identified fate-switching of tumor cells and placed the proliferative state at the end of the tumor development [132]. Taken together, the present scRNA-seq data suggest the emergence of quiescent/slow-cycling founder cellular state upon lineage erosion driven by *SOX10* downregulation, and their reactivation *in vivo* endows KD-tumors with proliferative, stem-like cellular potentials, leading to tumor aggressiveness at the phenotypic level.

4.3 *SOX10* downregulation leads to a quiescent stem cell state via Sox9 upregulation and Notch pathway activation

While the presence of qNSC-like tumor cells is supported by the scRNA-seq findings in this study and other relevant studies in GB, the quiescent stem cell state is computationally inferred. To strengthen the conclusions from the scRNA-seq data, I provided further experimental evidence that the ablation of *SOX10* imparts the slow cycling/quiescent phenotype in the context of BTSCs. GSEA resembled the KD cells to qNSC [67] and cluster 12 in our study at the transcriptomic level (**Figure 19**). Specifically, *SOX10* KD upregulates *SOX9* and Notch pathway target genes such as Hes5, whose expression is vital in maintaining the quiescent stem cell state (**Figure 19)** [68, 89, 90] I further showed that when grown under low-GF conditions, the KD cells preferentially entered G0 phase and could return to the cell cycle upon re-introduction of GF (**Figure 20)**. In line with this, the KD cells also showed an increase in the percentage of p27-positive cells, a commonly used marker for cells at quiescence in both normal and tumor cell settings [215, 216]. Most of the p27-positive quiescent cells were also positive for Sox9, providing direct evidence that lineage erosion triggered by Sox10 downregulation in BTSCs upregulates neural stem/progenitor cell marker Sox9 [162, 164, 239], and they are phenotypically quiescent (**Figure 21**). Interestingly, KD cells are resistant to differentiation cues, consistent with the roles of quiescent stem cells in reserving their proliferative and stemness features (**Figure 22**). My findings are supported by previous studies, which have shown that the reduction of *SOX10* is associated with a slow-cycling phenotype in both melanoma and glioma [188, 191, 194, 240]. Moreover, the slow-cycling state is potentially achieved through the upregulation of *SOX9*, which limits stem cell proliferation under the contexts of both normal stem cells and cancer stem cells [241-245]. During oligodendrogenesis, Sox10 suppresses Sox9 through mir-135 [182]. In the adult intestinal stem cell niche, *SOX9* expression (along with Hopx and Lrig1, which are quiescence markers for other cell types [246, 247] which were also upregulated in the KD cells) is high in intestinal quiescent stem cells to reserve the pool of progenitors to safeguard intestinal tissue homeostasis. Ablation of Sox9 rendered intestinal stem cells more susceptible to irradiation and affected epithelial regeneration [248]. In adult mouse SVZ, Sox9 is a master TF of the qNSC-state [68]. In radial glial cells, Sox9 expression is critical in balancing the fate choice between neuronal differentiation or maintaining a progenitor state. The upregulation of Sox9 increases the percentage of Mcm2+/Ki67- G0/G1 phase cells to prolong their cell cycle duration, thereby halting their lineage progression [71]. In cancer stem cells, *SOX9* has been shown to drive dormancy/quiescence programs in head and neck cancer, breast cancer and most recently in medulloblastoma [241, 245]. In parallel, the quiescence state observed could also be mediated by the upregulation of Notch pathway activity. In NSCs, qNSC upregulates Hes1 and Hes5 to suppress the expression of Ascl1 to prevent the lineage progression from qNSC to the transit-amplifying progenitor state [69]. In line with this, slow-cycling BTSCs often upregulate the Notch pathway to mediate a differential epigenetic landscape via KDM6 [98]. Similar observations were made in human BTSCs, where *SOX10*-KD caused an upregulation of *SOX9* and the activation of Notch pathway target genes, accompanied by increased numbers of G0 and p27-positive cells (**Figure 25)**. The tumorigenicity of the KD cells was also assessed using GLICO, where the KD tumor cells initiated bigger tumor sizes in the cerebral organoids compared to the Ctrl cells (**Figure 26**). Taken together, my results here indicate that lineage erosion driven by *SOX10* downregulation entails not only the stripping of the oligodendrocytic fate but also imparts a slow-cycling founder state driven by Sox9 upregulation and Notch pathway activation.

Interestingly, I also observed a lower expression of MHC-I molecules upon Sox10-KD in differentiation by serum (**Figure 23)**, suggesting that the KD cells may lower their antigen presentation in response to differentiation cues. My results here are consistent with a loss-of-function screen in melanoma, which showed that SOX10 is one of the top hits whose loss-of-function enables tumor cells to evade CD8+ T cells killing *in vitro* [123], providing a potential link to the quiescent phenotype and the lower T-cell infiltration observed in the stromal compartment observed in the KD tumors (**Figure S2**). While the causality between these two phenotypes remains speculative, recent studies have shown that the quiescent tissue stem cells such as hair follicle stem cells and muscle stem cells can lower antigen-presentation molecules' expression to evade adaptive immunity [217]. In tumors, disseminated cancer cells from pancreatic ductal adenocarcinoma can remain quiescent and evade adaptive immunity by turning off the MHC-I molecule expression [249]. More recently, it has been shown in breast cancer that quiescent cancer cells can form an immunosuppressive niche to resist immune attack from the host [218]. Therefore, Sox10-KD tumor cells may acquire the immune-evasive properties commonly used in quiescent stem cells to hide from immune surveillance programs and augment their rapid tumor development.

4.4 Therapeutic implications

The findings from this study were further evaluated for their relevance in therapeutic resistance, revealing the reduced expression of *SOX10* in tumor cells upon TMZ treatment, resulting in a slow-cycling drug-resistant cellular state **(Figure 26 and Figure 28)**. When these cells recovered from long-term TMZ treatment, they retained the *SOX10*-low, *SOX9*-high cellular state and harbored more *SOX9*/p27 double-positive cells, likely contributing to the higher TMZ resistance compared to the treatment naïve counterparts, reminiscing the phenotypic transition observed in the previous sections using shRNA-mediated Sox10-KD in mGB1 mouse model (**Figure 30)**. GB invariably relapses despite aggressive multimodal therapy. While genetic mutations can give rise to resistant clones, which ultimately leads to the development of increasingly resistant tumors at recurrence in other tumor types, such genetic mechanisms may not be held accountable for therapeutic resistance in GB, likely owing to the broadly similar mutational profiles of primary and recurrent GB [24-26]. Hence, phenotypic plasticity driven by non-genetic mechanisms constitutes a more likely route to acquire therapeutic resistance in GB. This process usually entails the emergence of a slow-cycling, therapy-resistant founder state, followed by their subsequent re-activation when the therapeutic pressure is lifted [220]. For example, Chen et al. showed that TMZ treatment selectively ablated fast-cycling cells in more differentiated backgrounds [131]. The treatment-induced quiescent state can be achieved through the re-configuration of the transcriptional program. Examples include the upregulation of pluripotent TFs such as *SOX2* [120]. Alternatively, the dormant state can also be acquired through metabolic rewiring. For example, Rusu et al. showed that dormant BTSCs divert their metabolism from glycolysis to glycerol metabolism via GPD1 in a process akin to embryonic diapause [112]. More recently, redox homeostasis has also been shown to govern the switch between fast cycling vs. slow cycling drug persister state in response to *EGFR* inhibition [228]. The findings in this study suggest that the quiescent/dormant founder state can be acquired via lineage erosion/conversion by *SOX10* reduction, adding to the growing body of evidence that the perturbation of TF networks is instrumental in the phenotypic adaptation of BTSC under treatment pressure. Indeed, the role of Sox10 in mediating therapeutic resistance has been shown in melanoma, particularly under BRAF inhibitor treatment [188, 189]. In brain tumors, SOX10 expression is downregulated in a murine brain tumor model upon irradiation [194]. In a recent single-cell transcriptomic profiling from Tirosh's group, IDH-mutant oligodendroglioma (harboring mostly OPC-like cells) showed a similar transition to an AC-like cellular state upon IDH-inhibitor treatment [250]. Hence, it is plausible that SOX10-high, OPC-like tumor cells downregulate *SOX10* expression in response to treatment pressure to mediate a transition towards a more AC/NSC-like cellular state.

What is unexpected in my findings is the observation that some of the quiescent stem cells remained in the recovered population even after the therapeutic pressure had been lifted, incompatible with the fully reversible "drug-tolerant persister state" proposed in GB and other types of cancer [98, 251]. These models assert that the development of drug resistance is a stochastic, non-hierarchical process whereby drug treatment selects for a transient, slow-cycling, drug-tolerant state, which can revert to the original cellular state after treatment withdrawal. They also predicted that the recovered population would have a similar drug sensitivity and heterogeneity as the parental cells, which was not observed in my current results (**Figure 30**). The discrepancy could be explained by the differences in the cell models used – most of the drug-tolerant persister phenotype studies used more differentiated cell lines, where the hierarchical arrangement of tumor cells is not as pronounced as in the cancer stem cell models used in this study. Hence, stochastic phenotypic transitions may be a more predominant driving force for drug resistance in these more classic differentiated tumor cell models. In support of my findings, a recent study showed that quiescent stem cells persist upon tumor recurrence [220]. My analysis indicated that recurrent tumors had enhanced quiescence signatures in matched pair bulk RNA-seq and non-matched scRNA-seq data (**Figure 31)**.

Given the higher cellular potential of quiescent stem cells, it is conceivable that maintaining this cell population would provide "escape routes" to drive tumor development. In this study, the mechanisms mediating the maintenance of the quiescent stem cells remain elusive. However, I speculate that cell-cell interactions might be key to their maintenance. In normal development, activated adult NSCs can maintain the qNSC pool by upregulating Notch ligand Dll1 or Lfng to maintain the Notch pathway via lateral inhibition [97, 252] (**Figure 3**). Indeed, the upregulation of Notch ligands such as Dll1 and Dll3 was also observed in the more proliferative clusters. Thus, the activated, proliferative tumor cells may actively maintain the pool of quiescent stem cells in the tumor via the Notch pathway. Further investigation of the cellular interactions will reveal determinants of quiescent stem cell maintenance upon recovery from treatment pressure. In particular, longitudinal analyses of the single cell transcriptome profiles of a single patient from primary, in treatment and after recurrence,would provide valuable insights into the changes of the cellular architecture during GB progression.

4.5 Proof of concept drug study

Finally, the utility of the Sox10-KD quiescent stem cell model in searching for a novel therapeutic strategy was further explored. The intra-tumoral heterogeneity and phenotypic plasticity of GB guaranties the failure of monotherapy. Therefore, the field is moving toward effective combinatorial treatment strategies, considering the diversity and fluidity of different cellular states and simultaneously targeting them. Ideally, such a combination strategy should strive to target the cellular states in a tumor while using a minimal number of compounds. Given our current knowledge of the tumor cell landscape in GB, two major combination strategies have been proposed. First, based on their two-cell-state GB model, Wang et al. demonstrated the potential of simultaneously eradicating the slow- and fast-cycling cellular states using a conventional brain tumor cell line (U87MG). This strategy is the minimalistic approach for combination therapy since the slow-cycling to fast-cycling cellular state is the simplest axis that explains the phenotypes across different cellular states [130]. However, one caveat of such an approach is that the slow-cycling cellular state is often difficult to target. They are usually more therapy-resistant, explaining the high drug concentrations needed to exert the effect in their study. The second approach took into consideration the plasticity of BTSCs and proposed a combination treatment by first inducing them to a more manageable cellular state (“State-inducing”), followed by the subsequent targeting of the eventual cellular state (“State-killing”) [144]. Yet, which cell state is more manageable therapeutically remains a largely contentious issue, let alone the means to induce and target such a “manageable state.” Here, inspired by the therapeutic lock-out approach used in other tumor types [253-255], I tested the feasibility of first driving the quiescent cellular state to a more proliferative state using Notch inhibitors, followed by their subsequent targeting by compounds effective to remove the fast-cycling cells. In principle, this strategy would not only circumvent the need to identify compounds effective for eliminating the slow-cycling state but would also abrogate the quiescent stem cell state to block the potential “escape routes” through which the tumor cells can be replenished.

A potent Notch pathway inhibitor LY411575 was chosen to test the possibility of the therapeutic strategy. LY411575 is a gamma-secretase inhibitor (GSI) that targets the S3 cleavage site and prevents the Notch pathway activation. It has been used in mouse models in the context of Alzheimer's disease, where the administration of LY411575 inhibited the formation of β-amyloid [256]. My results here showed that treatment with LY411575 activates the cell cycle program and proliferation phenotype, suggesting that the quiescence stem cell state can be induced to a faster-cycling state (**Figure 32**). Interestingly, upon LY411575 treatment, immunofluorescence analysis showed that Sox9 and p27 positivity uncoupled, suggesting that the stem cell compartment has become less quiescent compared to the DMSO control (**Figure 33**). Furthermore, compound screening showed that KD cells became more susceptible to anti-proliferative compounds upon pre-treatment with Notch inhibitor, including those that target redox homeostasis and cell cycle regulators, suggesting that the change of the proliferation status exposes the KD cells to targeting them with anti-proliferative compounds (**Figure**

34). My results are consistent with my observations in myocytes, neural stem cells and BTSCs directly derived from the NSCs [68, 226, 227]. However, some other studies suggest that the inhibition of Notch pathways leads to the apoptosis of GSCs. These contradictory findings may stem from the differences in treatment time (15 days in [98] vs. 2 days in this study). Alternatively, since our current mouse GB model is directly derived from NSCs, it is plausible that these tumor cells might preserve the ancestral behavior of NSCs compared with other models. Conceivably, given that the slow-cycling cellular state could be acquired through other mechanisms such as metabolic rewiring [109], Notch inhibitors may not be universally useful in inducing all the quiescent cellular to more proliferative states. Nonetheless, the inhibition of the Notch pathway provides an excellent starting point for testing the feasibility of this therapeutic strategy in this model, given its druggability and well-documented involvement in quiescent NSC biology.

The dual HDAC and PI3K inhibitor, Fimepinostat (or CUDC-907), was chosen for further validation, revealing increased efficacy in targeting KD cells when pre-treated with Notch inhibitor as increased apoptotic cells upon combinatory treatment *in vitro* (**Figure 34**). Fimepinostat was first synthesized to target both PI3K and HDAC pathways and showed potent anti-proliferative activity across a wide range of hematological and solid tumor cell lines at low-micromolar ranges. It also suppresses other proliferation-related pathways, including MAPK, STAT-3 and RTKs, cell cycle regulators and DNA damage repair pathways such as Wee-1 and Chk1 [257]. Its broad inhibitory effect is likely due to its deacetylation functions of both histone and non-histone proteins. Thus, it is unsurprising that Fimepinostat was fast-tracked in clinical testing in different cancer types (brain tumors: NCT03893487, breast cancer: NCT02307240, recurrent B-cell lymphoma: NCT02674750). In our study, Fimepinostat is an excellent candidate since it has been used in a mouse pediatric brain tumor model with an extension of overall survival as a single agent, demonstrating its bioavailability in the brain [258]. On the other hand, its all-encompassing inhibitory functions would be beneficial to target most of the potential proliferative states and suppress potential compensatory pathways. In particular, Fimepinostat has been shown to be effective in Myc-driven tumors and hence might be able to eliminate the activated NSCs as a result of the re-activation of quiescent stem cells [259]. As of the writing of this thesis, *in vivo* investigation on the therapeutic potential of the combinatory treatment of LY411575 and Fimepinostat in the Sox10-KD syngeneic mouse model has commenced. Preliminary results showed that the treatment combination was well-tolerated in the animals, despite previous reports concerning the adverse effects of long-term treatment of LY411575. Overall survival and scRNA-seq studies upon treatment with Fime with and without Notch inhibitor treatment will further validate the feasibility of this state-inducing strategy in an immune-competent background. Specifically, results from this *in vivo* work will reveal (1) whether the quiescent stem cell population can be depleted *in vivo* by Notch inhibitor; (2) whether its depletion by combination treatment will divert the tumor from a more developmental-like fate and (3) whether this combination strategy will extend the survival of the animals injected with the KD-tumor cells.

4.6 Limitations of the study

Due to the lack of *SOX10*-high syngeneic mouse models, this study was mainly performed in the mGB1 syngeneic mouse model, complemented with human BTSCs. Further validation using other syngeneic or spontaneous systems (such as RCAS-Tva spontaneous mouse GB models) will show whether the observed phenotypes in this study are universal across different genetic backgrounds. Nevertheless, the convergence of phenotypes across human models from this study and others lends additional support to my findings.

Another area not addressed in the current study is how the behavior of quiescent stem cells *in vivo* is modulated by the TME. Specifically, this study has yet to identify their re-activation and maintenance mechanisms in the tumors. One hypothesis for their reactivation is that they followed their natural path of reactivation, as in the case of quiescent stem cells. In normal development, the regulation of the quiescence state is maintained by niche signals or external cues. For example, quiescent NSCs upregulate different glutamate receptors to sense the tumor microenvironment and regulate their cell cycle exit or entry in response to these cues. For example, the pleiotropic molecule BDNF released from the neurons or the other differentiated-like tumor cells can bind to the TrkB receptors on the qNSCs to cause their reactivation [260]. Alternatively, qNSCs can also respond to injury signals such as TNF-a or IL-1a or Il1b to prime their cell cycle re-entry, especially in the case of stroke or pathological demyelination in multiple sclerosis. It was noticed that GO-BP analysis of cluster 12 revealed an upregulation of pathways related to glutamate receptors . Additionally, the TAM compartment of the KD tumors is characterized by the increase in the expression of pro-inflammatory cytokines, hence leading to the speculation that the re-activation of quiescent stem cells in the KD tumors may rely on the modulation from the TME. This is further supported by our preliminary findings that the secretome of *SOX10*-KD human cells stimulated pro-inflammatory cytokine profiles in monocyte-derived macrophages. Further studies dissecting the effect of different components of the stromal compartment may reveal determinants for the quiescence stem cell state *in vivo*. The findings from such studies are important in gaining a comprehensive picture of the cellular architecture and designing holistic therapeutic approaches, taking into account the complexity of the modulation of the stromal compartment.

5 Conclusion

The past decade saw a breakthrough in the granular understanding of the cellular architecture of GB, unveiling the cellular heterogeneity within this deadly disease. The field is also moving from molecular subtypes to the more subtle phenotypic switch that drives tumor progression and therapy resilence in search of novel therapeutic avenues. My work in this dissertation unraveled the phenotypic plasticity caused by the downregulation of Sox10 in the context of BTSCs, accentuating a quiescent founder state in mediating such phenotypic transitions toward GB aggressiveness. From a therapeutic standpoint, I used this model to demonstrate the feasibility of driving the quiescent founder state to a more proliferative one, potentially amenable to anti-proliferative treatment. My work adds to a growing body of evidence supporting the phenotypic fluidity of BTSCs and proposes a combination treatment strategy that warrants further *in vivo* validation.

6 Supplementary Information [2]

Given the scope and time constraint of the current thesis, the differences between the stromal compartments between Ctrl and KD tumors were not discussed at length in the previous chapters. However, some of the intriguing findings in the stromal compartment identified in the scRNA-seq study were nonetheless highlighted below to provide a more comprehensive picture of the aggressive properties of Sox10-KD tumors in the context of their stromal compositions.

6.1 Overview of the stromal data

To gain an overview of the stromal landscape of the Ctrl and KD tumors, GFP negative fractions from Ctrl and KD animals were extracted from the overall dataset and further analyzed. Initial analyses based on manual inspection of the marker genes in each cluster identified clusters with classical immune cell markers such as from TAM, dendritic cells and T cells. However, the identities of other clusters were less readily discernible. Therefore, to ascertain the cell identities of these clusters, all 16 clusters were separated as group 1 (clusters with apparent immune cell markers) and group 2 (clusters without apparent immune cell markers) and re-clustered separately to improve the granularity of the clustering (**Figure S1A**). They were then annotated with SingleR using two separate reference datasets: a dataset comprised of 358 bulk RNA-seq samples of the sorted mouse cell population was used as a general reference, whereas another mouse immune cell-focused dataset was used to annotate the immune cell populations better. The final identities of these clusters are shown in **Figure S1C**, revealing the widespread presence of macrophages in the stromal cells of both the Ctrl and KD populations. Hence, the combination of manual inspection and reference-based annotation of the stromal clusters provided added confidence in these clusters' identities and allowed for a more accurate comparison between the stromal landscapes between Ctrl and KD tumors.

6.2 Composition of the stromal components

Based on the annotations above, the proportions of each of the stromal cell populations were compared between Ctrl and KD tumors. As shown in **Figure S2A**, tumor-associated macrophages (TAM) made up the largest proportion of the stromal cell population in both Ctrl and KD animals, consistent with other studies in GB TME. In line with our group’s previous findings, there is a significantly higher abundance of TAMs in the KD immune cell compartment (OR = 2.19, $p < 0.001$). Interestingly, KD tumors have a significantly lower proportion of T cells (OR = 0.57, $p < 0.01$) and dendritic cells (OR = 0.29, $p < 0.001$) (**Figure S2B)**. These changes in immune cell populations match the immune landscape of a more aggressive GB. Notably, more non-immune cells were found in the KD tumors. For example, more endothelial cells can be found in the KD tumors, tying in with the increased vascularization of the KD tumors upon gross inspection. The presence of other non-immune cells (oligodendrocytes and neurons) may be due to the infiltrative nature of the cancer, leading to the inevitable inclusion of some of the

---

[2] The bioinformatics analyses were performed by Johanna Keding (Division of Applied Bioinformatics, DKFZ) during her master thesis research. Figures generated by her were used in this section.

normal brain cells in the datasets. Nonetheless, the differences between significant immune cell populations of Ctrl and KD tumor cells were still significant even after excluding these normal cell populations (**Figure S2B, right**). Hence, the present data suggest quantitative differences between the immune cell populations of Ctrl and KD tumors. Further validation and analyses were performed on T cells and TAMs, summarized below.

6.2.1 T cells

T cells make up the immune surveillance of tumor cells. Conceivably, the lower the infiltration of T cells in the tumors, the more uncontrollable the growth of the tumor is. Immunohistochemistry analysis of CD3-positive cells in the tumors showed a lower abundance of CD3-positive T cells in the KD tumors (around 3% in KD vs. 10% in Ctrl) (**Figure S2C**). Further analysis of the T cell cytotoxic and exhaustion scores revealed no significant differences, suggesting that the major difference between the two genotypes lies in their numerical differences in the tumors (data not shown). This lower abundance could be due to the lower expression of MHC-I molecules, as observed in the tumor fractions (**Figure 23**). Low MHC-I molecules expression on tumor cells lower their antigen expression level to evade the immune surveillance program. Therefore, the present data suggest that the tumor cell differences could drive the lower abundance of T cells in the KD tumors.

6.2.2 Tumor-associated macrophages

TAMs are the largest group of the immune cell population in GB. Their increased infiltration usually indicates an adverse prognosis. In addition, further pathway analysis using hallmark pathways showed that the KD-TAMs showed a stronger enrichment of the inflammatory pathway compared to the Ctrl-TAMs (**Figure S3A**). Ctrl-TAMs have a higher expression of genes involved in canonical monocyte and macrophage function, such as Ly6 and Tgfbi. In contrast, pro-inflammatory cytokines Il1a and Il1b were more regulated in the KD-TAMs (**Figure S3B**). In addition, further immunohistochemistry analysis showed that the KD-TAMs have a more bushy morphology than Ctrl-TAMs, which are often more rounded. This morphological difference is reminiscent of the neuroinflammatory microglia observed in other studies (**Figure S3C**). Indeed, conditioned medium from *SOX10*-KD cells induced the expression of pro-inflammatory cytokines in the monocyte-derived macrophages (**Figure S3D**). This piece of results also matches our previous observations on the KD-cell derived exosomes increase the pro-inflammatory cytokines in macrophages (unpublished data). It remains unclear the functions of the pro-inflammatory phenotype of TAMs in tumor progression at this stage. A pro-inflammatory TAMs is usually considered anti-tumor, as it is often associated with increased adaptive tumor immunity. However, a recent study showed that Il1a and Il1b is associated with worse prognosis in both human and mouse GB. Interestingly, the deletion of Il1a and Il1b led to fewer CD3 T cell infiltration and tumor cells staying at a quiescent state without acquiring proliferative phenotype, harkening back to the phenotypes observed in this study [261]. Hence, it is speculated that the quiescent KD cells might actively maintain a pro-inflammatory secretome to ensure its activation while maintaining an immunosuppressive TME. However, further analysis, especially the marker-based isolation of the TAMs, will be needed to confirm causality and test whether inhibiting the pro-inflammatory TAM phenotype constitutes a new therapeutic avenue to keep the quiescent stem cell at bay.

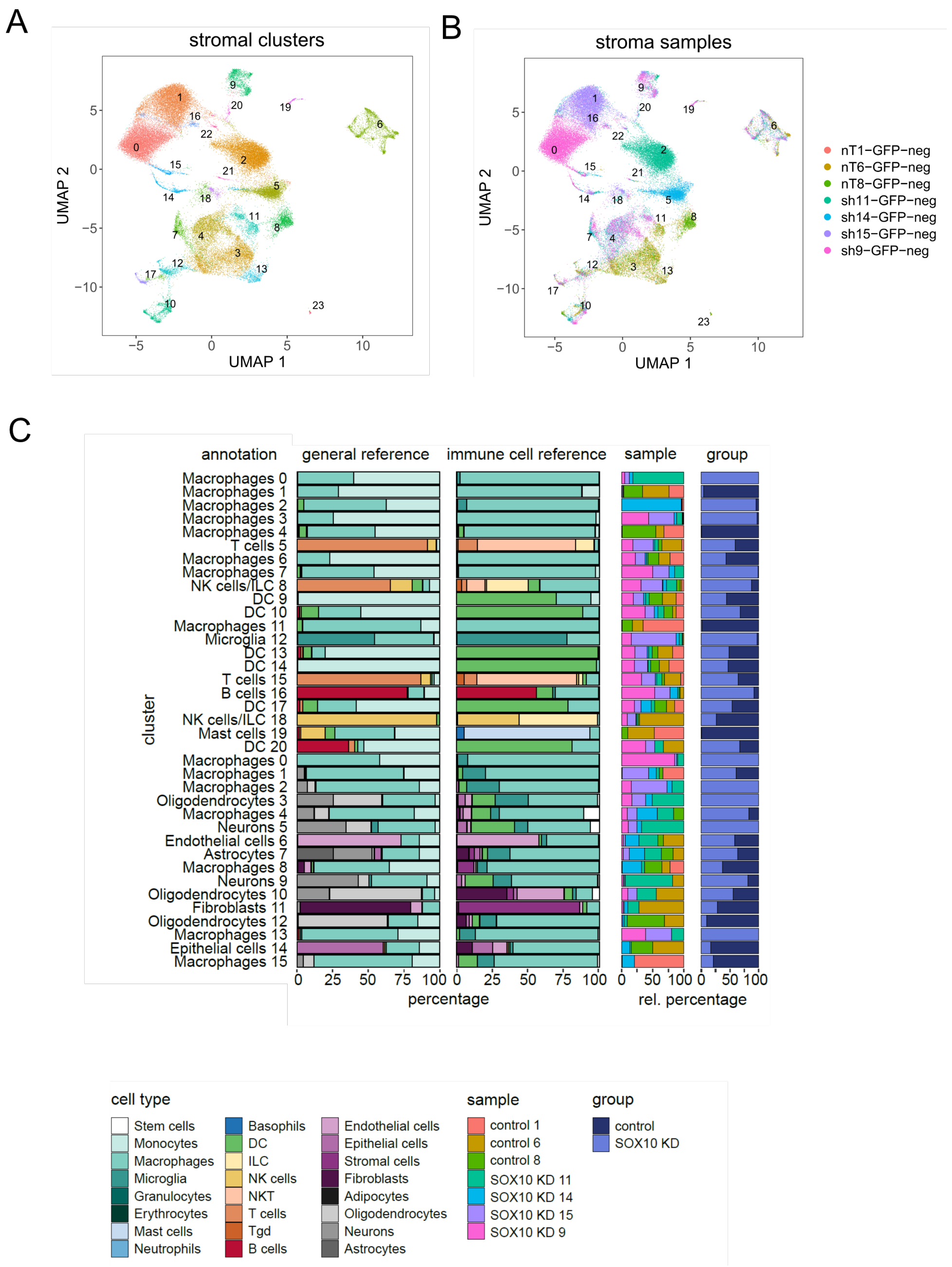

Figure S1. Stromal cell landscape of the Ctrl and KD tumors.
(A, B) UMAP plots of the GFP-negative samples by (A) Seurat clusters and (B) samples. (C) Clusters from the UMAPs of (A) were assigned to different cell identities using a general reference and immune cell-specific references provided in the singleR package

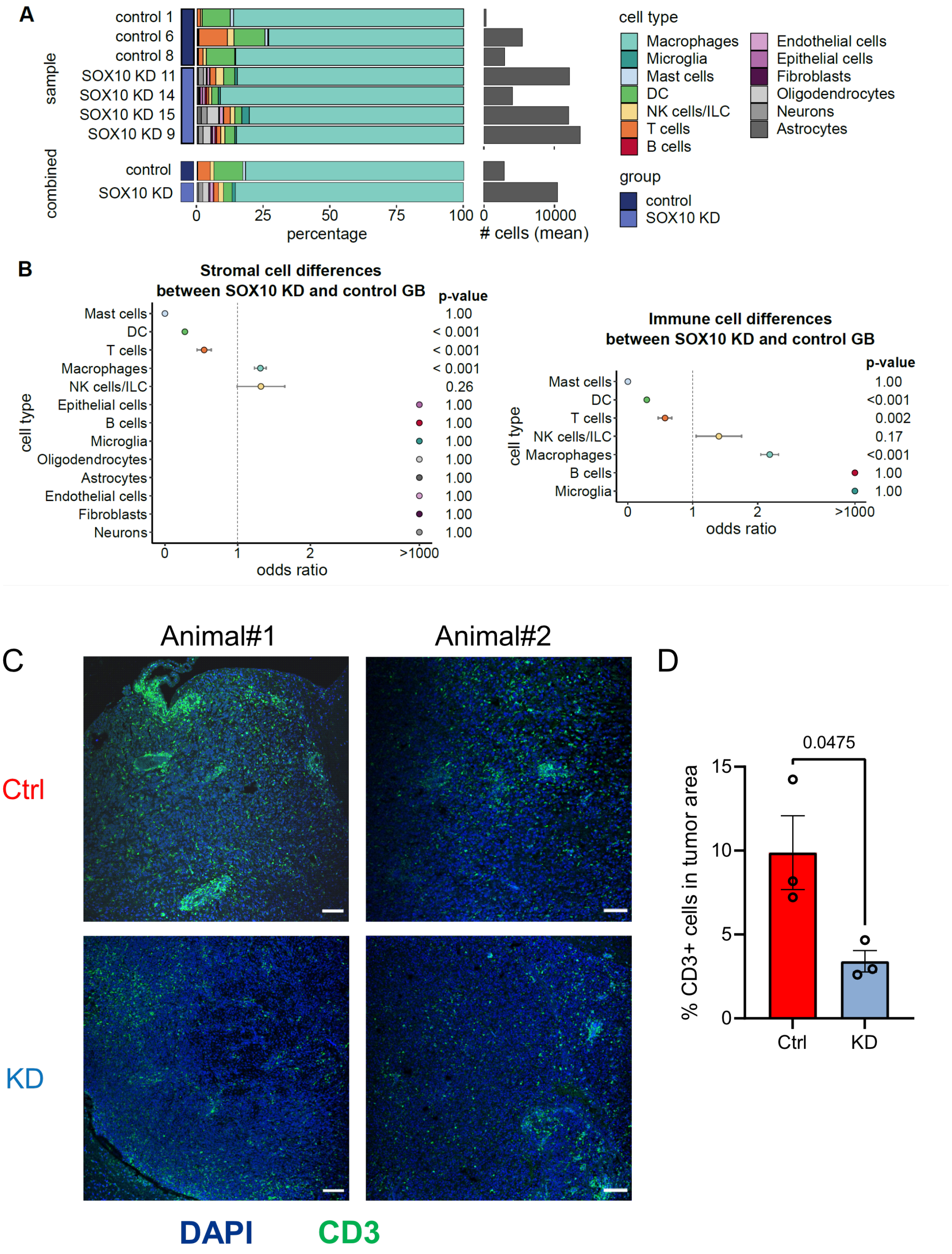

Figure S2. Comparison of immune cell compositions in Ctrl and KD tumors.

(A) Bar chart showing the composition of the stromal cells in individual mice. (B) Comparison of stromal and immune cell differences in KD tumors vs. Ctrl tumors. (C) Representative immunofluorescence CD3 (A general T cell marker) in Ctrl and KD animals. (D) Quantification of CD3+ cells in Ctrl and KD animals. Each dot represents the percentage of CD3+ T cells per mm^2 tumor area in one animal. P value was computed by T-test.

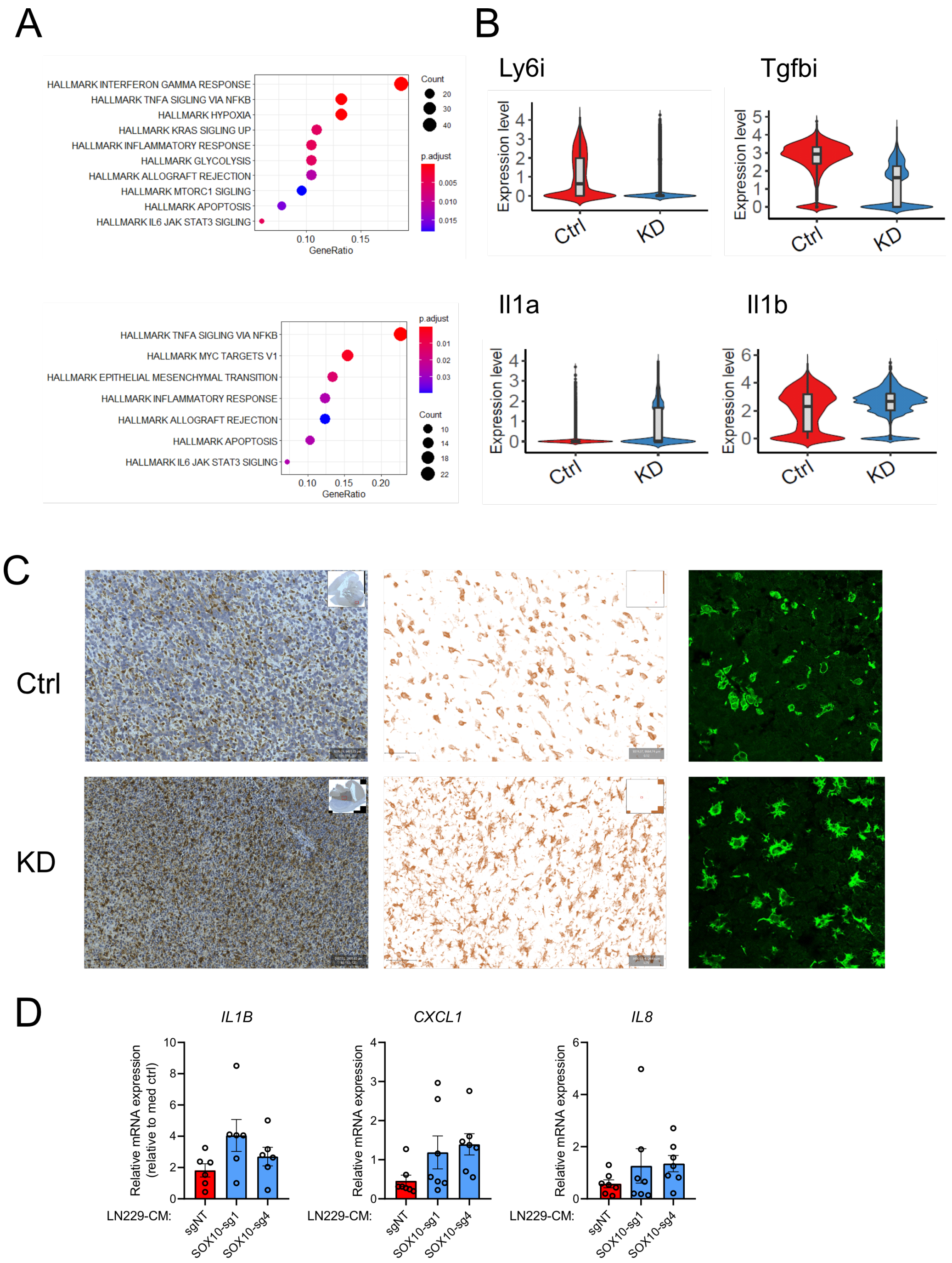

Figure S3. TAM differences between Ctrl and KD tumors.

(A) Dot plots summarizing the results of GSEA of the differentially regulated genes in the Ctrl-TAMs (top) and KD-TAMs (bottom) identified in the scRNA-seq study. (B) Representative gene expression related to canonical functions of TAM (top) and inflammatory TAM (bottom). (C) Morphology of TAM s in Ctrl and KD tumors identified by Iba1 immunohistochemistry and immunofluorescence. (D) mRNA expression of the proinflammatory cytokines of human monocyte-derived macrophages induced by conditioned medium (CM) from Ctrl tumor cells (red) and KD tumor cells (blue). Each dot represents the expression level of the indicated gene upon CM treatment in the monocyte-derived macrophages from one healthy donor.

6.3 Supplementary figures

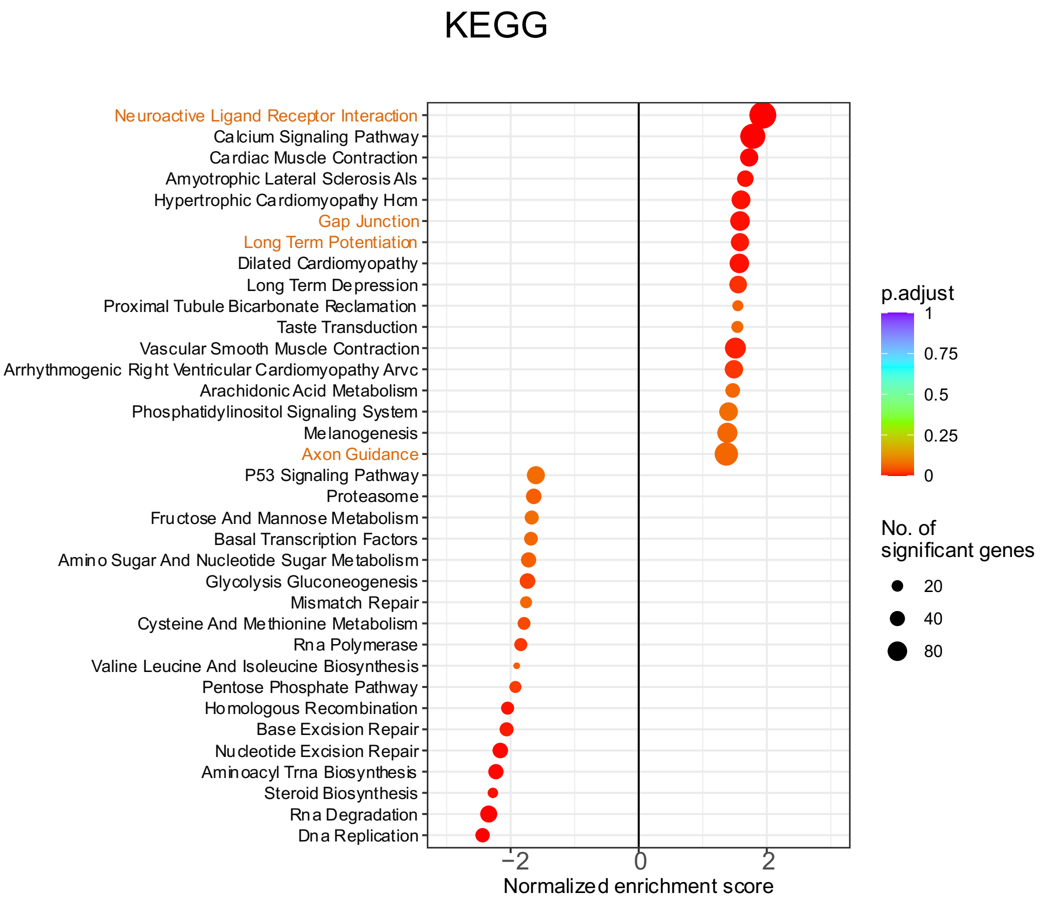

Figure S4. Analysis of bulk RNA-seq data of Ctrl and KD tumors.

Summary of Gene set enrichment analysis using KEGG pathways. X-axis depicts the normalized enrichment score (NES) of the geneset. A positive NES means the geneset is enriched in the KD tumor cells, whereas a negative NES means the geneset is enriched in the Ctrl tumor cells. Genesets were arranged by their enrichment scores, and the top 20 enriched genesets of KD and Ctrl tumors were shown. Genesets related to development were highlighted. Related to **Figure 11**.

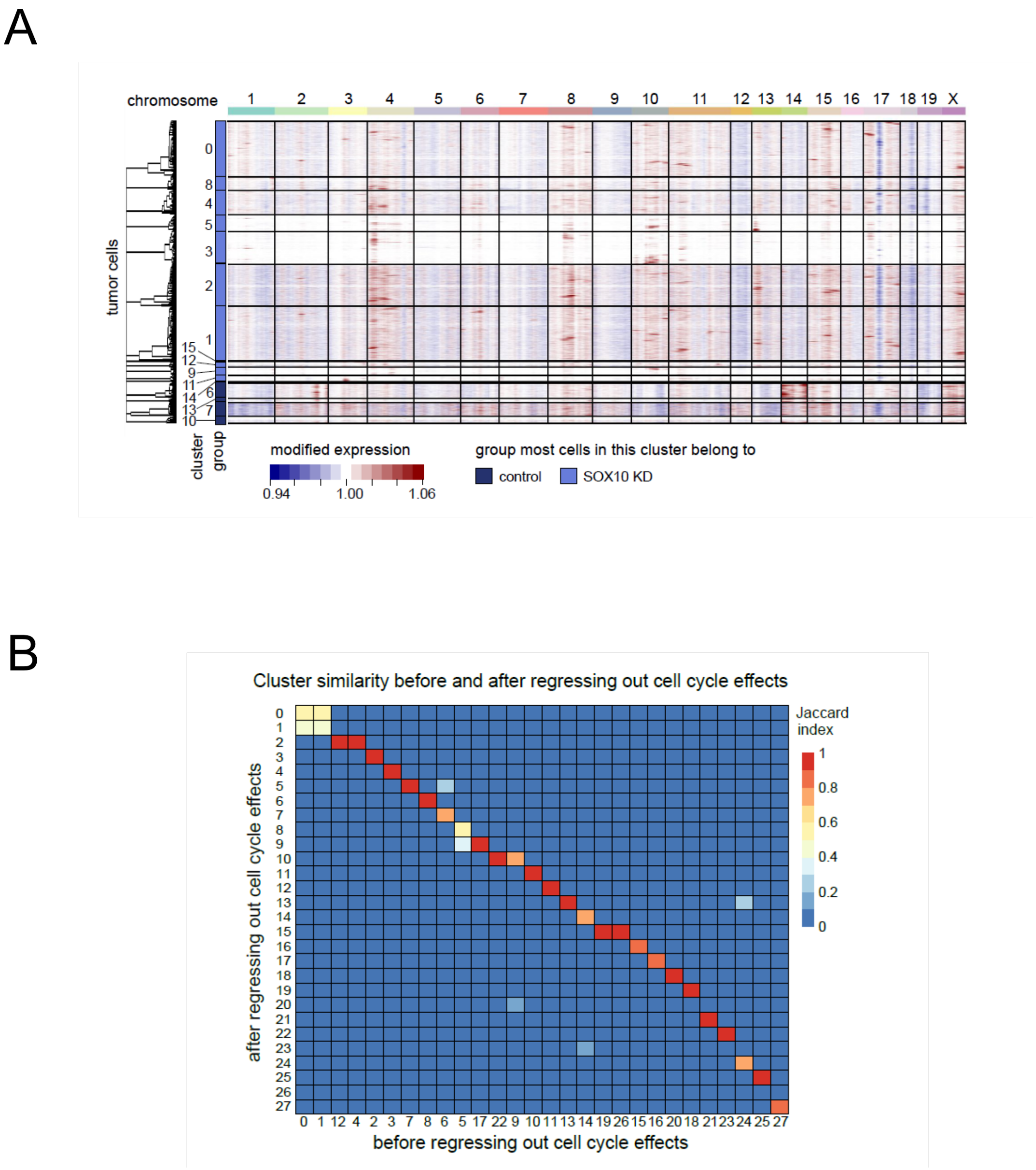

Figure S5. Further QC procedures of the scRNA-seq dataset.

(A) Analysis of the copy number variations in GFP-positive tumor cells. (B) Comparison of cluster similarities before and after regressing out cell cycle-related effects. Heatmap summarizing the Jaccard similarity indices between clusters before and after regressing out cell cycle-related effects. The median Jaccard index per cluster before regression with their best matching cluster after regression was 0.87. (These analyses were performed by J. Keding during her master's thesis research)

7 Publications

Publication related to this thesis:

Wu, Yonghe, Michael Fletcher, Zuguang Gu, Qi Wang, Barbara Costa, Anna Bertoni, **Ka-Hou Man**, Magdalena Schlotter, Jörg Felsberg, Jasmin Mangei, Martje Barbus, Ann-Christin Gaupel, Wei Wang, Tobias Weiss, Roland Eils, Michael Weller, Haikun Liu, Guido Reifenberger, Andrey Korshunov, Peter Angel, Peter Lichter, Carl Herrmann, and Bernhard Radlwimmer. 2020. Glioblastoma epigenome profiling identifies *SOX10* as a master regulator of molecular tumour subtype, *Nature Communications*, 11: 6434

Other publications:

Casati, Beatrice, Joseph Peter Verdi, Alexander Hempelmann, Maximilian Kittel, Andrea Gutierrez Klaebisch, Bianca Meister, Sybille Welker, Sonal Asthana, Salvatore Di Giorgio, Pavle Boskovic, **Ka Hou Man**, Meike Schopp, Paul Adrian Ginno, Bernhard Radlwimmer, Charles Erec Stebbins, Thomas Miethke, Fotini Nina Papavasiliou, and Riccardo Pecori. 2022. Rapid, adaptable and sensitive Cas13-based COVID-19 diagnostics using ADESSO, *Nature Communications*, 13: 3308.

Wong, Alissa Michelle, Xiaofan Ding, Aikha Melissa Wong, Mingjing Xu, Luyao Zhang, Howard Ho-Wai Leung, Anthony Wing-Hung Chan, Qi Xiu Song, Joseph Kwong, Loucia Kit-Ying Chan, **Matthew Man**, Mian He, Jinna Chen, Zhe Zhang, Wenxing You, Coleen Lau, Allen Yu, Yingying Wei, Yunfei Yuan, Paul Bo-San Lai, Jingmin Zhao, Kwan Man, Jun Yu, Michael Kahn, and Nathalie Wong. 2022. Unique molecular characteristics of NAFLD-associated liver cancer accentuate β-catenin/TNFRSF19-mediated immune evasion, *Journal of Hepatology*, 77: 410-23.

Ding, Xiaofan, Mian He, Anthony W. H. Chan, Qi Xiu Song, Siu Ching Sze, Hui Chen, **Matthew K. H. Man**, Kwan Man, Stephen L. Chan, Paul B. S. Lai, Xin Wang, and Nathalie Wong. 2019. Genomic and Epigenomic Features of Primary and Recurrent Hepatocellular Carcinomas, *Gastroenterology*, 157: 1630-45.e6.

8 Acknowledgements

I would like to express my gratitude to my supervisor Prof. Dr. Peter Lichter, for his guidance and support throughout my master and doctoral research in the Division. I would also like to thank him for his comments and suggestions during my PhD studies, in particular his time spent on the revision of this thesis.

This PhD endeavor would not have been possible without the direct supervision of Dr. Bernhard Radlwimmer, who gave me the opportunity to work in his subgroup, spent time with me to discuss my project on a weekly basis and encouraged me whenever I made mistakes. I gained many valuable experiences, both scientific or otherwise, while working in his team.

My gratitude also goes to Dr. Yonghe Wu, who sparked my first interest in the field of tumor stem cells. From a mentor to a key collaborator of this project, his unwavering support and kind words of encouragement were always something I could count on throughout these years.

I would like to thank my TAC members Prof. Dr. Benedikt Brors, Dr. Hai-kun Liu and Dr. Carl Herrmann for their valuable advice and discussion during my TAC meetings. Special thanks go to Benedikt, who sent help for the bioinformatic analysis and spent time proof-reading this thesis. I would also like to take this opportunity to thank Prof. Dr. Viktor Umansky and Dr. Sevin Turcan, who agreed to be my examiners and reviewed this thesis.

I would also like to thank Dr. Charles Imbusch and Johanna Keding for the bioinformatics analyses. I would like to thank Jan-Philipp Mallm, Katherina Bauer and Michele Bortolomeazzi from Single Cell Core Lab for the scRNA library preparation during the difficult times of the COVID-19 lockdown. I would also like to thank Tony, Xiujian and Joey from Haikun’s group, for fun times together discussing the interesting topics in addition to science, and ensuring I have an ample supply of antibodies for my work.

I am grateful to my current and former lab members of the TMB group: Mike Fletcher, Liliana Francois, Pavle Boskovic, Jasmin Mangei, Theresa Schmid, Nathalie Wilke, Yuan Peng, Anne Jenseit, Petra Schroeter, Archim Stephan and Magdalena Schlotter, for their mental and technical support during my stay in the group. In particular, I would like to thank Magdalena, for her joyful spirit we all envy and adore, and her special German classes and unforgettable German slangs. Special thanks go to Pavle, with whom we went through countless fun times in establishing the COVID testing station during the lockdown, mouse experiments and organoid culture together. I would also like to thank all other members of the B06x, especially Tolga Lokumcu and Mona Göttmann, for always encouraging me to come out of my shell. I really cherished the kindness and sincerity that every member of the B06X showed. It is safe to say that I will remember my time in B06X fondly as the journey of enlightenment through uncharted territories in science and in personal growth – territories that were unimaginable to me before but I will now never forget them.

I am truly grateful to my friends in Germany, who made Heidelberg more like home – every small thing we did together distracted me from stress of my PhD. I want to say thank you to other friends and former lab members in Hong Kong and Macau, who checked on me every now and then to ensure that I was on track. Above all, in this daunting PhD journey, all these people reminded me that I was actually truly blessed.

Lastly, I am indebted to my family, who supports me in whatever I do. Though they may not understand much written in this thesis, I dedicate this work to them, for letting me know they are always there for me no matter what happens.

9 References

1. Yan, H., et al., *IDH1 and IDH2 mutations in gliomas.* N Engl J Med, 2009. **360**(8): p. 765-73.
2. Louis, D.N., et al., *The 2021 WHO Classification of Tumors of the Central Nervous System: a summary.* Neuro Oncol, 2021. **23**(8): p. 1231-1251.
3. Ostrom, Q.T., et al., *CBTRUS Statistical Report: Primary Brain and Other Central Nervous System Tumors Diagnosed in the United States in 2014-2018.* Neuro Oncol, 2021. **23**(12 Suppl 2): p. iii1-iii105.
4. Rice, T., et al., *Understanding inherited genetic risk of adult glioma - a review.* Neurooncol Pract, 2016. **3**(1): p. 10-16.
5. Schwartzbaum, J., et al., *Polymorphisms associated with asthma are inversely related to glioblastoma multiforme.* Cancer Res, 2005. **65**(14): p. 6459-65.
6. Stupp, R., et al., *Radiotherapy plus concomitant and adjuvant temozolomide for glioblastoma.* N Engl J Med, 2005. **352**(10): p. 987-96.
7. Weller, M., et al., *EANO guidelines on the diagnosis and treatment of diffuse gliomas of adulthood.* Nat Rev Clin Oncol, 2021. **18**(3): p. 170-186.
8. Hegi, M.E., et al., *MGMT gene silencing and benefit from temozolomide in glioblastoma.* N Engl J Med, 2005. **352**(10): p. 997-1003.
9. Weller, M., *Where does O(6) -methylguanine DNA methyltransferase promoter methylation assessment place temozolomide in the future standards of care for glioblastoma?* Cancer, 2018. **124**(7): p. 1316-1318.
10. Perry, J.R., et al., *Short-Course Radiation plus Temozolomide in Elderly Patients with Glioblastoma.* N Engl J Med, 2017. **376**(11): p. 1027-1037.
11. Minniti, G., et al., *Current status and recent advances in reirradiation of glioblastoma.* Radiat Oncol, 2021. **16**(1): p. 36.
12. Yung, W.K., et al., *A phase II study of temozolomide vs. procarbazine in patients with glioblastoma multiforme at first relapse.* Br J Cancer, 2000. **83**(5): p. 588-93.
13. van den Bent, M.J., et al., *Randomized phase II trial of erlotinib versus temozolomide or carmustine in recurrent glioblastoma: EORTC brain tumor group study 26034.* J Clin Oncol, 2009. **27**(8): p. 1268-74.
14. Inda, M.M., et al., *Chromosomal abnormalities in human glioblastomas: gain in chromosome 7p correlating with loss in chromosome 10q.* Mol Carcinog, 2003. **36**(1): p. 6-14.
15. Cancer Genome Atlas Research, N., *Comprehensive genomic characterization defines human glioblastoma genes and core pathways.* Nature, 2008. **455**(7216): p. 1061-8.
16. Brennan, C.W., et al., *The somatic genomic landscape of glioblastoma.* Cell, 2013. **155**(2): p. 462-77.
17. Mizoguchi, M., et al., *Activation of STAT3, MAPK, and AKT in malignant astrocytic gliomas: correlation with EGFR status, tumor grade, and survival.* J Neuropathol Exp Neurol, 2006. **65**(12): p. 1181-8.
18. Puputti, M., et al., *Amplification of KIT, PDGFRA, VEGFR2, and EGFR in gliomas.* Mol Cancer Res, 2006. **4**(12): p. 927-34.
19. Kwak, Y., et al., *C-MET overexpression and amplification in gliomas.* Int J Clin Exp Pathol, 2015. **8**(11): p. 14932-8.
20. Xie, Q., et al., *Hepatocyte growth factor (HGF) autocrine activation predicts sensitivity to MET inhibition in glioblastoma.* Proc Natl Acad Sci U S A, 2012. **109**(2): p. 570-5.
21. Horn, S., et al., *TERT promoter mutations in familial and sporadic melanoma.* Science, 2013. **339**(6122): p. 959-61.

22. Huang, F.W., et al., *Highly recurrent TERT promoter mutations in human melanoma.* Science, 2013. **339**(6122): p. 957-9.
23. Killela, P.J., et al., *TERT promoter mutations occur frequently in gliomas and a subset of tumors derived from cells with low rates of self-renewal.* Proc Natl Acad Sci U S A, 2013. **110**(15): p. 6021-6.
24. Barthel, F.P., et al., *Longitudinal molecular trajectories of diffuse glioma in adults.* Nature, 2019. **576**(7785): p. 112-+.
25. Wang, J.G., et al., *Clonal evolution of glioblastoma under therapy.* Nature Genetics, 2016. **48**(7): p. 768-+.
26. Draaisma, K., et al., *Molecular Evolution of IDH Wild-Type Glioblastomas Treated With Standard of Care Affects Survival and Design of Precision Medicine Trials: A Report From the EORTC 1542 Study.* Journal of Clinical Oncology, 2020. **38**(1): p. 81-+.
27. Korber, V., et al., *Evolutionary Trajectories of IDH(WT) Glioblastomas Reveal a Common Path of Early Tumorigenesis Instigated Years ahead of Initial Diagnosis.* Cancer Cell, 2019. **35**(4): p. 692-704 e12.
28. Johnson, B.E., et al., *Mutational analysis reveals the origin and therapy-driven evolution of recurrent glioma.* Science, 2014. **343**(6167): p. 189-193.
29. Phillips, H.S., et al., *Molecular subclasses of high-grade glioma predict prognosis, delineate a pattern of disease progression, and resemble stages in neurogenesis.* Cancer Cell, 2006. **9**(3): p. 157-73.
30. Verhaak, R.G., et al., *Integrated genomic analysis identifies clinically relevant subtypes of glioblastoma characterized by abnormalities in PDGFRA, IDH1, EGFR, and NF1.* Cancer Cell, 2010. **17**(1): p. 98-110.
31. Wang, Q., et al., *Tumor Evolution of Glioma-Intrinsic Gene Expression Subtypes Associates with Immunological Changes in the Microenvironment.* Cancer Cell, 2017. **32**(1): p. 42-56 e6.
32. Noble, M., C. Proschel, and M. Mayer-Proschel, *Getting a GR(i)P on oligodendrocyte development.* Dev Biol, 2004. **265**(1): p. 33-52.
33. Wu, Y., et al., *Glioblastoma epigenome profiling identifies SOX10 as a master regulator of molecular tumour subtype.* Nat Commun, 2020. **11**(1): p. 6434.
34. Gangoso, E., et al., *Glioblastomas acquire myeloid-affiliated transcriptional programs via epigenetic immunoediting to elicit immune evasion.* Cell, 2021. **184**(9): p. 2454-2470 e26.
35. Schmitt, M.J., et al., *Phenotypic Mapping of Pathologic Cross-Talk between Glioblastoma and Innate Immune Cells by Synthetic Genetic Tracing.* Cancer Discov, 2021. **11**(3): p. 754-777.
36. Noushmehr, H., et al., *Identification of a CpG island methylator phenotype that defines a distinct subgroup of glioma.* Cancer Cell, 2010. **17**(5): p. 510-22.
37. Sturm, D., et al., *Hotspot mutations in H3F3A and IDH1 define distinct epigenetic and biological subgroups of glioblastoma.* Cancer Cell, 2012. **22**(4): p. 425-37.
38. Sturm, D., et al., *Paediatric and adult glioblastoma: multiform (epi)genomic culprits emerge.* Nat Rev Cancer, 2014. **14**(2): p. 92-107.
39. Ceccarelli, M., et al., *Molecular Profiling Reveals Biologically Discrete Subsets and Pathways of Progression in Diffuse Glioma.* Cell, 2016. **164**(3): p. 550-63.
40. Capper, D., et al., *DNA methylation-based classification of central nervous system tumours.* Nature, 2018. **555**(7697): p. 469-474.
41. Capper, D., et al., *Practical implementation of DNA methylation and copy-number-based CNS tumor diagnostics: the Heidelberg experience.* Acta Neuropathol, 2018. **136**(2): p. 181-210.

42. Hasselbalch, B., et al., *Cetuximab, bevacizumab, and irinotecan for patients with primary glioblastoma and progression after radiation therapy and temozolomide: a phase II trial.* Neuro Oncol, 2010. **12**(5): p. 508-16.
43. Neyns, B., et al., *Stratified phase II trial of cetuximab in patients with recurrent high-grade glioma.* Ann Oncol, 2009. **20**(9): p. 1596-1603.
44. Papavassiliou, K.A. and A.G. Papavassiliou, *The Bumpy Road towards mTOR Inhibition in Glioblastoma: Quo Vadis?* Biomedicines, 2021. **9**(12).
45. Westphal, M., C.L. Maire, and K. Lamszus, *EGFR as a Target for Glioblastoma Treatment: An Unfulfilled Promise.* CNS Drugs, 2017. **31**(9): p. 723-735.
46. Bhat, K.P.L., et al., *Mesenchymal differentiation mediated by NF-kappaB promotes radiation resistance in glioblastoma.* Cancer Cell, 2013. **24**(3): p. 331-46.
47. Lathia, J.D., et al., *Cancer stem cells in glioblastoma.* Genes Dev, 2015. **29**(12): p. 1203-17.
48. Yabo, Y.A., S.P. Niclou, and A. Golebiewska, *Cancer cell heterogeneity and plasticity: A paradigm shift in glioblastoma.* Neuro Oncol, 2022. **24**(5): p. 669-682.
49. Gimple, R.C., et al., *Brain cancer stem cells: resilience through adaptive plasticity and hierarchical heterogeneity.* Nat Rev Cancer, 2022.
50. Lee, J.H., et al., *Human glioblastoma arises from subventricular zone cells with low-level driver mutations.* Nature, 2018. **560**(7717): p. 243-247.
51. Kumar, A., et al., *ADULT NEUROGENESIS IN HUMANS: A Review of Basic Concepts, History, Current Research, and Clinical Implications.* Innov Clin Neurosci, 2019. **16**(5-6): p. 30-37.
52. Altman, J., *Are new neurons formed in the brains of adult mammals?* Science, 1962. **135**(3509): p. 1127-8.
53. Nottebohm, F., *Neuronal replacement in adulthood.* Ann N Y Acad Sci, 1985. **457**: p. 143-61.
54. Reynolds, B.A. and S. Weiss, *Generation of neurons and astrocytes from isolated cells of the adult mammalian central nervous system.* Science, 1992. **255**(5052): p. 1707-10.
55. Ming, G.L. and H. Song, *Adult neurogenesis in the mammalian brain: significant answers and significant questions.* Neuron, 2011. **70**(4): p. 687-702.
56. Doetsch, F., et al., *Subventricular zone astrocytes are neural stem cells in the adult mammalian brain.* Cell, 1999. **97**(6): p. 703-16.
57. Menn, B., et al., *Origin of oligodendrocytes in the subventricular zone of the adult brain.* J Neurosci, 2006. **26**(30): p. 7907-18.
58. Marshall, C.A. and J.E. Goldman, *Subpallial dlx2-expressing cells give rise to astrocytes and oligodendrocytes in the cerebral cortex and white matter.* J Neurosci, 2002. **22**(22): p. 9821-30.
59. Liu, X., et al., *GFAP-expressing cells in the postnatal subventricular zone display a unique glial phenotype intermediate between radial glia and astrocytes.* Glia, 2006. **54**(5): p. 394-410.
60. Zywitza, V., et al., *Single-Cell Transcriptomics Characterizes Cell Types in the Subventricular Zone and Uncovers Molecular Defects Impairing Adult Neurogenesis.* Cell Rep, 2018. **25**(9): p. 2457-2469 e8.
61. Arai, K. and E.H. Lo, *Chapter 18 - Gliogenesis*, in *Primer on Cerebrovascular Diseases (Second Edition)*, L.R. Caplan, et al., Editors. 2017, Academic Press: San Diego. p. 91-95.
62. Arvidsson, A., et al., *Neuronal replacement from endogenous precursors in the adult brain after stroke.* Nat Med, 2002. **8**(9): p. 963-70.
63. Nait-Oumesmar, B., et al., *Activation of the subventricular zone in multiple sclerosis: evidence for early glial progenitors.* Proc Natl Acad Sci U S A, 2007. **104**(11): p. 4694-9.

64. Chakkalakal, J.V., et al., *The aged niche disrupts muscle stem cell quiescence.* Nature, 2012. **490**(7420): p. 355-60.
65. Tumpel, S. and K.L. Rudolph, *Quiescence: Good and Bad of Stem Cell Aging.* Trends Cell Biol, 2019. **29**(8): p. 672-685.
66. Cotsarelis, G., T.T. Sun, and R.M. Lavker, *Label-retaining cells reside in the bulge area of pilosebaceous unit: implications for follicular stem cells, hair cycle, and skin carcinogenesis.* Cell, 1990. **61**(7): p. 1329-37.
67. Kalamakis, G., et al., *Quiescence Modulates Stem Cell Maintenance and Regenerative Capacity in the Aging Brain.* Cell, 2019. **176**(6): p. 1407-1419 e14.
68. Llorens-Bobadilla, E., et al., *Single-Cell Transcriptomics Reveals a Population of Dormant Neural Stem Cells that Become Activated upon Brain Injury.* Cell Stem Cell, 2015. **17**(3): p. 329-40.
69. Sueda, R., et al., *High Hes1 expression and resultant Ascl1 suppression regulate quiescent vs. active neural stem cells in the adult mouse brain.* Genes Dev, 2019. **33**(9-10): p. 511-523.
70. Andersen, J., et al., *A transcriptional mechanism integrating inputs from extracellular signals to activate hippocampal stem cells.* Neuron, 2014. **83**(5): p. 1085-97.
71. Fabra-Beser, J., et al., *Differential Expression Levels of Sox9 in Early Neocortical Radial Glial Cells Regulate the Decision between Stem Cell Maintenance and Differentiation.* J Neurosci, 2021. **41**(33): p. 6969-6986.
72. Kobayashi, T. and R. Kageyama, *Lysosomes and signaling pathways for maintenance of quiescence in adult neural stem cells.* FEBS J, 2021. **288**(10): p. 3082-3093.
73. Kobayashi, T., et al., *Enhanced lysosomal degradation maintains the quiescent state of neural stem cells.* Nat Commun, 2019. **10**(1): p. 5446.
74. Urban, N., I.M. Blomfield, and F. Guillemot, *Quiescence of Adult Mammalian Neural Stem Cells: A Highly Regulated Rest.* Neuron, 2019. **104**(5): p. 834-848.
75. Zhang, J., et al., *Novel Roles of Small Extracellular Vesicles in Regulating the Quiescence and Proliferation of Neural Stem Cells.* Front Cell Dev Biol, 2021. **9**: p. 762293.
76. Kokovay, E., et al., *VCAM1 is essential to maintain the structure of the SVZ niche and acts as an environmental sensor to regulate SVZ lineage progression.* Cell Stem Cell, 2012. **11**(2): p. 220-30.
77. Belenguer, G., et al., *Adult Neural Stem Cells Are Alerted by Systemic Inflammation through TNF-alpha Receptor Signaling.* Cell Stem Cell, 2021. **28**(2): p. 285-299 e9.
78. Bonnet, D. and J.E. Dick, *Human acute myeloid leukemia is organized as a hierarchy that originates from a primitive hematopoietic cell.* Nat Med, 1997. **3**(7): p. 730-7.
79. Uchida, N., et al., *Direct isolation of human central nervous system stem cells.* Proc Natl Acad Sci U S A, 2000. **97**(26): p. 14720-5.
80. Singh, S.K., et al., *Identification of a cancer stem cell in human brain tumors.* Cancer Res, 2003. **63**(18): p. 5821-8.
81. Singh, S.K., et al., *Identification of human brain tumour initiating cells.* Nature, 2004. **432**(7015): p. 396-401.
82. Lan, X., et al., *Fate mapping of human glioblastoma reveals an invariant stem cell hierarchy.* Nature, 2017. **549**(7671): p. 227-232.
83. Bhaduri, A., et al., *Outer Radial Glia-like Cancer Stem Cells Contribute to Heterogeneity of Glioblastoma.* Cell Stem Cell, 2020. **26**(1): p. 48-63 e6.
84. Gazave, E., et al., *Origin and evolution of the Notch signalling pathway: an overview from eukaryotic genomes.* BMC Evol Biol, 2009. **9**: p. 249.
85. Wang, Z., et al., *Emerging role of Notch in stem cells and cancer.* Cancer Lett, 2009. **279**(1): p. 8-12.

86. Hori, K., A. Sen, and S. Artavanis-Tsakonas, *Notch signaling at a glance.* J Cell Sci, 2013. **126**(Pt 10): p. 2135-40.
87. Allen, F. and I. Maillard, *Therapeutic Targeting of Notch Signaling: From Cancer to Inflammatory Disorders.* Front Cell Dev Biol, 2021. **9**: p. 649205.
88. Iso, T., L. Kedes, and Y. Hamamori, *HES and HERP families: multiple effectors of the Notch signaling pathway.* J Cell Physiol, 2003. **194**(3): p. 237-55.
89. Imayoshi, I., et al., *Essential roles of Notch signaling in maintenance of neural stem cells in developing and adult brains.* J Neurosci, 2010. **30**(9): p. 3489-98.
90. Basak, O., et al., *Neurogenic subventricular zone stem/progenitor cells are Notch1-dependent in their active but not quiescent state.* J Neurosci, 2012. **32**(16): p. 5654-66.
91. Boareto, M., D. Iber, and V. Taylor, *Differential interactions between Notch and ID factors control neurogenesis by modulating Hes factor autoregulation.* Development, 2017. **144**(19): p. 3465-3474.
92. Guentchev, M. and R.D. McKay, *Notch controls proliferation and differentiation of stem cells in a dose-dependent manner.* Eur J Neurosci, 2006. **23**(9): p. 2289-96.
93. Borghese, L., et al., *Inhibition of notch signaling in human embryonic stem cell-derived neural stem cells delays G1/S phase transition and accelerates neuronal differentiation in vitro and in vivo.* Stem Cells, 2010. **28**(5): p. 955-64.
94. Breunig, J.J., et al., *Notch regulates cell fate and dendrite morphology of newborn neurons in the postnatal dentate gyrus.* Proc Natl Acad Sci U S A, 2007. **104**(51): p. 20558-63.
95. Ables, J.L., et al., *Notch1 is required for maintenance of the reservoir of adult hippocampal stem cells.* J Neurosci, 2010. **30**(31): p. 10484-92.
96. Ehm, O., et al., *RBPJkappa-dependent signaling is essential for long-term maintenance of neural stem cells in the adult hippocampus.* J Neurosci, 2010. **30**(41): p. 13794-807.
97. Kawaguchi, D., et al., *Dll1 maintains quiescence of adult neural stem cells and segregates asymmetrically during mitosis.* Nat Commun, 2013. **4**: p. 1880.
98. Liau, B.B., et al., *Adaptive Chromatin Remodeling Drives Glioblastoma Stem Cell Plasticity and Drug Tolerance.* Cell Stem Cell, 2017. **20**(2): p. 233-246 e7.
99. MacDonald, B.T., K. Tamai, and X. He, *Wnt/beta-catenin signaling: components, mechanisms, and diseases.* Dev Cell, 2009. **17**(1): p. 9-26.
100. Bengoa-Vergniory, N. and R.M. Kypta, *Canonical and noncanonical Wnt signaling in neural stem/progenitor cells.* Cell Mol Life Sci, 2015. **72**(21): p. 4157-72.
101. Binda, E., et al., *Wnt5a Drives an Invasive Phenotype in Human Glioblastoma Stem-like Cells.* Cancer Res, 2017. **77**(4): p. 996-1007.
102. Huang, M., et al., *Wnt-mediated endothelial transformation into mesenchymal stem cell-like cells induces chemoresistance in glioblastoma.* Sci Transl Med, 2020. **12**(532).
103. Rajakulendran, N., et al., *Wnt and Notch signaling govern self-renewal and differentiation in a subset of human glioblastoma stem cells.* Genes Dev, 2019. **33**(9-10): p. 498-510.
104. Hemmati, H.D., et al., *Cancerous stem cells can arise from pediatric brain tumors.* Proc Natl Acad Sci U S A, 2003. **100**(25): p. 15178-83.
105. Clement, V., et al., *HEDGEHOG-GLI1 signaling regulates human glioma growth, cancer stem cell self-renewal, and tumorigenicity.* Curr Biol, 2007. **17**(2): p. 165-72.
106. Anido, J., et al., *TGF-beta Receptor Inhibitors Target the CD44(high)/Id1(high) Glioma-Initiating Cell Population in Human Glioblastoma.* Cancer Cell, 2010. **18**(6): p. 655-68.
107. Suva, M.L., et al., *Reconstructing and reprogramming the tumor-propagating potential of glioblastoma stem-like cells.* Cell, 2014. **157**(3): p. 580-94.
108. Castellan, M., et al., *Single-cell analyses reveal YAP/TAZ as regulators of stemness and cell plasticity in Glioblastoma.* Nat Cancer, 2021. **2**(2): p. 174-188.
109. Marques, C., et al., *NF1 regulates mesenchymal glioblastoma plasticity and aggressiveness through the AP-1 transcription factor FOSL1.* Elife, 2021. **10**.

110. Riddick, G., et al., *A Core Regulatory Circuit in Glioblastoma Stem Cells Links MAPK Activation to a Transcriptional Program of Neural Stem Cell Identity.* Sci Rep, 2017. **7**: p. 43605.
111. Prager, B.C., et al., *Glioblastoma Stem Cells: Driving Resilience through Chaos.* Trends Cancer, 2020. **6**(3): p. 223-235.
112. Rusu, P., et al., *GPD1 Specifically Marks Dormant Glioma Stem Cells with a Distinct Metabolic Profile.* Cell Stem Cell, 2019. **25**(2): p. 241-257 e8.
113. Caren, H., et al., *Glioblastoma Stem Cells Respond to Differentiation Cues but Fail to Undergo Commitment and Terminal Cell-Cycle Arrest.* Stem Cell Reports, 2015. **5**(5): p. 829-842.
114. Galli, R., et al., *Isolation and characterization of tumorigenic, stem-like neural precursors from human glioblastoma.* Cancer Res, 2004. **64**(19): p. 7011-21.
115. Zheng, H., et al., *p53 and Pten control neural and glioma stem/progenitor cell renewal and differentiation.* Nature, 2008. **455**(7216): p. 1129-33.
116. Lu, C., et al., *IDH mutation impairs histone demethylation and results in a block to cell differentiation.* Nature, 2012. **483**(7390): p. 474-8.
117. Beier, D., et al., *CD133(+) and CD133(-) glioblastoma-derived cancer stem cells show differential growth characteristics and molecular profiles.* Cancer Res, 2007. **67**(9): p. 4010-5.
118. Kenney-Herbert, E., et al., *CD15 Expression Does Not Identify a Phenotypically or Genetically Distinct Glioblastoma Population.* Stem Cells Transl Med, 2015. **4**(7): p. 822-31.
119. Al-Mayhani, T.F., et al., *A non-hierarchical organization of tumorigenic NG2 cells in glioblastoma promoted by EGFR.* Neuro Oncol, 2019. **21**(6): p. 719-729.
120. Auffinger, B., et al., *Conversion of differentiated cancer cells into cancer stem-like cells in a glioblastoma model after primary chemotherapy.* Cell Death Differ, 2014. **21**(7): p. 1119-31.
121. Adamski, V., et al., *Dormant glioblastoma cells acquire stem cell characteristics and are differentially affected by Temozolomide and AT101 treatment.* Oncotarget, 2017. **8**(64): p. 108064-108078.
122. Couturier, C.P., et al., *Single-cell RNA-seq reveals that glioblastoma recapitulates a normal neurodevelopmental hierarchy.* Nat Commun, 2020. **11**(1): p. 3406.
123. Patel, S.J., et al., *Identification of essential genes for cancer immunotherapy.* Nature, 2017. **548**(7669): p. 537-542.
124. Tirosh, I., et al., *Single-cell RNA-seq supports a developmental hierarchy in human oligodendroglioma.* Nature, 2016. **539**(7628): p. 309-313.
125. Venteicher, A.S., et al., *Decoupling genetics, lineages, and microenvironment in IDH-mutant gliomas by single-cell RNA-seq.* Science, 2017. **355**(6332).
126. Filbin, M.G., et al., *Developmental and oncogenic programs in H3K27M gliomas dissected by single-cell RNA-seq.* Science, 2018. **360**(6386): p. 331-335.
127. Neftel, C., et al., *An Integrative Model of Cellular States, Plasticity, and Genetics for Glioblastoma.* Cell, 2019. **178**(4): p. 835-849 e21.
128. Richards, L.M., et al., *Gradient of Developmental and Injury Response transcriptional states defines functional vulnerabilities underpinning glioblastoma heterogeneity.* Nat Cancer, 2021. **2**(2): p. 157-173.
129. Garofano, L., et al., *Pathway-based classification of glioblastoma uncovers a mitochondrial subtype with therapeutic vulnerabilities.* Nat Cancer, 2021. **2**(2): p. 141-156.
130. Wang, L., et al., *The Phenotypes of Proliferating Glioblastoma Cells Reside on a Single Axis of Variation.* Cancer Discov, 2019. **9**(12): p. 1708-1719.

131. Chen, J., et al., *A restricted cell population propagates glioblastoma growth after chemotherapy.* Nature, 2012. **488**(7412): p. 522-6.
132. Wang, X., et al., *Sequential fate-switches in stem-like cells drive the tumorigenic trajectory from human neural stem cells to malignant glioma.* Cell Res, 2021. **31**(6): p. 684-702.
133. Wang, Z., et al., *Cell Lineage-Based Stratification for Glioblastoma.* Cancer Cell, 2020. **38**(3): p. 366-379 e8.
134. Chaligne, R., et al., *Epigenetic encoding, heritability and plasticity of glioma transcriptional cell states.* Nat Genet, 2021. **53**(10): p. 1469-1479.
135. Friebel, E., et al., *Single-Cell Mapping of Human Brain Cancer Reveals Tumor-Specific Instruction of Tissue-Invading Leukocytes.* Cell, 2020. **181**(7): p. 1626-1642 e20.
136. Klemm, F., et al., *Interrogation of the Microenvironmental Landscape in Brain Tumors Reveals Disease-Specific Alterations of Immune Cells.* Cell, 2020. **181**(7): p. 1643-1660 e17.
137. Buonfiglioli, A. and D. Hambardzumyan, *Macrophages and microglia: the cerberus of glioblastoma.* Acta Neuropathol Commun, 2021. **9**(1): p. 54.
138. Ye, X.Z., et al., *Tumor-associated microglia/macrophages enhance the invasion of glioma stem-like cells via TGF-beta1 signaling pathway.* J Immunol, 2012. **189**(1): p. 444-53.
139. Feng, X., et al., *Loss of CX3CR1 increases accumulation of inflammatory monocytes and promotes gliomagenesis.* Oncotarget, 2015. **6**(17): p. 15077-94.
140. Bunse, L., et al., *Suppression of antitumor T cell immunity by the oncometabolite (R)-2-hydroxyglutarate.* Nat Med, 2018. **24**(8): p. 1192-1203.
141. Di Tomaso, T., et al., *Immunobiological characterization of cancer stem cells isolated from glioblastoma patients.* Clin Cancer Res, 2010. **16**(3): p. 800-13.
142. Bao, S., et al., *Glioma stem cells promote radioresistance by preferential activation of the DNA damage response.* Nature, 2006. **444**(7120): p. 756-60.
143. Vora, P., et al., *The Rational Development of CD133-Targeting Immunotherapies for Glioblastoma.* Cell Stem Cell, 2020. **26**(6): p. 832-844 e6.
144. Suva, M.L. and I. Tirosh, *The Glioma Stem Cell Model in the Era of Single-Cell Genomics.* Cancer Cell, 2020. **37**(5): p. 630-636.
145. Gubbay, J., et al., *A gene mapping to the sex-determining region of the mouse Y chromosome is a member of a novel family of embryonically expressed genes.* Nature, 1990. **346**(6281): p. 245-50.
146. Sinclair, A.H., et al., *A gene from the human sex-determining region encodes a protein with homology to a conserved DNA-binding motif.* Nature, 1990. **346**(6281): p. 240-4.
147. Schepers, G.E., R.D. Teasdale, and P. Koopman, *Twenty pairs of sox: extent, homology, and nomenclature of the mouse and human sox transcription factor gene families.* Dev Cell, 2002. **3**(2): p. 167-70.
148. Harley, V.R., R. Lovell-Badge, and P.N. Goodfellow, *Definition of a consensus DNA binding site for SRY.* Nucleic Acids Res, 1994. **22**(8): p. 1500-1.
149. Kondoh, H. and Y. Kamachi, *SOX-partner code for cell specification: Regulatory target selection and underlying molecular mechanisms.* Int J Biochem Cell Biol, 2010. **42**(3): p. 391-9.
150. Werner, M.H., et al., *Molecular basis of human 46X,Y sex reversal revealed from the three-dimensional solution structure of the human SRY-DNA complex.* Cell, 1995. **81**(5): p. 705-14.
151. Connor, F., et al., *DNA binding and bending properties of the post-meiotically expressed Sry-related protein Sox-5.* Nucleic Acids Res, 1994. **22**(16): p. 3339-46.
152. Lee, P.C., et al., *SUMOylated SoxE factors recruit Grg4 and function as transcriptional repressors in the neural crest.* J Cell Biol, 2012. **198**(5): p. 799-813.

153. Klum, S., et al., *Sequentially acting SOX proteins orchestrate astrocyte- and oligodendrocyte-specific gene expression.* EMBO Rep, 2018. **19**(11).
154. Bergsland, M., et al., *Sequentially acting Sox transcription factors in neural lineage development.* Genes Dev, 2011. **25**(23): p. 2453-64.
155. Malas, S., et al., *The isolation and high-resolution chromosomal mapping of human SOX14 and SOX21; two members of the SOX gene family related to SOX1, SOX2, and SOX3.* Mamm Genome, 1999. **10**(9): p. 934-7.
156. Sandberg, M., M. Kallstrom, and J. Muhr, *Sox21 promotes the progression of vertebrate neurogenesis.* Nat Neurosci, 2005. **8**(8): p. 995-1001.
157. Haslinger, A., et al., *Expression of Sox11 in adult neurogenic niches suggests a stage-specific role in adult neurogenesis.* Eur J Neurosci, 2009. **29**(11): p. 2103-14.
158. Mu, L., et al., *SoxC transcription factors are required for neuronal differentiation in adult hippocampal neurogenesis.* J Neurosci, 2012. **32**(9): p. 3067-80.
159. Nesbitt, A., et al., *Exome sequencing expands the mechanism of SOX5-associated intellectual disability: A case presentation with review of sox-related disorders.* Am J Med Genet A, 2015. **167A**(11): p. 2548-54.
160. Stolt, C.C., et al., *SoxD proteins influence multiple stages of oligodendrocyte development and modulate SoxE protein function.* Dev Cell, 2006. **11**(5): p. 697-709.
161. Baroti, T., et al., *Sox13 functionally complements the related Sox5 and Sox6 as important developmental modulators in mouse spinal cord oligodendrocytes.* J Neurochem, 2016. **136**(2): p. 316-28.
162. Stolt, C.C. and M. Wegner, *SoxE function in vertebrate nervous system development.* Int J Biochem Cell Biol, 2010. **42**(3): p. 437-40.
163. Turnescu, T., et al., *Sox8 and Sox10 jointly maintain myelin gene expression in oligodendrocytes.* Glia, 2018. **66**(2): p. 279-294.
164. Scott, C.E., et al., *SOX9 induces and maintains neural stem cells.* Nat Neurosci, 2010. **13**(10): p. 1181-9.
165. Sohn, J., et al., *Identification of Sox17 as a transcription factor that regulates oligodendrocyte development.* J Neurosci, 2006. **26**(38): p. 9722-35.
166. Haseeb, A. and V. Lefebvre, *The SOXE transcription factors-SOX8, SOX9 and SOX10-share a bi-partite transactivation mechanism.* Nucleic Acids Res, 2019. **47**(13): p. 6917-6931.
167. Mollaaghababa, R. and W.J. Pavan, *The importance of having your SOX on: role of SOX10 in the development of neural crest-derived melanocytes and glia.* Oncogene, 2003. **22**(20): p. 3024-34.
168. Stolt, C.C., et al., *Terminal differentiation of myelin-forming oligodendrocytes depends on the transcription factor Sox10.* Genes Dev, 2002. **16**(2): p. 165-70.
169. Southard-Smith, E.M., L. Kos, and W.J. Pavan, *Sox10 mutation disrupts neural crest development in Dom Hirschsprung mouse model.* Nat Genet, 1998. **18**(1): p. 60-4.
170. Paratore, C., et al., *Survival and glial fate acquisition of neural crest cells are regulated by an interplay between the transcription factor Sox10 and extrinsic combinatorial signaling.* Development, 2001. **128**(20): p. 3949-61.
171. Potterf, S.B., et al., *Analysis of SOX10 function in neural crest-derived melanocyte development: SOX10-dependent transcriptional control of dopachrome tautomerase.* Dev Biol, 2001. **237**(2): p. 245-57.
172. Pingault, V., et al., *SOX10: 20 years of phenotypic plurality and current understanding of its developmental function.* J Med Genet, 2022. **59**(2): p. 105-114.
173. Bondurand, N., et al., *Interaction among SOX10, PAX3 and MITF, three genes altered in Waardenburg syndrome.* Hum Mol Genet, 2000. **9**(13): p. 1907-17.

174. Imayoshi, I., et al., *Oscillatory control of factors determining multipotency and fate in mouse neural progenitors.* Science, 2013. **342**(6163): p. 1203-8.
175. Fufa, T.D., et al., *Genomic analysis reveals distinct mechanisms and functional classes of SOX10-regulated genes in melanocytes.* Hum Mol Genet, 2015. **24**(19): p. 5433-50.
176. Lopez-Anido, C., et al., *Differential Sox10 genomic occupancy in myelinating glia.* Glia, 2015. **63**(11): p. 1897-1914.
177. Marathe, H.G., et al., *BRG1 interacts with SOX10 to establish the melanocyte lineage and to promote differentiation.* Nucleic Acids Res, 2017. **45**(11): p. 6442-6458.
178. Elsesser, O., et al., *Chromatin remodeler Ep400 ensures oligodendrocyte survival and is required for myelination in the vertebrate central nervous system.* Nucleic Acids Res, 2019. **47**(12): p. 6208-6224.
179. He, D., et al., *Chd7 cooperates with Sox10 and regulates the onset of CNS myelination and remyelination.* Nat Neurosci, 2016. **19**(5): p. 678-689.
180. Harris, M.L., et al., *A dual role for SOX10 in the maintenance of the postnatal melanocyte lineage and the differentiation of melanocyte stem cell progenitors.* PLoS Genet, 2013. **9**(7): p. e1003644.
181. Quintes, S., et al., *Zeb2 is essential for Schwann cell differentiation, myelination and nerve repair.* Nat Neurosci, 2016. **19**(8): p. 1050-1059.
182. Reiprich, S., et al., *Transcription factor Sox10 regulates oligodendroglial Sox9 levels via microRNAs.* Glia, 2017. **65**(7): p. 1089-1102.
183. Saunus, J.M., et al., *Epigenome erosion and SOX10 drive neural crest phenotypic mimicry in triple-negative breast cancer.* NPJ Breast Cancer, 2022. **8**(1): p. 57.
184. Hoek, K.S., et al., *Metastatic potential of melanomas defined by specific gene expression profiles with no BRAF signature.* Pigment Cell Res, 2006. **19**(4): p. 290-302.
185. Hoek, K.S., et al., *In vivo switching of human melanoma cells between proliferative and invasive states.* Cancer Res, 2008. **68**(3): p. 650-6.
186. Tsoi, J., et al., *Multi-stage Differentiation Defines Melanoma Subtypes with Differential Vulnerability to Drug-Induced Iron-Dependent Oxidative Stress.* Cancer Cell, 2018. **33**(5): p. 890-904 e5.
187. Shakhova, O., et al., *Antagonistic cross-regulation between Sox9 and Sox10 controls an anti-tumorigenic program in melanoma.* PLoS Genet, 2015. **11**(1): p. e1004877.
188. Sun, C., et al., *Reversible and adaptive resistance to BRAF(V600E) inhibition in melanoma.* Nature, 2014. **508**(7494): p. 118-22.
189. Shaffer, S.M., et al., *Rare cell variability and drug-induced reprogramming as a mode of cancer drug resistance.* Nature, 2017. **546**(7658): p. 431-435.
190. Wouters, J., et al., *Robust gene expression programs underlie recurrent cell states and phenotype switching in melanoma.* Nat Cell Biol, 2020. **22**(8): p. 986-998.
191. Capparelli, C., et al., *Targeting SOX10-deficient cells to reduce the dormant-invasive phenotype state in melanoma.* Nat Commun, 2022. **13**(1): p. 1381.
192. Carro, M.S., et al., *The transcriptional network for mesenchymal transformation of brain tumours.* Nature, 2010. **463**(7279): p. 318-25.
193. Alcantara Llaguno, S.R., et al., *Adult Lineage-Restricted CNS Progenitors Specify Distinct Glioblastoma Subtypes.* Cancer Cell, 2015. **28**(4): p. 429-440.
194. Lau, J., et al., *STAT3 Blockade Inhibits Radiation-Induced Malignant Progression in Glioma.* Cancer Res, 2015. **75**(20): p. 4302-11.
195. Abdelfattah, N., et al., *Single-cell analysis of human glioma and immune cells identifies S100A4 as an immunotherapy target.* Nat Commun, 2022. **13**(1): p. 767.
196. Varn, F.S., et al., *Glioma progression is shaped by genetic evolution and microenvironment interactions.* Cell, 2022. **185**(12): p. 2184-2199 e16.

197. Bankhead, P., et al., *QuPath: Open source software for digital pathology image analysis.* Sci Rep, 2017. **7**(1): p. 16878.
198. Campos, B., et al., *Differentiation therapy exerts antitumor effects on stem-like glioma cells.* Clin Cancer Res, 2010. **16**(10): p. 2715-28.
199. Costa, B., et al., *A Set of Cell Lines Derived from a Genetic Murine Glioblastoma Model Recapitulates Molecular and Morphological Characteristics of Human Tumors.* Cancers (Basel), 2021. **13**(2).
200. Lancaster, M.A. and J.A. Knoblich, *Generation of cerebral organoids from human pluripotent stem cells.* Nat Protoc, 2014. **9**(10): p. 2329-40.
201. Chen, Z., et al., *A high-throughput drug combination screen identifies an anti-glioma synergism between TH588 and PI3K inhibitors.* Cancer Cell Int, 2020. **20**: p. 337.
202. Finneran, M., et al., *Long-term Survival in a Patient with Butterfly Glioblastoma: A Case Report.* Cureus, 2020. **12**(2): p. e6914.
203. Opoku-Darko, M., J.E. Amuah, and J.J.P. Kelly, *Surgical Resection of Anterior and Posterior Butterfly Glioblastoma.* World Neurosurg, 2018. **110**: p. e612-e620.
204. Aibar, S., et al., *SCENIC: single-cell regulatory network inference and clustering.* Nat Methods, 2017. **14**(11): p. 1083-1086.
205. Brooks, L.J., et al., *The white matter is a pro-differentiative niche for glioblastoma.* Nat Commun, 2021. **12**(1): p. 2184.
206. Weng, Q., et al., *Single-Cell Transcriptomics Uncovers Glial Progenitor Diversity and Cell Fate Determinants during Development and Gliomagenesis.* Cell Stem Cell, 2019. **24**(5): p. 707-723 e8.
207. Fulton, D., P.M. Paez, and A.T. Campagnoni, *The multiple roles of myelin protein genes during the development of the oligodendrocyte.* ASN Neuro, 2010. **2**(1): p. e00027.
208. Arai, Y., et al., *Role of Fabp7, a downstream gene of Pax6, in the maintenance of neuroepithelial cells during early embryonic development of the rat cortex.* J Neurosci, 2005. **25**(42): p. 9752-61.
209. Raponi, E., et al., *S100B expression defines a state in which GFAP-expressing cells lose their neural stem cell potential and acquire a more mature developmental stage.* Glia, 2007. **55**(2): p. 165-77.
210. Wang, R., et al., *Adult Human Glioblastomas Harbor Radial Glia-like Cells.* Stem Cell Reports, 2020. **14**(2): p. 338-350.
211. Pollen, A.A., et al., *Molecular identity of human outer radial glia during cortical development.* Cell, 2015. **163**(1): p. 55-67.
212. Marques-Torrejon, M.A., et al., *LRIG1 is a gatekeeper to exit from quiescence in adult neural stem cells.* Nat Commun, 2021. **12**(1): p. 2594.
213. Lamar, E., et al., *Nrarp is a novel intracellular component of the Notch signaling pathway.* Genes Dev, 2001. **15**(15): p. 1885-99.
214. Uxa, S., et al., *Ki-67 gene expression.* Cell Death Differ, 2021. **28**(12): p. 3357-3370.
215. Coats, S., et al., *Requirement of p27Kip1 for restriction point control of the fibroblast cell cycle.* Science, 1996. **272**(5263): p. 877-80.
216. Oki, T., et al., *A novel cell-cycle-indicator, mVenus-p27K-, identifies quiescent cells and visualizes G0-G1 transition.* Sci Rep, 2014. **4**: p. 4012.
217. Agudo, J., et al., *Quiescent Tissue Stem Cells Evade Immune Surveillance.* Immunity, 2018. **48**(2): p. 271-285 e5.
218. Baldominos, P., et al., *Quiescent cancer cells resist T cell attack by forming an immunosuppressive niche.* Cell, 2022. **185**(10): p. 1694-1708 e19.
219. Bruschini, S., G. Ciliberto, and R. Mancini, *The emerging role of cancer cell plasticity and cell-cycle quiescence in immune escape.* Cell Death Dis, 2020. **11**(6): p. 471.

220. Xie, X.P., et al., *Quiescent human glioblastoma cancer stem cells drive tumor initiation, expansion, and recurrence following chemotherapy.* Dev Cell, 2022. **57**(1): p. 32-46 e8.
221. John, N., et al., *Transforming growth factor beta-mediated Sox10 suppression controls mesenchymal progenitor generation in neural crest stem cells.* Stem Cells, 2011. **29**(4): p. 689-99.
222. Wang, H., et al., *Akt Regulates Sox10 Expression to Control Oligodendrocyte Differentiation via Phosphorylating FoxO1.* J Neurosci, 2021. **41**(39): p. 8163-8180.
223. Busker, S., et al., *Pharmacokinetics of metronomic temozolomide in cerebrospinal fluid of children with malignant central nervous system tumors.* Cancer Chemother Pharmacol, 2022. **89**(5): p. 617-627.
224. Patel, M., et al., *Plasma and cerebrospinal fluid pharmacokinetics of intravenous temozolomide in non-human primates.* J Neurooncol, 2003. **61**(3): p. 203-7.
225. Portnow, J., et al., *The neuropharmacokinetics of temozolomide in patients with resectable brain tumors: potential implications for the current approach to chemoradiation.* Clin Cancer Res, 2009. **15**(22): p. 7092-8.
226. Aguanno, S., et al., *A Three-Dimensional Culture Model of Reversibly Quiescent Myogenic Cells.* Stem Cells Int, 2019. **2019**: p. 7548160.
227. Chapouton, P., et al., *Notch activity levels control the balance between quiescence and recruitment of adult neural stem cells.* J Neurosci, 2010. **30**(23): p. 7961-74.
228. Oren, Y., et al., *Cycling cancer persister cells arise from lineages with distinct programs.* Nature, 2021. **596**(7873): p. 576-582.
229. Park, N.I., et al., *ASCL1 Reorganizes Chromatin to Direct Neuronal Fate and Suppress Tumorigenicity of Glioblastoma Stem Cells.* Cell Stem Cell, 2017. **21**(2): p. 209-224 e7.
230. Bent, M.J.V.D., et al., *Updated results of the INTELLANCE 2/EORTC trial 1410 randomized phase II study on Depatux –M alone, Depatux-M in combination with temozolomide (TMZ) and either TMZ or lomustine (LOM) in recurrent EGFR amplified glioblastoma (NCT02343406).* 2018. **36**(15_suppl): p. 2023-2023.
231. Weller, M., et al., *Rindopepimut with temozolomide for patients with newly diagnosed, EGFRvIII-expressing glioblastoma (ACT IV): a randomised, double-blind, international phase 3 trial.* Lancet Oncol, 2017. **18**(10): p. 1373-1385.
232. Szatmari, T., et al., *Detailed characterization of the mouse glioma 261 tumor model for experimental glioblastoma therapy.* Cancer Sci, 2006. **97**(6): p. 546-53.
233. Sarkar, A. and K. Hochedlinger, *The sox family of transcription factors: versatile regulators of stem and progenitor cell fate.* Cell Stem Cell, 2013. **12**(1): p. 15-30.
234. Wegner, M., *All purpose Sox: The many roles of Sox proteins in gene expression.* Int J Biochem Cell Biol, 2010. **42**(3): p. 381-90.
235. Sock, E. and M. Wegner, *Using the lineage determinants Olig2 and Sox10 to explore transcriptional regulation of oligodendrocyte development.* Dev Neurobiol, 2021. **81**(7): p. 892-901.
236. Wang, R., et al., *Glioblastoma stem-like cells give rise to tumour endothelium.* Nature, 2010. **468**(7325): p. 829-33.
237. Jung, E., et al., *Tumor cell plasticity, heterogeneity, and resistance in crucial microenvironmental niches in glioma.* Nat Commun, 2021. **12**(1): p. 1014.
238. Venkataramani, V., et al., *Glioblastoma hijacks neuronal mechanisms for brain invasion.* Cell, 2022. **185**(16): p. 2899-2917 e31.
239. Vong, K.I., et al., *Sox9 is critical for suppression of neurogenesis but not initiation of gliogenesis in the cerebellum.* Mol Brain, 2015. **8**: p. 25.
240. Cronin, J.C., et al., *SOX10 ablation arrests cell cycle, induces senescence, and suppresses melanomagenesis.* Cancer Res, 2013. **73**(18): p. 5709-18.

241. Borgenvik, A., et al., *Dormant SOX9-positive cells facilitate MYC-driven recurrence of medulloblastoma.* Cancer Res, 2022.
242. Furuyama, K., et al., *Continuous cell supply from a Sox9-expressing progenitor zone in adult liver, exocrine pancreas and intestine.* Nat Genet, 2011. **43**(1): p. 34-41.
243. Kadaja, M., et al., *SOX9: a stem cell transcriptional regulator of secreted niche signaling factors.* Genes Dev, 2014. **28**(4): p. 328-41.
244. Laughney, A.M., et al., *Regenerative lineages and immune-mediated pruning in lung cancer metastasis.* Nat Med, 2020. **26**(2): p. 259-269.
245. Sosa, M.S., et al., *NR2F1 controls tumour cell dormancy via SOX9- and RARbeta-driven quiescence programmes.* Nat Commun, 2015. **6**: p. 6170.
246. Munoz, J., et al., *The Lgr5 intestinal stem cell signature: robust expression of proposed quiescent '+4' cell markers.* EMBO J, 2012. **31**(14): p. 3079-91.
247. Lin, C.C., et al., *Knock-out of Hopx disrupts stemness and quiescence of hematopoietic stem cells in mice.* Oncogene, 2020. **39**(28): p. 5112-5123.
248. Roche, K.C., et al., *SOX9 maintains reserve stem cells and preserves radioresistance in mouse small intestine.* Gastroenterology, 2015. **149**(6): p. 1553-1563 e10.
249. Pommier, A., et al., *Unresolved endoplasmic reticulum stress engenders immune-resistant, latent pancreatic cancer metastases.* Science, 2018. **360**(6394).
250. Spitzer, A., et al., *Mutant IDH Inhibitors Induce Lineage Differentiation in IDH-mutant Oligodendroglioma.* Medrxiv,2021: p. 2021.11.16.21266364.
251. Sharma, S.V., et al., *A chromatin-mediated reversible drug-tolerant state in cancer cell subpopulations.* Cell, 2010. **141**(1): p. 69-80.
252. Semerci, F., et al., *Lunatic fringe-mediated Notch signaling regulates adult hippocampal neural stem cell maintenance.* Elife, 2017. **6**.
253. Cho, I.J., et al., *Mechanisms, Hallmarks, and Implications of Stem Cell Quiescence.* Stem Cell Reports, 2019. **12**(6): p. 1190-1200.
254. Saito, Y., et al., *Induction of cell cycle entry eliminates human leukemia stem cells in a mouse model of AML.* Nat Biotechnol, 2010. **28**(3): p. 275-80.
255. Takeishi, S., et al., *Ablation of Fbxw7 eliminates leukemia-initiating cells by preventing quiescence.* Cancer Cell, 2013. **23**(3): p. 347-61.
256. Basi, G.S., et al., *Amyloid precursor protein selective gamma-secretase inhibitors for treatment of Alzheimer's disease.* Alzheimers Res Ther, 2010. **2**(6): p. 36.
257. Li, X., et al., *The HDAC and PI3K dual inhibitor CUDC-907 synergistically enhances the antileukemic activity of venetoclax in preclinical models of acute myeloid leukemia.* Haematologica, 2021. **106**(5): p. 1262-1277.
258. Pal, S., et al., *Dual HDAC and PI3K Inhibition Abrogates NFkappaB- and FOXM1-Mediated DNA Damage Response to Radiosensitize Pediatric High-Grade Gliomas.* Cancer Res, 2018. **78**(14): p. 4007-4021.
259. Sun, K., et al., *Dual HDAC and PI3K Inhibitor CUDC-907 Downregulates MYC and Suppresses Growth of MYC-dependent Cancers.* Mol Cancer Ther, 2017. **16**(2): p. 285-299.
260. Venkatesh, H.S., et al., *Neuronal Activity Promotes Glioma Growth through Neuroligin-3 Secretion.* Cell, 2015. **161**(4): p. 803-16.
261. Chen, Z., et al., *A paracrine circuit of IL-1β/IL-1R1 between myeloid and tumor cells drives glioblastoma progression.* BioRxiv, 2022: p. 2022.04.03.486888.